COMMUNICATION-LESS SYNCHRONOUS RECTIFICATION FOR IN MOTION WIRELESS CHARGING

by

Joshua B. Larsen

A thesis submitted in partial fulfillment
of the requirements for the degree

of

MASTER OF SCIENCE

in

Electrical Engineering

Approved:

Abhilash Kamineni, Ph.D. Major Professor	Hongjie Wang, Ph.D. Committee Member
Don Cripps, Ph.D. Committee Member	D. Richard Cutler, Ph.D. Vice Provost of Graduate Studies

UTAH STATE UNIVERSITY
Logan, Utah

2023

ABSTRACT

Communication-less Synchronous Rectification for In Motion Wireless Charging

by

Joshua B. Larsen, Master of Science

Utah State University, 2023

Major Professor: Abhilash Kamineni, Ph.D.
Department: Electrical and Computer Engineering

This thesis puts forward a control scheme to allow for synchronous rectification for dynamic wireless power transfer. The automotive industry is transitioning away from internal combustion engines (ICEs) and towards electric vehicles (EVs). This transition is spurred by the environmental and economic benefits EVs offer over ICEs. However, further improvements can still be made to how electric vehicles operate. One of these improvements is the technology of in motion wireless charging or dynamic wireless power transfer. In motion wireless charging offers the ability to remove existing range anxiety concerns for EVs. It also offers the potential for a reduction in battery sizes for EVs, which are the primary cost of EVs, this in turn decreases the total costs of mass EV adoption.

Traditional implementations of in motion wireless charging utilize passive rectification to simplify controls between embedded primary pads and the vehicle. However, this solution, while effective, limits the potential benefits of wireless charging. The use of synchronous or active rectification techniques, offer improved performance, control techniques, and bidirectional capabilities. However, the reason synchronous rectification is not already used in motion charging is the complexity of synchronization over wireless communication.

To move past this challenge, this thesis investigates a synchronization scheme that can be achieved without communication by taking advantage of induced free resonant currents

in the vehicle's tuning network to synchronize the switching transitions to receive power. In this thesis, a traditional in motion wireless charging system utilizing passive rectification is designed and built as a benchmark for dynamic charging. Simulations of this control scheme are presented. Practical considerations are addressed for hardware realization. Finally, the control approach is validated through hardware in static and dynamic applications.

(115 pages)

PUBLIC ABSTRACT

Communication-less Synchronous Rectification for In Motion Wireless Charging

Joshua B. Larsen

This thesis puts forward a control scheme to allow for synchronous rectification for dynamic wireless power transfer. The automotive industry is transitioning away from internal combustion engines (ICEs) and towards electric vehicles (EVs). This transition is spurred by the environmental and economic benefits EVs offer over ICEs. However, further improvements can still be made to how electric vehicles operate. One of these improvements is the technology of in motion wireless charging or dynamic wireless power transfer. In motion wireless charging offers the ability to remove existing range anxiety concerns for EVs. It also offers the potential for a reduction in battery sizes for EVs, which are the primary cost of EVs, this in turn decreases the total costs of mass EV adoption.

Traditional implementations of in motion wireless charging utilize passive rectification to simplify controls between embedded primary pads and the vehicle. However, this solution while effective, limits the potential benefits of wireless charging. The use of synchronous or active rectification techniques, offer improved performance, control techniques, and bidirectional capabilities. However, the reason synchronous rectification is not already used in in motion charging is the complexity of synchronization over wireless communication.

To move past this challenge, this thesis investigates a synchronization scheme that can be achieved without communication by taking advantage of induced free resonant currents in the vehicle's tuning network to synchronize the switching transitions to receive power. In this thesis a traditional in motion wireless charging system utilizing passive rectification is designed and built as a benchmark for dynamic charging. Simulations of this control scheme are presented. Practical considerations are addressed for hardware realization. Finally, the control approach is validated through hardware in static and dynamic applications.

This is for my family. Without your constant support, help, direction and willingness to listen to me talk about jibberish all the time this wouldn't be possible.

ACKNOWLEDGMENTS

I would like to thank first my advisor Abhilash for helping teach me what it takes to be an engineer and more importantly a research engineer. Next I would like to thank everyone that was able to help me with the build of this project including Mayank, Jaron, Mikayla, Ahbdullah, Azmeer, and Haris. Without all of your help with PCB design principles, running experiments, and staying extremely late to get the system running, I would not have finished in time. Outside the project itself, I would like to thank everyone who helped me with the theory of power electronics and design philosophy including Matt, Sanat, Aditya, Shubhangi, Craig, and Shun. Lastly, I would like to thank everyone else who worked in the lab, who always made it fun to come in and work.

Joshua B. Larsen

CONTENTS

Page

LIST OF TABLES

LIST OF FIGURES

CHAPTER 1

INTRODUCTION

1.1 Background

As of 2021, the current market share in the US for light duty vehicles that are fully electric vehicles (EV) is 3.4%. This is up from the less than 1% market share as of 2018 [1]. This gradual but consistent increase in electric vehicle sales in the United States is expected to continue for the foreseeable future, and its trend for the last several years can be seen in Fig. 1.1. This growing shift in the automotive industry away from traditional internal combustion engines (ICEs) and towards EVs is being driven by many facets. One of the primary driving forces is the push to reduce greenhouse gas emissions.

The transportation industry is one of the main contributors to CO_2 emissions [9]. In 2020, 27% of greenhouse gas emission emitted in the United States came from transportation [2]. The breakdown of greenhouse gas emission by sector in the United States can be seen in Fig. 1.2. Within the 27% of greenhouse gas emissions given off by the transportation industry, 83% is from light, medium, and heavy-duty vehicles used along American roadways as seen in Fig. 1.3. Many governments across the globe are implementing increasingly strict

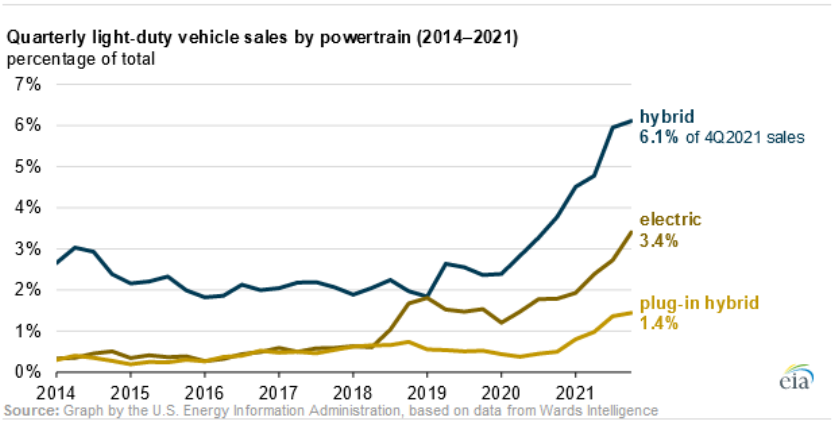

Fig. 1.1: EV Adoption Rate in US [1]

emission regulations for traditional vehicles and increasing tax incentives and subsidies on electric vehicles. As of 2015, 194 parties have signed the Paris Agreement, which aims to be a worldwide collective effort in a pathway to a net-zero emission world [3]. As of 2021, almost all the signing countries have ratified the agreement, as seen in Fig. 1.4. Thus, a government-aided transition to reduce the amount of greenhouse gases emitted by the transportation industry is assured.

Electrified vehicles offer a solution to reduce this large section of greenhouse gas emissions within the United States and around the world. EVs are a zero-emission source of transportation after production, in that driving an electric vehicle emits zero-emissions. EVs are also more energy efficient in their power train than internal combustion engines. EVs typically operate with a grid-to-wheel efficiency of 60-73% [10]. ICEs operate with a tank-to-wheel energy efficiency of 12-30% [10]. However, converting the transportation industry to electric is not an effective solution on its own, since the energy generation for an electric vehicle can still be powered by emission producing sources. These sources of energy production are of a higher efficiency than cars in burning fossil fuels, with a range of 32-45% [11]. However, the actual power generation to wheel utilization for electric vehicles becomes only 19-32% efficient when using fossil fuels as an energy source. This means that EVs are currently more environmentally friendly than ICEs, but still lead to the production of greenhouse gas emissions during use due to the utilization of fossil fuels for power generation on a comparable level to ICEs [12].

With 25% of greenhouse gases produced within the US coming directly from electricity production, adding the transportation energy needs to the current breakup of energy producing sources would only lead to marginal decreases or no measurable decrease in emissions. However, by powering newly made electric vehicles from greener or renewable sources of energy such as nuclear, solar, or wind, a major reduction in greenhouse gases can occur since the source to wheel emissions of EVs can be greatly reduced and possibly be negated. This process of electrifying the transportation industry stands as an important sector in the transition towards a green future [13].

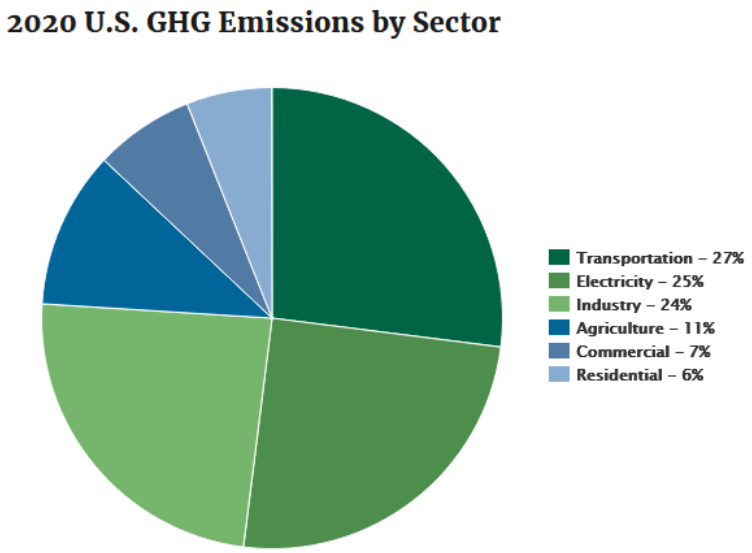

Fig. 1.2: Break Down of US Greenhouse Gas Emissions [2]

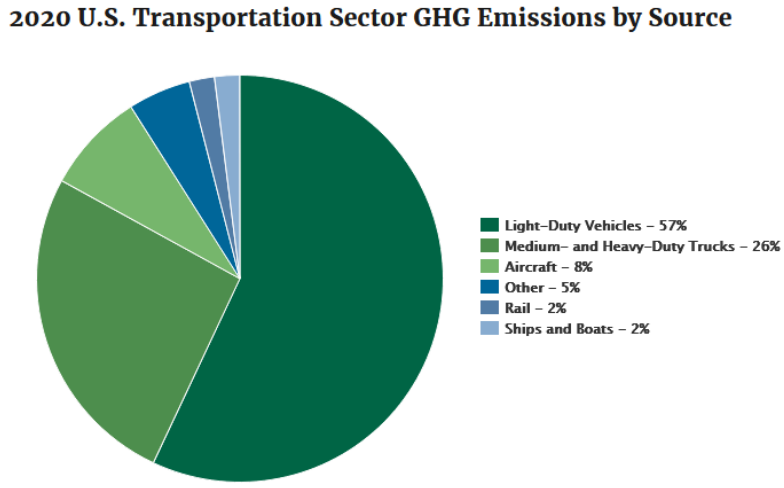

Fig. 1.3: Break Down of US Greenhouse Gas Emissions within Transportation [2]

Fig. 1.4: Map of Countries that have signed and Ratified Paris Agreement [3]

1.1.1 Current State of Electric Vehicles

Outside the large scale implications of greenhouse gas emissions and government policies pushing shifts within the transportation industry towards electric vehicles, EVs offer several compelling advantages to gasoline powered vehicles that an average consumer may enjoy. Electric vehicles are quieter and have performance benefits such as instantaneous torque. They do not idle or consume much energy while stopped. Newer electric vehicles generally offer regenerative breaking allowing for energy recuperation, improving efficiency and allowing for one-pedal driving. They can also provide unique advantages outside traditional applications, such as the new Ford Lightning pickup truck, which offers backup power in case of a power outage for a consumer's home. The Ford Lightning can also operate as a power supply for work equipment, coolers and other devices, allowing for more convenient outdoor uses or worksite deployments [14].

The adoption rates of EVs are still limited due to the challenges that come with an emerging technological field and as a consumer good. There are many facets affecting adoption rates of EVs, including demographics, driving patterns, exposure, and expected benefits. Each of these have an effect in a consumer's opinion of electric vehicles [15]. One of, the largest impediments from a technological standpoint is current battery technology.

Currently, the specific energy of batteries is still relatively small when compared to the specific energy of gasoline, restricting the range of EVs [16]. Batteries are also costly; as of 2021, a battery pack costs on average $132 per kWh to produce [17]. The number most experts have touted for EV battery cost to become cost competitive to current internal combustion engines is $100 per kWh. This would entail that if the only method of improvement for EVs range was through battery technology, there would have to be a reduction of almost 25% in cost to produce. This creates an issue since any direct improvement of EV range is mostly dependent on increasing battery size, which increases cost and weight of already costly and heavy vehicles. The restriction on range for electric vehicles, the currently small network of charging infrastructure, and the relatively long refueling times, leads to the concept of range anxiety. Range anxiety is a consumer's fear of running out of charge while driving an electric vehicle and being unable to recharge [18]. Range anxiety manifests itself in the recharging patterns of consumers. For consumers going on long trips, regular hour long stops need to be budgeted into the trip's time. Also, when those breaks occur may be dependent upon future charging locations along the route, causing anxiety about refueling and time of travel.

Adding on top of the consumer's concept of range anxiety, the method of charging an increasing market share of EVs has a large impact on the current electrical grid and the price of energy production [19]. As the grid gradually shifts away from fossil fuels and towards green energy sources in line with government policies, the grid's behavior and structure will change drastically. As of 2022, the grid is still largely operating as a monolithic power source with large momentum. The stability generated on the grid is drawn from the fossil fuel plants driving it. However, most green energy sources, excluding nuclear, do not operate in the same fashion. They are more prone to large fluctuations from an ever-changing environment. As such, these variations need to be accounted for and smoothed out through additional energy storage being introduced. One promising method to help with grid stability is through vehicle-to-grid (V2G) connections of EVs. Vehicle-to-grid is the concept of utilizing the large batteries available within electric vehicles as an energy storage

mechanism for the grid [20–23]. V2G would entail consumers allowing utility companies or vehicle manufacturers and dealerships to purchase electricity from their vehicles at defined rates, and or offer subsidies to consumers when purchasing EVs for use of their battery pack.

Regardless of dealing with range anxiety, grid stability, and the price and size of batteries, multiple areas of research are being pursued and show promising trends [24–30]. This thesis is focused on the charging infrastructure for electric vehicles that would help with range anxiety concerns. Charging solutions for EVs can be broken down into three complimentary and often overlapping areas of research and application: extreme fast charging, plug-in-charging and wireless static/dynamic charging.

1.1.2 Charging Technologies

Extreme fast charging (XFC) is the research field related to the increase of power delivery to vehicles for quick recharging [25, 26, 31]. This field of research aims to minimize charging times to be more comparable to ICEs' refueling time of only a few minutes. Typically, this technology is applied to plug-in chargers, but it can also be applied to wireless charging. Some automakers such as Tesla and Porsche already offer XFC plug-in technologies. A Tesla Supercharger location shown in Fig. 1.5 [32, 33]. Plug in chargers are an efficient method to charge vehicles, offering a range of 80-90% efficiency, with a high of 94% [34]. Many research areas are focused on high power connections to the grid and the power electronics necessary to convert medium grid voltage to usable levels for EV charging [31, 35]

However, there are limitations with XFC and plug-in charging as the primary method to recharge EVs. First, plug-in chargers are inconvenient for consumers to use. These inconveniences stem from the charging cable itself. The cable can be a cause of concern given the cables may be rather large and difficult to handle given that they are required to carry currents in the hundreds of amperes. The cable could also be water cooled to decrease the size of the cable at the cost of increasing the points of failure and increasing complexity. Plug-in chargers are prone to weathering given the need to have increasing

amounts of convenient locations for people to charge as seen in Fig. 1.6. The convenient locations for EV charging often lead to chargers being built in locations causing eyesores and impediments to pedestrian traffic. They also pose a risk of vandalism and cybersecurity, given the exposed hardware [36, 37].

Additionally, XFC technology is at a point in which it is no longer being limited by the power electronics but by the charging rates of batteries. For current lithium based batteries, the extremely high charging rates or C rates are only available for a small portion of the batteries overall charging time [38]. The power delivery vs. state of charge curve for several vehicles can be seen in Fig. 1.7. This entails that for most of the vehicle's charging time, the power delivery is limited to a much slower rate. Even though the overall power delivery is limited for much of its charging cycle, the initial power delivery at these extreme rates is very beneficial for quick recharges that don't need to fully recharge the vehicle. The second consideration, is that charging at higher rates, the battery's lifetime is degraded at a higher rate leading to increased vehicle maintenance, cost, and carbon footprint [38, 39].

Another technology that is emerging for the transportation industry is wireless power transfer (WPT), more specifically, inductive wireless power transfer (IPT). This technology has been studied extensively at lower power levels for consumer electronics and is now starting to see commercial use at higher power levels for EV charging [40]. WPT offers a solution to several of the concerns listed with plug in charging. Specifically, allowing for park and charge without interaction with high power cabling [30]. This improves the convenience

Fig. 1.5: Tesla Fast Charging Stations [4]

Fig. 1.6: Charging Stations built in a remote part of Palmdale, California [5]

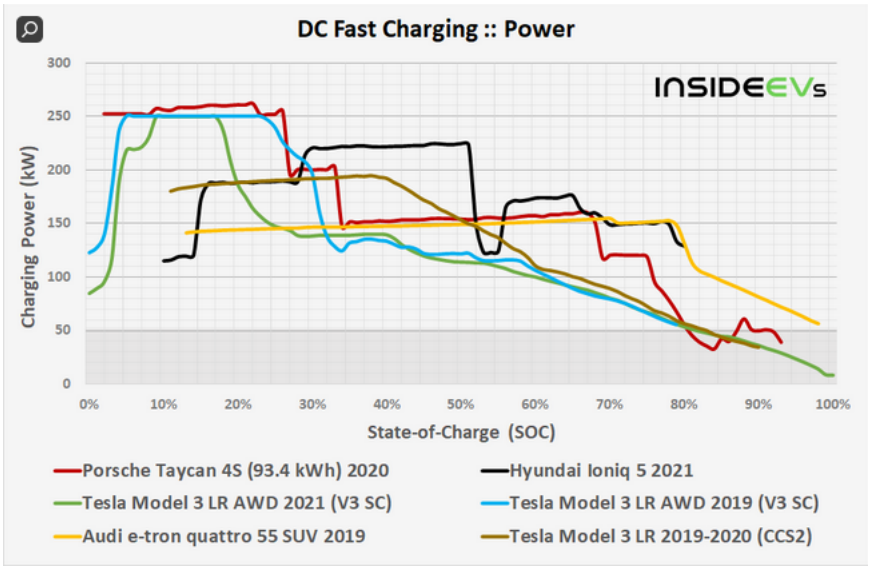

Fig. 1.7: Power Delivery vs SOC curve [6]

for the consumer, removes potential failure points, lowers cybersecurity risks with DC-DC connections, and moves charging infrastructure from posts seen in 1.6 to underground shown in Fig. 1.8a. It also would promote the concept of opportunity charging if enough wireless chargers were deployed. Opportunity charging would allow the consumer to charge whenever the vehicle is stopped without any direct interaction with a charger.

Extending the technology of wireless power transfer, another emerging technology is known as in motion wireless charging or dynamic wireless power transfer (DWPT). DWPT offers a new approach to vehicle charging through a new method of recharging without stopping. This is an excellent solution for long-haul trucking applications and commuting. As well as quasi-dynamic charging for fixed bus routes or high density intersections [24, 27, 28], DWPT allows for several improved benefits for EVs. First, DWPT is a method to help deal with range anxiety for consumers by enabling consumers to recharge while driving. Range anxiety can be overcome completely if enough roadways are electrified or electrified to a high enough power level. Second, is a reduction in the size of EV batteries. The use of DWPT decreases the need for electric vehicles to have large batteries capable of handling long durations without charging. Bringing the charge to the vehicle more regularly will lead to cost reductions and performance improvements across the board for EVs. Third, is by charging the vehicles more regularly, the need for XFC is diminished. This can aid in reducing the wear and tear on EV batteries.

Initial applications for this technology are focused on fixed route applications and quasi-dynamic systems, but can grow into highway and interstate installations. Several companies such as WAVE, Witricity, Momentum, Electreon have implemented working DWPT systems [40]. The company WAVE has developed a wireless charging station for an electric bus route in California, which has been in operation for over 5 years, seen in Fig.1.8. Its application falls under the static category since it is only utilized for short bus stops.

Electreon, another company, has implemented several other pilot projects, including a kilometer long DWPT system in Italy along an inter-city toll road that powers city

buses. The pad embedding of the system can be seen in Fig. 1.9. As the deployment of DWPT systems increases to a larger scale, there will be a shift in the transportation industry towards the benefits explained earlier. This technology does not discount the need for plug in charging or XFC technology. There are still many use cases and needs for them in an electrified transportation industry. Therefore, a combination of both of these technologies offer the best result for EV adoption and deployment. This thesis focuses in on the application of in motion or dynamic wireless power transfer.

1.2 Literature Review

1.2.1 Static Wireless Power Transfer

Wireless Power Transfer Technologies

The fundamental component of in motion wireless charging is founded from traditional or static wireless power transfer. The field of wireless power transfer covers a large area of power levels and use cases, ranging from charging small consumer electronics like cell phones, biomedical devices, and transmitting power to remote areas without direct connection to the power grid [41]. There are several types of WPT technologies that exist. At the highest level there are two distinct categories of wireless power transfer, near-field and far-field or non-radiative and radiative respectively. Near-field WPT technologies include Inductive and capacitive coupling. Far-field includes the use of microwaves or lasers to transmit power. The categories of wireless power transfer are also shown in Fig. 1.10. These systems are generally used for applications specific to their respective radiative type. For EV charging, near field technologies are typically utilized. Simple example circuits for inductive and capacitive coupling can be seen in Fig 1.11. These circuits transmit power through magnetic and electric fields, respectively.

For the given application of charging EVs, there are some major constraints. The main two being safety and the ability to provide large amounts of power, from tens to hundreds of kilowatts. The only technology that currently shows promise, in literature for EV charging,

(a) WAVE charging pad (b) California Bus Charging

Fig. 1.8: Wireless Charging Installation [7]

Fig. 1.9: Electreon In-Motion Charging Solution

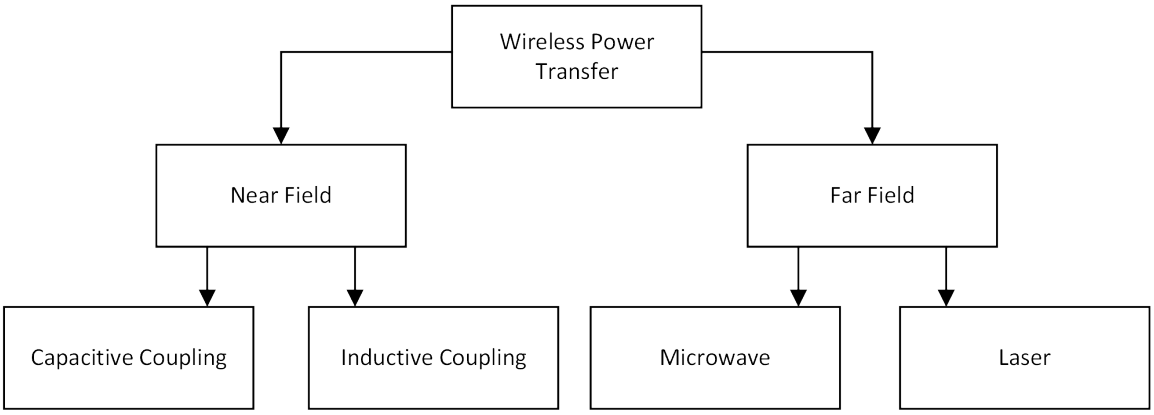

Fig. 1.10: WPT Technologies

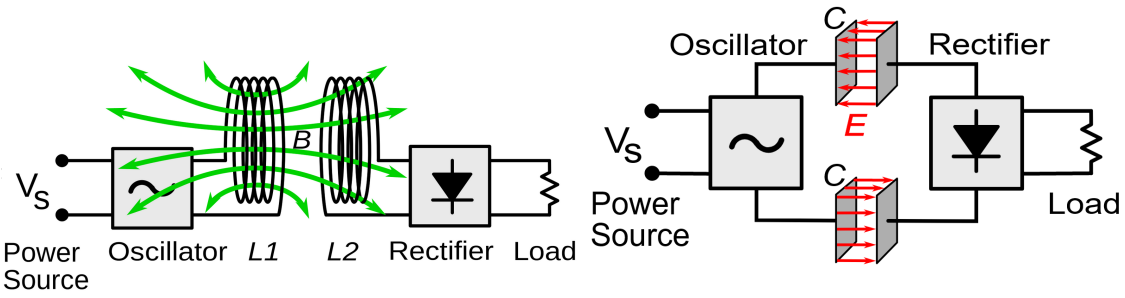

(a) Simple IPT System [42]

(b) Simple CPT System [42]

Fig. 1.11: Near Field Wireless Circuits

is inductive power transfer [27, 28, 30, 43–46]. Capacitive charging offers promise but is currently limited in power delivery [47]. Far-field technologies have been proposed for in motion wireless charging systems and applications in remote areas where running power cables are difficult. For EV static charging, there are still concerns regarding safety systems for far field technology and currently do not show as much promise as inductive [48, 49].

Inductive Power Transfer

Inductive power transfer utilizes magnetic coupling to transmit power between a transmitting and receiving coil of wire, as shown in fig 1.11a. The magnetic coupling is generated by applying an alternating current to the transmitting wire, which generates a magnetic flux as described by Ampere's Law given in (1.1). Where H is the Magnetic field intensity, D is the electric flux density, and J is the current density. When the magnetic flux generated by the transmitting pad interacts with the receiving coil, it produces an alternating voltage and is described by Faraday's law of induction given in (1.2) [41]. Where E is the electric field intensity and B is the magnetic flux density.

$$\nabla * H = J + \frac{\partial D}{\partial t} \tag{1.1}$$

$$\nabla * E = -\frac{\partial B}{\partial t} \tag{1.2}$$

This relationship can in turn be represented as a loosely coupled transformer, as shown in fig 1.12. Where the self inductance of each coil are represented as L_1 and L_2. The mutual inductance generated is given by M_{12} and is usually expressed as a coupling coefficient k_{12}, which has been proposed as a figure of merit in representing how effectively the magnetic fields generated by the transmitting coil are received by the secondary coil. The relationship between mutual inductance and the coupling coefficient is shown in (1.3). The voltage and current equations for the loosely coupled transformer are shown in (1.4) and (1.5) [50].

$$K_{12} = \frac{M_{12}}{\sqrt{L_1 L_2}} \tag{1.3}$$

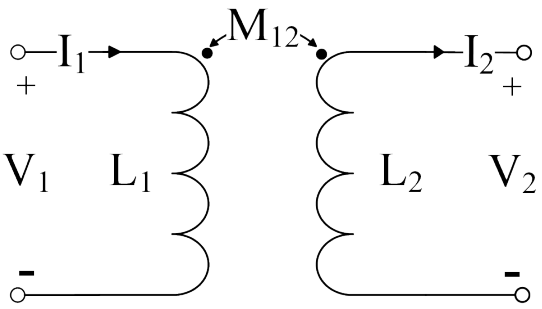

Fig. 1.12: Loosely Coupled Transformer

$$v_1 = L_1 \frac{di_1}{dt} + M_{12} \frac{di_2}{dt} \tag{1.4}$$

$$v_2 = L_2 \frac{di_2}{dt} + M_{12} \frac{di_1}{dt} \tag{1.5}$$

For an IPT system to be able to transmit large amounts of power in the range of tens to hundreds of kilowatts, over large air gaps in the tens of centimeters, the loosely coupled coils need to be tuned to a resonance frequency utilizing resonant networks which, allow the system to maximize power transfer [51]. A generalized circuit representation of a resonant IPT system is shown in Fig. 1.16. This places this style of IPT charging for electric vehicles under the umbrella of resonant converters. For these systems, power transfer and power density are dependent on the tuned resonant frequency. Where increasing switching frequency increases power density. For EV applications, there is a standard frequency utilized of 85 kHz for static WPT as defined by SAE J2954 [52]. For the remainder of this paper, wireless power transfer (WPT) refers to this resonant IPT technology.

For EV charging there are many desirable metrics for system performance including miss alignment tolerance, stability, power output, control ability, simplicity, etc. The primary areas of research have revolved around pad and tuning topology design to achieve several of these metrics [53–61, 61–64, 64–69]. Pad design research has mainly been focused on miss alignment tolerance and power output. Several pad designs have been proposed throughout literature, and hundreds of variations of those pads have been de-

signed [53–65, 70]. The primary styles of pad discussed in literature can be broken up into a few fundamental types circular/square, solenoid, DD, DD quadrature, and bi-polar. Each pad type offers unique benefits that can help shape system design for specific applications based on their flux paths. An overview of the various pad types can be seen in 1.14. For most static applications, circular or square shaped primary and secondary pads have been utilized due to their simplicity. While for in motion charging, DD and DD-Q pads have shown promise due to their misalignment tolerance and interoperability [66].

Several tuning topologies have been proposed throughout literature which, have focused on metrics including misalignment tolerance, control ability, simplicity, and allowed tolerance variation of components. Some basic and widely used tuning typologies are shown in table 1.15. As with pad design, more simple tuning typologies like series-series or parallel-parallel may be preferred for static or quasi-dynamic, where the system is in a more defined environment. While with in motion charging, higher order systems, like LCCL to any, may be selected to filter out high $\frac{dv}{dt}$ and $\frac{di}{dt}$ from the coils to meet EMI specifications.

Controls of WPT

The field of static wireless power transfer has generated many control strategies for various applications. These control strategies have various objectives in their implementations, ranging from optimal power regulation, maximum efficiency tracking, synchronization techniques for active rectification, bidirectional power flow, and startup transient control to name a few [71–81].

Many of these control strategies for electric vehicle charging have been accomplished with a standard circuit approach shown in fig 1.16 [81–84]. Where there is an H-bridge inverter followed by the networks primary compensation, primary coil, receiver coil, receiver compensation, diode bridge rectifier, followed by if necessary for the research being done a DC-DC converter to help with power regulation and output voltage control.

The authors of [81] proposed a dual loop controller strategy for a traditional style system that achieves maximum system efficiency in the face of misalignment. The authors of [82] propose a modified approach for the DC-DC regulator, in which it is simplified to a

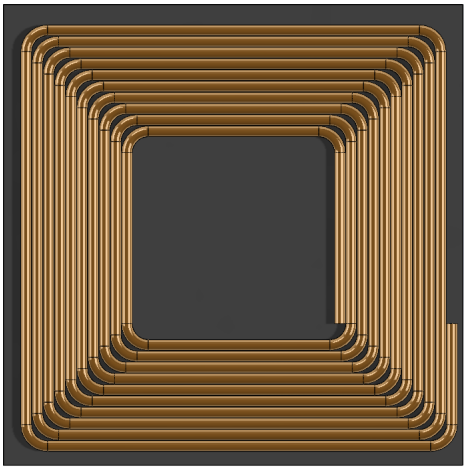

(a) Circular Pad

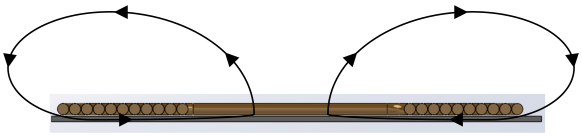

(b) Circular Pad Flux Path

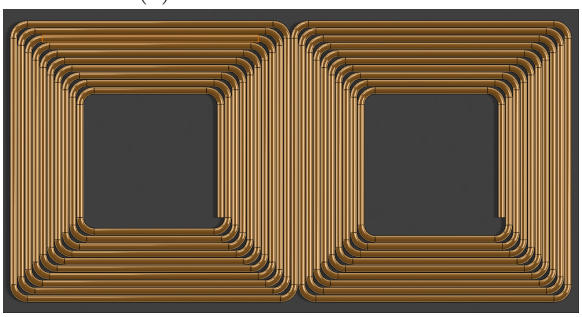

(c) DD Pad

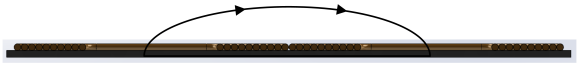

(d) DD Pad Flux Path

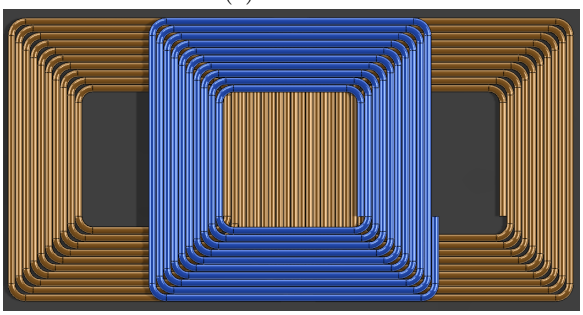

(e) DD-Q Pad

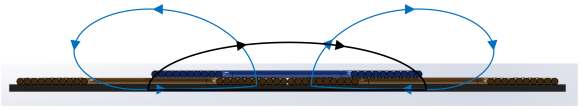

(f) DD-Q Pad Flux Path

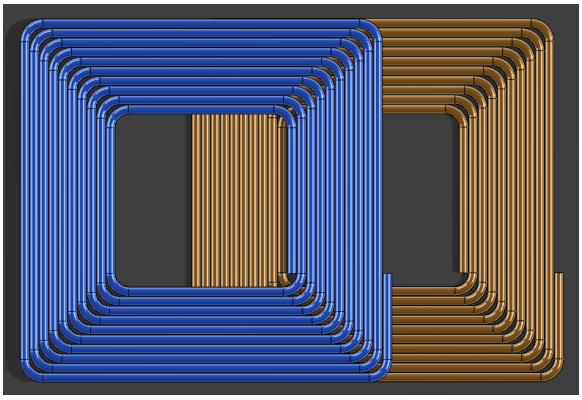

(g) Bipolar Pad

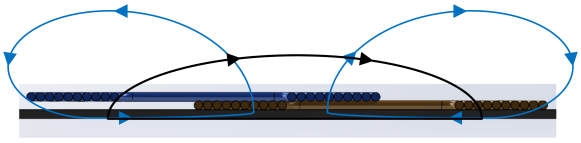

(h) Bipolar Pad Flux Path

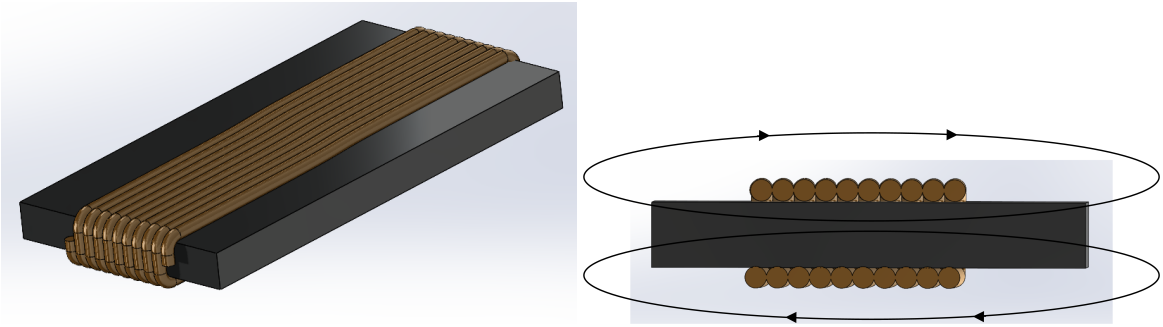

(a) Solenoid Pad (b) Solenoid Pad Flux Path

Fig. 1.14: Typical Pad designs

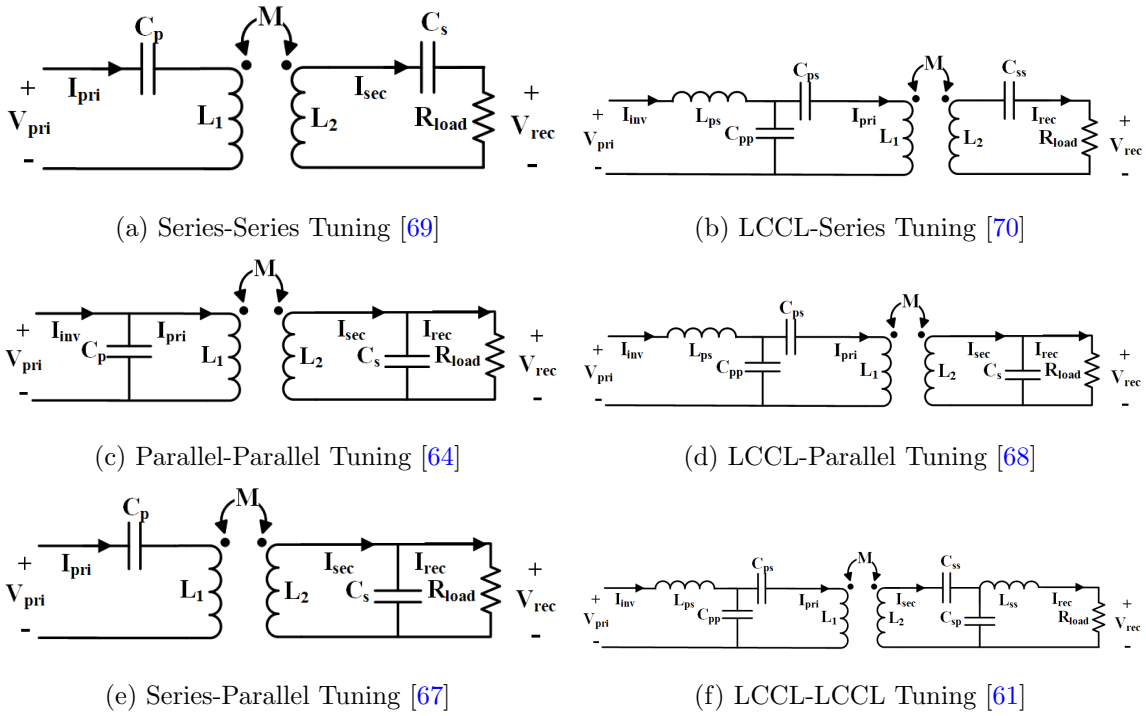

(a) Series-Series Tuning [69] (b) LCCL-Series Tuning [70]

(c) Parallel-Parallel Tuning [64] (d) LCCL-Parallel Tuning [68]

(e) Series-Parallel Tuning [67] (f) LCCL-LCCL Tuning [61]

Fig. 1.15: Typical Tuning Typologies

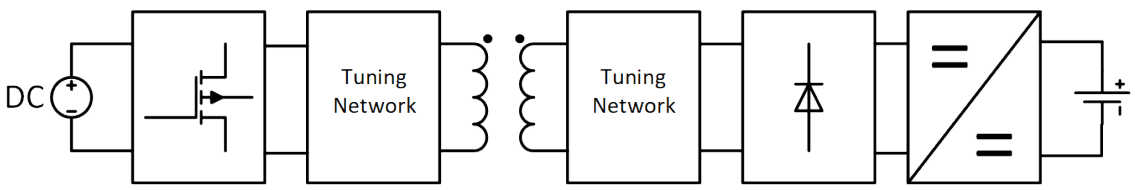

Fig. 1.16: Traditional System

single switch to regulate output voltage. Their system improved overall system efficiency, power density and removed communication requirements between primary and secondary. The authors of [83] utilize a simple logic controller applied to the traditional system to achieve a constant current or constant voltage output. Other authors have done comparative analysis on two different control strategies to regulate power flow. The two strategies are frequency and phase shift controllers for the primary in a series-series compensated tank [84].

However, some techniques and strategies proposed in literature have diverged from this approach. The authors of [71], [80], and [79] have utilized active lower switches on their rectifier to successfully regulate power transfer from the secondary side and reduce the communication requirements. The reduction of communication in wireless power transfer is a key component for DWPT, and strategies proven in static could be extended to dynamic. Including use of active lower switches on the secondary side rectifier. Additionally, these circuits decrease system complexity by no longer requiring a DC-DC converter to regulate output power. The circuit discussed in [71] is shown in Fig 1.17.

Extending further, research has been done utilizing fully synchronous rectifiers or bidirectional wireless power systems. The primary driving force of research looking into synchronous rectification for electric vehicles is vehicle to grid applications (V2G). Vehicle to grid applications for electric vehicles offer a unique way that EVs can help maintain grid stability, as we transition to more variable sources of energy with renewables. Several papers have been written about the modeling of a bidirectional system for WPT [72, 73, 76]. These papers have proposed small signal phasor modeling, steady state models and dynamic multi-variable state space models.

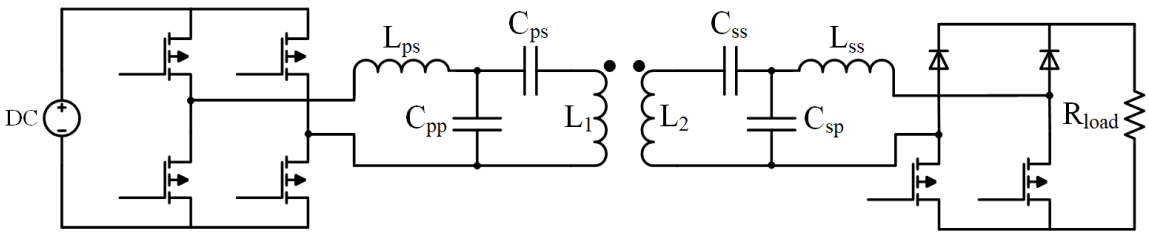

Fig. 1.17: Semi-Active Rectifier

Many papers have been written on different control approaches for bidirectional WPT [74,75,77,78,85,86]. A power-frequency droop controller is proposed in [77]. This approach ensures power regulation is kept within margin for either transmitting or receiving power electronics. The authors of [78] propose a new controller that allows for synchronization and power regulation in both directions by utilizing a third pickup coil as a sensing circuit. An optimal efficiency controller is presented in [75]. The control strategy maximizes system efficiency despite miss tuned components in the circuit. A control strategy that utilizes active and reactive components of the primary pickup is utilized in [74] to regulate the bidirectional synchronization and power flow. The authors of [85] use a genetic algorithm to optimize a discrete PID controller for power regulation. Finally, [86], proposes a frequency jitter control to regulate multiple secondaries on a single primary. In general, bidirectional solutions for controls of wireless power transfer offer a very compelling approach given the potential needs for V2G applications and the increased level of control with a fully active secondary.

1.2.2 Dynamic Wireless Power Transfer

Types of DWPT systems

Dynamic wireless power transfer is not a large extension of research from SWPT. However, the application of DWPT has several challenges that make its adoption, and use, a distinct and active field of research. Currently, there are several prominent dynamic wireless power transfer system styles proposed in literature that utilize inductive power transfer. These systems are broken up into three categories. First, are track or rail based systems. Second, is segmented or lumped pads and third, is reflexive or field focusing circuits.

Most of the original research done with dynamic wireless power transfer was in the form of track based systems [87,88]. These applications utilize a long high current track laid out along a specified route and the secondary coil is slotted into the track. This style allows for multiple secondaries to receive power from a single primary, while keeping the overall system

as simple as possible [89,90]. An example system is shown in fig 1.18. These systems are an excellent solution for very well-defined routes and moderate power levels. The difficulties with this style of DWPT system for EV charging, is the large inductance created with a large primary coil. The large inductance make it difficult to drive the pads with enough voltage to induce the necessary current to transmit the necessary power requirements for EVs at higher frequencies. Most of these systems have been operated at lower frequencies which, will not meet the new SAE J2954 specification of 85 kHz. Currently, there is no standard for DWPT's operating frequency, but to have interoperable systems with static charging major consideration is being placed on 85 kHz for DWPT. Increasing the frequency of these systems will significantly increase the losses and increase the cost of the systems by increasing the necessary copper or removing ferrite in their long tracks to counteract said losses [91]. This leaves this style of system as not an ideal approach for in motion EV charging.

The opposite of a track based system is a lumped or segmented system. This approach utilizes individual primaries in the road one after another [92–106]. By segmenting the primary coil, it creates a more complex and costly system overall, but at the benefit of increased efficiency and system robustness. Segmented systems are more efficient by allowing for control schemes to activate and deactivate primary pads when in the presences of a secondary coil. The system improves robustness by removing single point failure that would be present in a track based system. However, these benefits come at a greatly increased system cost due to extra power electronic costs. This system does not have to be a one to one pad and power electronics pair. There are cases in which a single primary inverter could energize several primary pads. An example lumped or segmented system is shown in fig 1.19. Where the primary electronics section includes system tuning.

In-between track and segmented systems is a more recent development of reflexive or field focusing systems [107–111]. These DWPT systems operate by utilizing a single inverter to energize multiple primary pads. This system operates by utilizing the reflective impedance of the secondary to tune the primary pad, allowing for high power transfer in

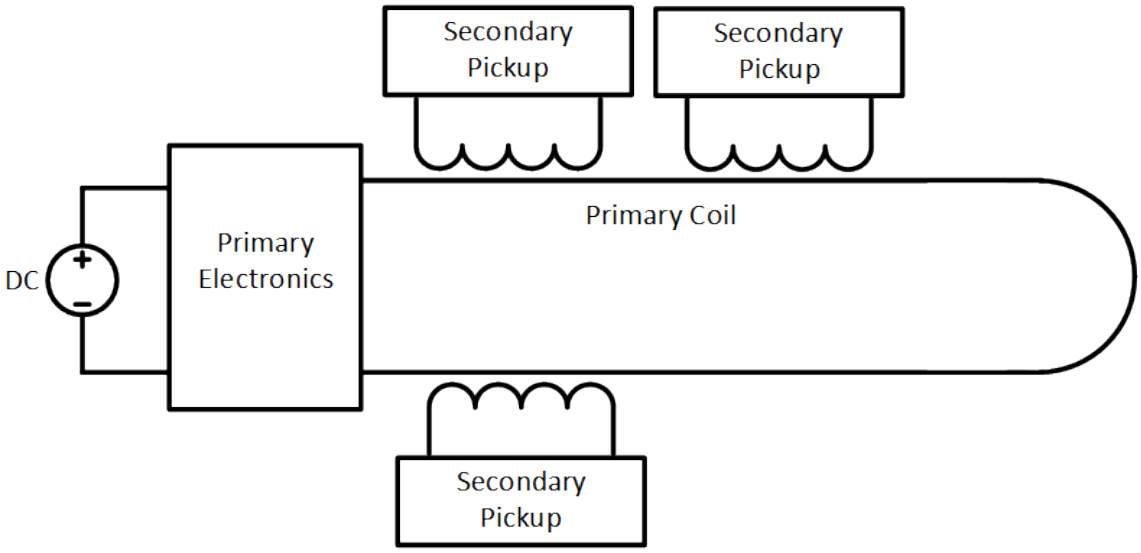

Fig. 1.18: Track Based DWPT System

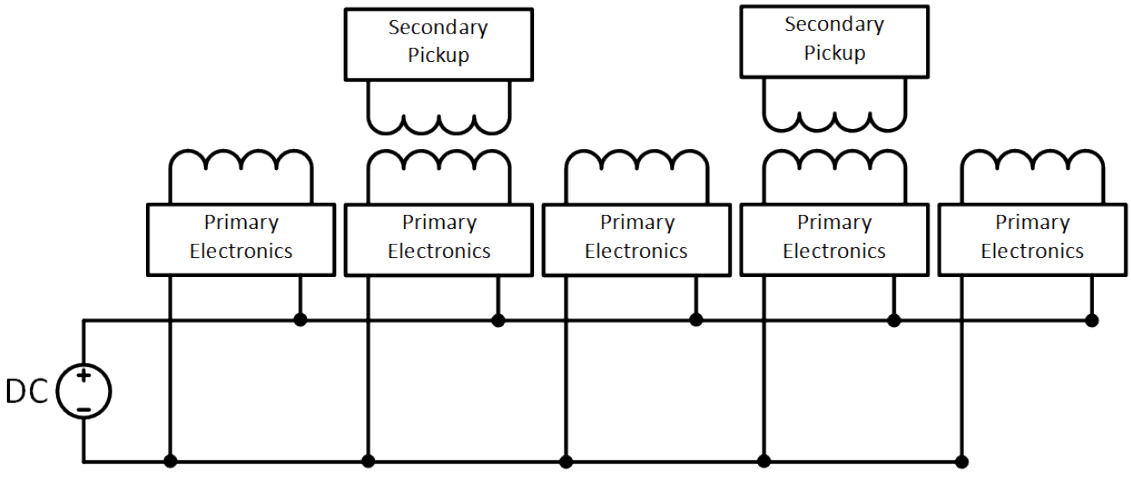

Fig. 1.19: Segmented DWPT System

the presence of a secondary. This achieves a state where primaries not in the presence of a secondary receiver have very little current circulating in their tuning networks and pads. This strikes an interesting balance between track based and segmented based DWPT systems. In that, there are lower losses when compared to a track based system and decreased system cost when compared to segmented. However, it utilizes very finely tuned resonant networks that may be difficult to maintain with mass adoption. It also still maintains a single point failure. An example reflexive system is shown in Fig 1.20.

Modeling DWPT systems

The analytical modeling used for static wireless power transfer can provide insights into specific operating points for DWPT. These models are limited though, due to not taking into account, or simply being unable to model the effects caused by multiple primary, and or secondary pad interactions, and or transient behavior while pads are activating and deactivating in the case of segmented systems.

Prior research has been done in analytical modeling of transient effects for DWPT systems, in the vein of, simplified models and generalized state space averaging [112–114]. Additional work has been done to utilize finite element modeling, and dynamic circuit simulations using position varying finite element models. This allows for rapid develop of system tuning, pad design, and closed loop controls [115]. This prior research offers a solid

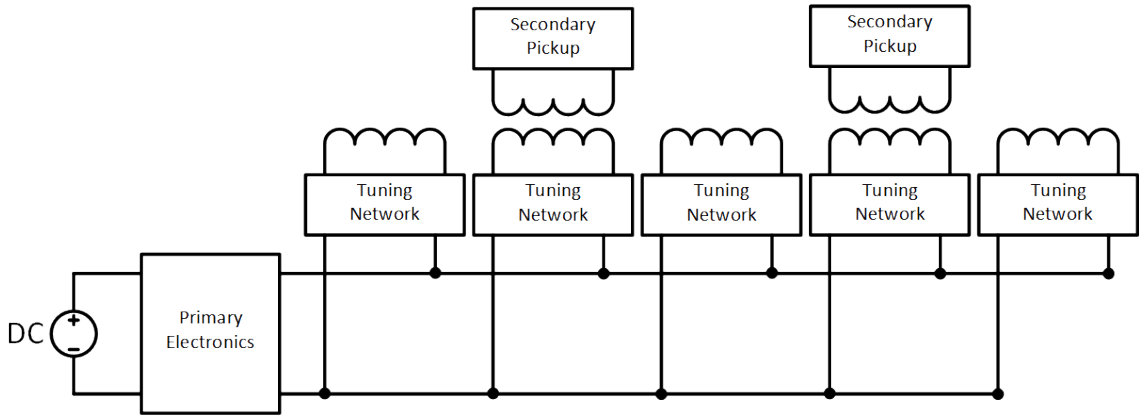

Fig. 1.20: Reflexive DWPT System

foundation for system design.

To model the interactions between the various coils, the loosely coupled coils given in 1.12 can be expanded. By representing the governing equations of (1.4), (1.5) in matrix form as shown in (1.6) the matrix can be expanded to add any additional primary or secondary pads to the system as seen in fig 1.21 and as shown in general matrix form (1.7) [115]. This gives a time varying inductance matrix for an arbitrary length DWPT system.

For simulation purposes and simplification, it is proposed in [115] that this matrix can be represented as a position based coupling matrix, where a defined coupling relationship can be determined based on a defined position of the secondary coil. This matrix can be determined through finite element analysis and provides a speed independent interaction between the various coils allowing for system simulation at arbitrary speeds and misalignment, allowing for rapid development. The final position based inductance matrix is given in (1.8).

$$\begin{bmatrix} v_1 \\ v_2 \end{bmatrix} = \begin{bmatrix} L_1 & M_{12} \\ M_{12} & L_2 \end{bmatrix} \begin{bmatrix} \frac{di_1}{dt} \\ \frac{di_2}{dt} \end{bmatrix} \tag{1.6}$$

$$\begin{bmatrix} v_1 \\ v_2 \\ \vdots \\ v_{m+n} \end{bmatrix} = \begin{bmatrix} L_1 & M_{12} & \cdots & M_{n+m} \\ M_{12} & L_2 & & \\ \vdots & & \ddots & \\ M_{m+n} & & & L_{m+n} \end{bmatrix} \begin{bmatrix} \frac{di_1}{dt} \\ \frac{di_2}{dt} \\ \vdots \\ \frac{di_{m+n}}{dt} \end{bmatrix} \tag{1.7}$$

$$\begin{bmatrix} v_1 \\ v_2 \\ \vdots \\ v_{m+n} \end{bmatrix} = \begin{bmatrix} L_1 & M_{12} & \cdots & M_{m+n} \\ M_{12} & L_2 & & \\ \vdots & & \ddots & \\ M_{m+n} & & & L_{m+n} \end{bmatrix} \begin{bmatrix} \frac{di_1}{dx} \\ \frac{di_2}{dx} \\ \vdots \\ \frac{di_{m+n}}{dx} \end{bmatrix} \tag{1.8}$$

Controls of DWPT

Controls for dynamic wireless systems share design choices and considerations that

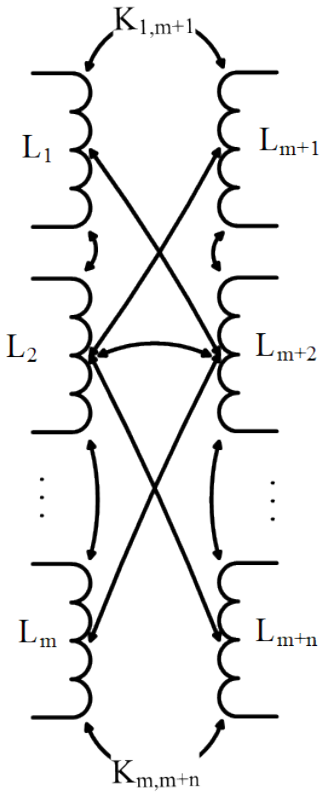

Fig. 1.21: Multi-Inductor Coupling Matrix

static systems are optimizing for. These are ranging from misalignment tolerance, power regulation, maximum efficiency and startup control. However, dynamic systems have additional requirements that have to be accounted for. Specifically, synchronization of multiple primary pads that includes turning on and off pads, when in the presence of a secondary receiver. They also have to deal with limitations in communication between primary and secondary, since vehicles speeds would severely limit communication bandwidths. The communication limitation, therefore, limits power regulation strategies. This makes defining optimal control strategies to regulate power for various vehicles classes and power levels, that interact with this infrastructure in rapid succession, a complex challenge.

Within the body of research, there have been papers proposed regarding techniques for synchronization of primary pad activation [103–106]. These papers have described methods utilizing additional regulators to control pad activation based on power sent to the receiver [106]. The authors of [105] propose a load detection method utilizing energy equilibrium. This system makes use of a class-E inverter instead of an H-bridge inverter. The author of [104] proposes a method of activation through changing inductance values to determine the location of the secondary. Additionally, [103] presents a controller that uses transient analysis of a DWPT system to active and deactivate primaries.

Further, there has been research done in power regulation techniques for DWPT systems. These techniques have been applied to both the primary side and secondary side individually, or in some cases both. The authors of [102] proposed a control strategy that utilizes a novel sampling technique and predefined lookup tables to regulate power from the primary side. A two loop controller is proposed in [101] that regulates the primary track current and total output power. Another dual loop control strategy is proposed in [100] where coupling coefficient estimation is utilized to regulate output power. Coupling coefficient estimation is also utilized in [98,99] to regulate power with the secondary side DC-DC converter.

A model predictive controller is presented in [97] to regulate output power through a secondary side DC-DC converter. [96] proposes a constant maximum power point controller

based around a detuned series-series compensation. The authors of [95] propose a controller to help regulate power transfer to a multi-pad receiver. A multi pad receiver is a technique that would allow a modular design for interoperable power levels. The opposite of this is proposed in [94] in which a primary side multi pad control strategy is proposed to regulate power transfer. This approach helps ensure smooth transitions from one pad to the next.

There has also been research into half active rectifiers as a method to regulate power transfer or improve efficiency for DWPT systems. The half active rectifier was utilized to maximize efficiency in [93] while a DC-DC converter still regulated power. A pulse density modulation controller was proposed in [92] to improve system efficiency.

1.3 Proposed Work

1.3.1 Research Objectives

This research's primary objective is to develop a comprehensive control strategy for dynamic wireless power transfer. In motion wireless charging has several challenges that make the technology complex and difficult for mass application. Those challenges range from, but are not limited to, vehicle detection, power regulation, interoperability, and communication. To resolve or simplify several of these challenges, this thesis presents a novel method for synchronous rectification. By utilizing synchronous rectification and the additional control variables it provides, DWPT systems can regulate power from the vehicle, allow for interoperable power levels without additional DC-DC converters, and achieve vehicle detection for activation and deactivation of primary pads. All of this instead be achievable without direct communication from the primary to the secondary.

1.3.2 Thesis Organisation

This thesis is organized as follows: Chapter 2 elaborates on the design of the control strategy and design of the dynamic wireless power system. Chapter 3 contains simulation methods for the controller and simulation results. It also contains simulation results for the closed loop control of the dynamic system. Chapter 4 discusses practical hardware

implementation of the control strategy system and results for its application. Chapter 5 offers a conclusion and notes about future work.

CHAPTER 2

Analysis and Design of an LCCL-LCCL DWPT System and Synchronous Controller

2.1 System Design

2.1.1 System Analysis

For the design of a fully synchronous rectifier to be completed, some initial system design specifications and assumptions need to be outlined. First, this system will be operating with a segmented primary pad design and not a track based system. Second, is that the DWPT system tuning is LCCL-LCCL as shown in figure 2.1. This decision is due to the decoupling of the inverter's and rectifier current from the track current, the improved performance in system stability as outline previously, as well as the tuning design's robustness to tuning tolerances [66].

Given the initial system design requirements, some further assumptions can be made. The next assumption for a segmented primary DWPT system, is the primary pads should be synchronized in both phase and frequency. This is to ensure that there is no power transfer between primary pads. If the primary pads were not synchronized correctly in phase angle, there would be direct power transfer from one primary pad to another. This power transfer would not be large, due to low coupling, but it would directly decrease efficiency within the system. Additionally, once both pads have coupled to a secondary pad, as it moves in

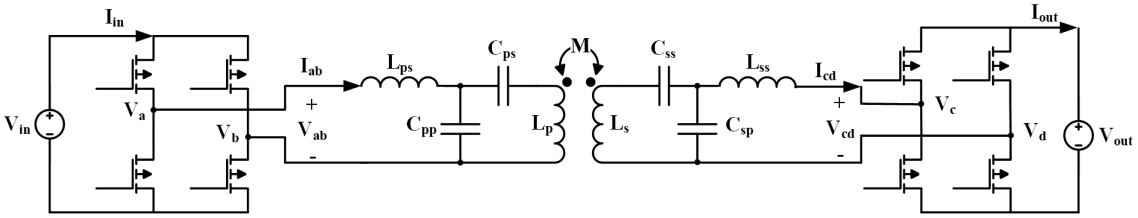

Fig. 2.1: LCCL-LCCL tuned system with Active Rectifier

between the primaries, the power transfer to the receiver coil could be dramatically reduced or nullified due to the phase angle difference between primaries.

If the primary pads were not synchronized in frequency, there would be cyclic power transfer between them as the phase relationship between primary pads moved. The analytical reasoning for synchronization between primaries is the same as what is described for the synchronization from primary to secondary described in this paper. Synchronization of primary pads is a straightforward process and can be achieved through direct wired or wireless connections. Also, for a segmented system to maintain high efficiency, it can be assumed that primary pads have been designed and controlled to activate and deactivate when in the presence of a receiver coil. Any technique proposed in literature can be applied to achieve this effect [103–106].

These assumptions allow for the design of a synchronous rectifier to be simplified. First, by assuming that the primary pads are synchronized to a fixed phase and frequency, the secondary receiver will not have to regulate to arbitrary phase angle shifts as it transitions between primary coils. Second, is assuming that primary pads are activated efficiently, the effects on power transfer from pad activation should be minimized, such that the rectifier does not have to regulate to large perturbations in power transfer. These two initial assumptions allow a simplified analysis of the DWPT system. The analysis can then be completed as a single primary and secondary system. This simplification is holds in that the secondary effectively interacts with a single primary, given the primaries are synchronized, and power transfer will be bound to a specified range during the majority of operation. This in turn will not have a major impact on the secondaries control loops during operation.

For the DWPT system shown in Fig. 2.1 there are two independent inputs to the system V_{AB} and V_{CD}. These inputs of the system are square wave voltages generated by the primary inverter and secondary rectifier, respectively. The square wave voltages they generate can be represented by the Fourier series equations given in (2.1) and (2.2) where, V_{in} and V_{out} are the DC input voltage of the primary and output voltage of the secondary. ω_s is the assumed synchronized operating frequency, and ϕ_{AB}, ϕ_{CD}, and θ are phase angle

relationships between the half-bridges.

$$V_{AB} = V_{in}\frac{4}{\pi}\sum_{n=1}^{\infty}\frac{1}{n}\cos\left(n\omega_s t + \frac{n\phi_{AB}}{2}\right)\sin\left(\frac{n\phi_{AB}}{2}\right) \tag{2.1}$$

$$V_{CD} = V_{out}\frac{4}{\pi}\sum_{n=1}^{\infty}\frac{1}{n}\cos\left(n\omega_s t + n\theta + \frac{n\phi_{AB}}{2}\right)\sin\left(\frac{n\phi_{CD}}{2}\right) \tag{2.2}$$

From these equations there are four distinct control mechanisms to the system that can be regulated during operation, frequency ω_s, and the phase angle relationships, ϕ_{AB}, ϕ_{CD}, and θ. The phase angles ϕ_{AB} and ϕ_{CD} govern the relationship between the two half bridge on the primary inverter and secondary rectifier, respectively. These angles govern the magnitude of the input and out voltage square waves of V_{AB} and V_{CD}. The phase angle θ defines the angle between the inverter and rectifier measured from the center of the primary square wave voltage V_{ab} to the start of the secondary square wave voltage V_{CD}. The voltage waveforms generated, and phase relationships, are shown graphically in Fig. 2.2.

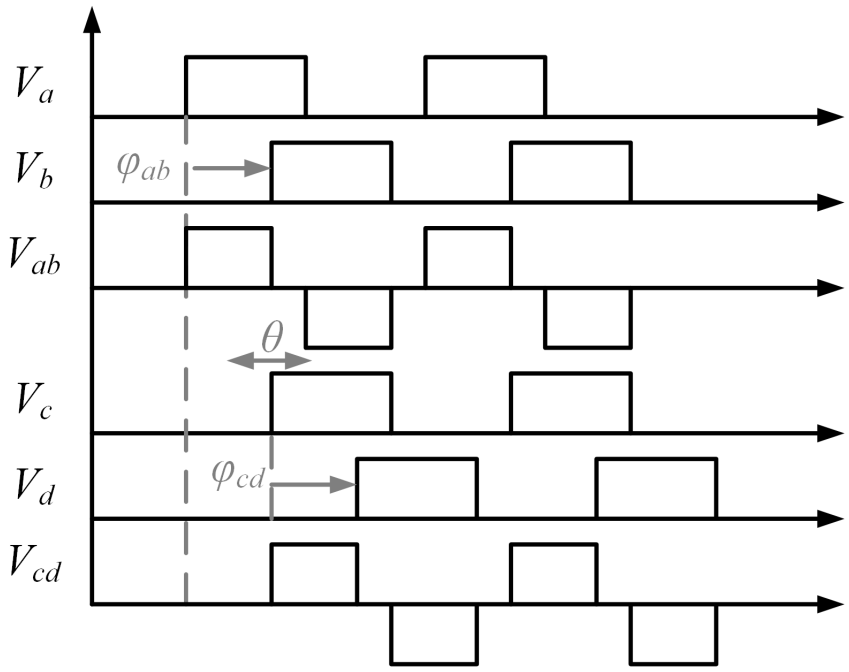

Fig. 2.2: Phase Relationships of Inverter and Rectifier

As stated previously, system tuning to a resonant frequency is imperative for wireless power to transmit the necessary power for EV charging [116]. For the LCCL-LCCL tuning compensation utilized through the remainder of this thesis, a design procedure for system tuning is presented that follows the procedure presented throughout literature [66, 78, 115]. Following this procedure, the primary consideration for DWPT system design is output power, which can be expressed as (2.3). In which Q is the loaded quality factor and S_u is the uncompensated power. S_u is calculated as shown in equation (2.4), where ω_s is the operating frequency, I_p is the current through the primary coil, k is the coupling coefficient as defined in (1.3) and L_p is the primary pad inductance.

$$P_{out} = QS_u \tag{2.3}$$

$$S_u = \omega_s I_p^2 k^2 L_p \tag{2.4}$$

From practical design limitations, usable pad current levels, I_p, can be specified from limitations imposed from available litz wire sizes, the usage of bi-filer or higher wire count coil designs, and power requirements. Additionally, from intended application k and L_p can also be specified given air gaps, misalignment tolerances, pad design, and power levels. ω_s is set to match the SAE standard of 85 kHz. Given these, system parameters are properly specified and the system's two DC Voltages V_{in} and V_{out} are selected. The voltages described in (2.1) and (2.2) are then simplified to their fundamental approximation, and the tuning design is expressed as follows. The primary series inductor L_{ps} is calculated as shown in (2.5). In which the necessary impedance of the inductor at resonance is calculated given the output voltage and recirculating tank current required for the system.

$$L_{ps} = \frac{V_{AB}}{\omega_s I_p} \tag{2.5}$$

The primary parallel capacitor C_{pp} is set to be in resonance with the primary series inductor as shown in (2.6)

$$C_{pp} = \frac{1}{\omega_s^2 L_{ps}} \tag{2.6}$$

The primary side series capacitor C_{ps} is utilized as a partial tuning capacitor to reduce the reactance of the primary pad and bring it equal to the reactance of the primary series inductor L_{ps}. How this is accomplished is described by (2.7) and (2.8).

$$\omega L_{ps} = \omega_s L_p - \frac{1}{\omega_s C_{ps}} \tag{2.7}$$

$$C_{ps} = \frac{1}{\omega_s^2 (L_p - L_{ps})} \tag{2.8}$$

The secondary side tuning network begins with the calculating the induced open circuit voltage V_{oc} in the secondary pad as shown in (2.9), along with the RMS output current required to deliver the designed power I_{CD}. The calculation of the bridge current is given in (2.10).

$$V_{oc} = j\omega M I_p = j\omega_s I_p k \sqrt{L_p L_s} \tag{2.9}$$

$$I_{CD} = \frac{\pi}{2\sqrt{2}} \frac{P_{out}}{V_{out}} \tag{2.10}$$

The secondary side series inductance L_{ss} can be calculated utilizing V_{oc} and I_{CD} as shown in (2.11). The parallel series capacitor C_{sp} and partial pad capacitance C_{ss} can be calculated the same as the primary, as shown in (2.12) and (2.13).

$$L_{ss} = \frac{V_{oc}}{\omega_s I_{CD}} \tag{2.11}$$

$$C_{sp} = \frac{1}{\omega_s^2 L_{ss}} \tag{2.12}$$

$$C_{ss} = \frac{1}{\omega_s^2 (L_s - L_{ss})} \tag{2.13}$$

The system being in resonance under ideal tuning conditions allows equation (2.14) to be true. With this equation being true, system currents can then be derived.

$$\omega^2 = \frac{1}{L_{ps} C_{pp}} = \frac{1}{C_{ps}(L_p - L_{ps})} = \frac{1}{L_{ss} C_{sp}} = \frac{1}{C_{ss}(L_s - L_{ss})} \tag{2.14}$$

Derivation of the system currents can be completed using the techniques and insights proposed by [117]. To analyze the DWPT circuit, the system is represented in a more direct state, shown in Fig. 2.3. In this circuit, the H-bridges are simplified to the induced voltages V_{ab} and V_{cd}. The induced voltages due to coupling between primary and secondary are represented by V_{pm} and V_{sm}.

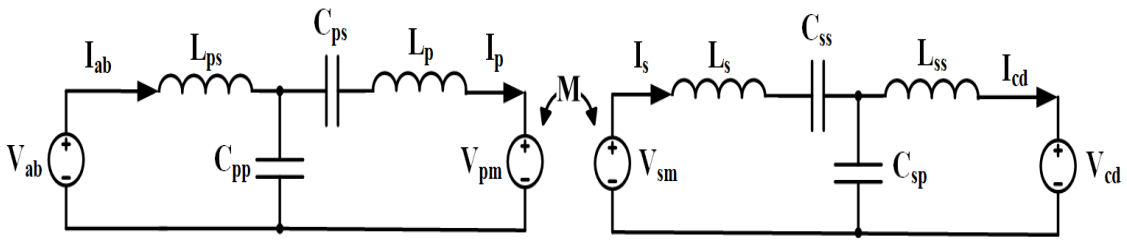

Fig. 2.3: LCCL-LCCL Analysis Circuit

In [117] it is noted that the primary and secondary track currents I_p and I_s are independent of the induced voltages V_{pm} and V_{sm}, under the assumption that they are ideal sinusoidal currents. This assumption holds that the higher order harmonics of the currents are significantly attenuated. From this assumption the currents are derived and can be expressed by,

$$I_p = -\frac{4MV_{in}\sin\left(\frac{\phi_{AB}}{2}\right)}{\pi\omega_s L_{ss} L_p}\sin\left(\omega_s t + \theta + \frac{\phi_{AB}}{2}\right) \tag{2.15}$$

$$I_s = -\frac{4MV_{out}\sin\left(\frac{\phi_{CD}}{2}\right)}{\pi\omega_s L_{ps} L_s}\sin\left(\omega_s t + \frac{\phi_{AB}}{2}\right) \tag{2.16}$$

From these currents the induced voltages V_{pm} and V_{sm} are given by,

$$V_{pm} = -V_{out}\frac{4M}{\pi L_s}\cos\left(\omega_s t + \theta + \frac{\phi_{CD}}{2}\right)\sin\left(\frac{\phi_{CD}}{2}\right) \tag{2.17}$$

$$V_{sm} = -V_{in}\frac{4M}{\pi L_p}\cos\left(\omega_s t + \frac{\phi_{AB}}{2}\right)\sin\left(\frac{\phi_{AB}}{2}\right) \tag{2.18}$$

The bridge currents I_{ab} and I_{cd} are noted to be dependent upon V_{pm} and V_{sm} in [117], which can now be derived and are expressed as,

$$I_{ab} = -\frac{4MV_{out}\sin\left(\frac{\phi_{CD}}{2}\right)}{\pi\omega_s L_{ps} L_s}\sin\left(\omega_s t + \frac{\phi_{AB}}{2}\right) \tag{2.19}$$

$$I_{cd} = -\frac{4MV_{in}\sin\left(\frac{\phi_{AB}}{2}\right)}{\pi\omega_s L_{ss} L_p}\sin\left(\omega_s t + \theta + \frac{\phi_{AB}}{2}\right) \tag{2.20}$$

From the induced rectifier current I_{cd} and the rectifiers induced voltage V_{CD}, output power can be calculated as shown in (2.21). From this, equation (2.22) is derived. From the output power equation it can be noted that the system power is dependent upon input voltage, output voltage and the relative coupling of the pads. The methods to actively regulate this power transfer are the same as mentioned prior, ω_s, ϕ_{AB}, ϕ_{CD}, and θ.

$$P_{out} = Re : \{V_{CD}(-I_{CD})^*\} \tag{2.21}$$

$$P_{out} = \frac{8M}{\pi^2 w_s L_s L_p} V_{in} V_{out}\sin(\theta)\sin\left(\frac{\phi_{AB}}{2}\right)\sin\left(\frac{\phi_{CD}}{2}\right) \tag{2.22}$$

2.1.2 Controller Design

Given the control parameters that can individually regulate power transfer, there are a few guiding principles as to selecting a single method for regulation. First, given the SAE standard of 85 kHz and the surrounding frequency band of 81.93 kHz—90 kHz, there is limited range for regulation through frequency control [52]. Frequency control could be utilized if the system had a large quality factor at resonance, allowing for large power regulation through minimal frequency changes. However, most DWPT systems operate with a relatively low quality factor. The relatively low quality factor entails that frequency regulation is not an effective solution to regulate power transfer, since necessary frequency changes would exceed the bounding range of the SAE standard. However, this does not limit its potential, for this thesis the premise that any frequency within that band could be used for operation. This is considered under the assumption that any frequency could be used to meet specific design requirements chosen by the system designer. Second, the phase angle relationship between primary and secondary converters, ϕ_{BC}, is necessary to regulate power

transfer direction. However, given that for current DWPT systems, bidirectional support is not needed, it is simpler to maintain it at unidirectional power transfer. Therefore, to regulate power, duty cycle modulation or pulse width modulation or phase angle modulation, utilizing ϕ_{AB}, and ϕ_{CD} is selected.

Direct power regulation through ϕ_{AB}, and ϕ_{CD} is straightforward to implement with traditional PID controllers utilizing DC current and voltage sensors to determine power levels, and has been studied extensively in dual active bridge converters [76]. It is well documented that to maximize power transfer $\theta + \frac{\phi_{AB}}{2}$ should be equal to $\pm\frac{\pi}{2}$ for the given power flow direction [73, 74, 78].

Additionally, for a DWPT system, synchronization between the primary and secondary is a challenge. For a dual active bridge converter, which this system is at its most fundamental state, the system is generally run through a single microcontroller or FPGA. If multiple controllers are necessary for its operation, a synchronization wire is utilized. The purpose for the synchronization is that due to component tolerances, there will exist minor deviations in frequency generation from controller to controller. The minor frequency differences will stop effective power transfer as power transfer will become cyclic in nature as the phases between the bridges will cycle. This is the same concept as the initial assumption that primary inverters will be synchronized in their operation. For a DWPT system, a direct wired connection is impossible between primary and secondary. A wireless connection could be feasible, but would entail complex and costly systems to ensure proper synchronization. Therefore, a method to adjust the rectifier's induced voltage to operate at the same frequency as the primary with the correct θ to maximize power transfer is necessary and ideally would operate without communication.

The challenge of frequency and phase correction between distant controllers is a common challenge in wireless communication and signal processing. The challenge generally shown in this field is the recovery of the baseband or carrier frequency that the information was transmitted on [118–120]. The general solution for this is the use of phase locked loops (PLLs).

As a whole, phase locked loops operate in a simple manner. PLLs take in a signal that potentially has various harmonic components, and synchronize to a single specified frequency that is contained in the signal. They can then output information about this signal, including instantaneous phase and frequency, depending upon the application. This allows for the correct demodulation of communicated signals. The basic structure of an analog PLL is shown in Fig. 2.4. The first block of the figure determines the relative phase of the input frequency versus the output frequency. The next block filters out any undesired frequencies. It is then passed to a frequency generation controller, which outputs the desired frequency. This frequency output could be various functions including sine, triangle, or square wave, based on the implementation. This structure can be achieved both with analog circuitry and digital circuitry.

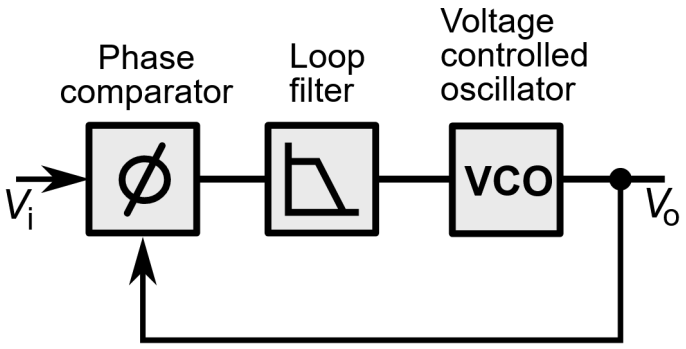

Fig. 2.4: Standard Phase Locked Loop [8]

The use of PLLs in wireless power transfer has already been done to achieve bidirectional power transfer in [78]. This application utilized an external PLL to directly synchronize with the 85 kHz operating frequency utilizing an additional sensing coil. It then used interrupt points from the PLL to maintain synchronization. However, this technique, while effective, poses concerns about its utilization over a range of operating frequencies as well as the additional cost of extra sensing hardware. The concern over operating range is directed at the premise that an exact operating frequency is known by both the primary

and secondary before operation, in this paper, it was 20 kHz. The same brand of controller was also utilized on primary and secondary, and thus the exact derivation of frequency on both controllers would be as close to identical as possible. This is a valid assumption for a system design where both primary and secondary are designed together.

However, for interoperability of DWPT systems', leeway of frequency over the full range stated by the SAE standard may be required. This is potentially feasible with a standard PLL design proposed in [78], but gate assignments become difficult as the system deviates from the chosen frequency. An explanation and look into this concern will be done later in this chapter, with a detailed explanation of how gate signals are generated. This thesis looks to address these concerns by using a fully digital PLL to derive the correct operating frequency through direct carrier adjustment as a means of carrier recovery, instead of using a PLL to directly derive the carrier.

To properly develop a digital PLL capable of regulating both θ and ω_s, to maintain synchronization, it must be discussed how the rectifier generates its gates signals and how the two unregulated variables would manifest during the operation of the controller. For this application, the controller utilized is an FPGA, but a microcontroller implements the same principles and only minor adjustments should be necessary to implement the principles discussed.

For this thesis, both the rectifier's controller and inverter controller generates an internal saw-tooth carrier or equivalent triangular carrier at the operating frequency of 85kHz through a simple counter, which is driven by a much faster clock. This carrier controls the frequency and relative phase angles of the half bridges. The speed of the higher frequency clock specifies the precision of the carrier waveform. An example carrier is shown in Fig. 2.5. The saw-tooth carrier shown represents the 0 to 2π radians of a full switching cycle. To generate V_{CD} or V_{AB} the controller compares this carrier with modulation values relative to the desired phase angle as shown in the figure, where the half bridges have a phase shift of $\phi_{cd} = \pi/2$. This then generates the quasi square wave voltage shown for V_{CD} .

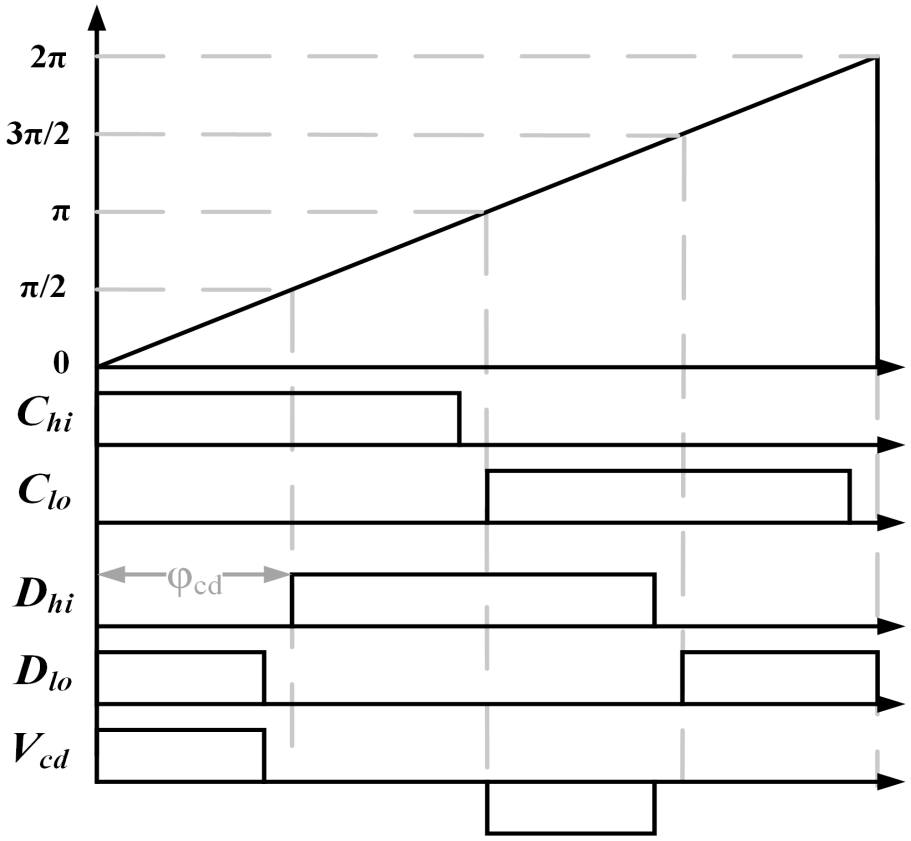

Fig. 2.5: Rectifier Gate Generation

To adjust the secondary's carrier in terms of frequency or phase, there are three approaches that could be implemented. The first would be to adjust the slop of the carrier. This would entail modifying the underlying high frequency clock generation by increasing or decreasing its frequency, and thus increasing or decreasing the period of the carrier. This implementation would be extremely difficult to properly accomplish within a controller, if possible at all, due to the difficulty of adjusting internal clock generation on FPGA's, since its status is preset before operation commences, this is the same for a microcontroller.

The second method available to adjust the carrier is changing the peak of the internal counter, which will adjust its frequency and phase. This method on its own is not feasible for regulation. For example, the 85kHz operation of this system utilizing an internal high frequency clock of 340MHz would only have a precision of ±21.2Hz. However, the use of a PLL controller to regulate the amplitude dynamically to the desired frequency overtime

with continuous minor adjustments would be effective. This is done in [78], where the carrier was reset every cycle based on the PLL's output.

As stated previously, this works well for a given operating frequency. However, as the frequency adjusts, the point at which the carrier is reset adjusts. This can cause various challenges with gate assignments if left unchecked. The first challenge is missed gate assignments that could occur with an adjusting carrier peak. The missed gating comes from a changing ϕ_{CD} that could potentially have a gate transition occur at an instance of the carrier that doesn't exist for this cycle. The second is deformed square waves due to the adjusting carrier cutting into the positive or negative portion of the voltage, if the frequency the PLL is regulating to is much slower or faster than the secondary, respectively. Both of these conditions can be seen in Fig. 2.6. In this figure, the adjustment to faster and lower frequencies by changing the amplitude is done through the red lines. Both of these challenges can be overcome through dynamically changing the relative modulation values with respect to the previous cycle peaks and maintaining safety bounds on the rectifier's duty cycle. However, this causes many challenges with respect to the power controller's output and appropriately scaling its output to adjust to an initially undefined carrier. The upside is that this problem is bounded due to the bounds implemented by the SAE and an effective solution could be created.

The third method, is an extension of the second method's principle of adjusting the carrier. This method directly adjusts the carrier by adding effective delays or increases to the counter, this modulation could be applied directly to the carrier without adjusting its amplitude by adding or subtracting from the carrier to add phase lead or lag and then re-modulate the carrier at a predefined amplitude to maintain the same modulation values for power control. This method would allow for the modulation values to not have to dynamically adjust in response to changes in frequency. This also give the synchronization controller the relative freedom to apply these adjustments along the carrier away from gate transitions. The second method and this method are compliments of each other. In that the second method adjusts the gate assignments to work with frequency while this method

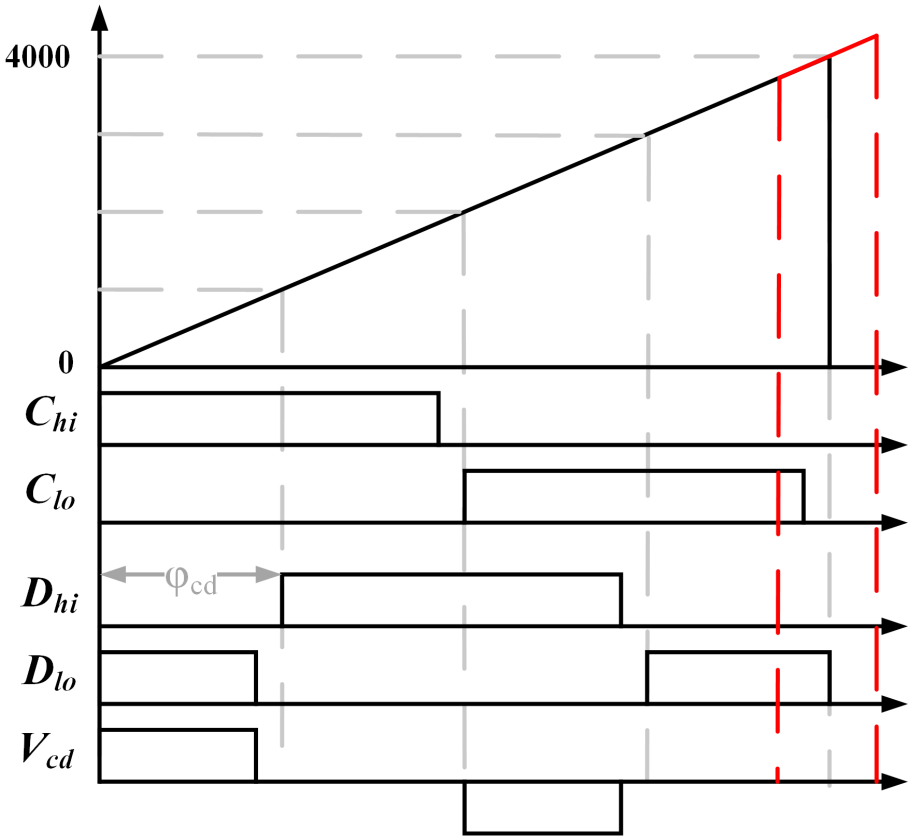

Fig. 2.6: Adjusting carrier through normal PLL

adjusts the frequency to work with gate assignments, and both with correct implementations would work effectively. This later method is the one explored within this thesis.

To express the adjustment of the carrier with the control approach and how a controller could effectively regulate phase and frequency with a PLL, an example is discussed. In Fig. 2.7 there are three saw tooth waveforms. The carrier in black represents the secondaries internal carrier with no adjustments made as a reference. The line in red represents the desired phase and frequency of the secondary carrier to synchronize and maximize received power transfer from the primary. The line in blue represents an adjusted secondary carrier that describes the method of control presented by this thesis, as the controller is separated into two parts. The desired carrier in red has an initial phase offset ϕ_o and a slightly slower operating frequency from the secondary's carrier, which can be noted in the figure by the initial offset and difference in slope.

To determine the phase offset between the secondary's carrier and the desired carrier, a method to determine the starting point of the desired waveform is necessary. To accomplish this, the controller would evaluate the current angle of the secondary's unadjusted carrier at the point in which, the desired carrier is equal to zero. This gives the controller the current phase error every cycle. As shown in Fig. 2.7 where in the first cycle the phase angle ϕ_o is shown when the desired carrier is equal to zero. A method to determine when the zero crossing of the desired carrier occurs is described later in this chapter.

From the determined error, a perfect proportional controller could adjust the secondary's carrier by the error as shown at point E1 in Fig. 2.7, regulating the controller's error to zero. However, it can then be noted that by the next zero crossing event, there is an additional error in the phase represented by ϕ_f. This additional error is described by (2.23), where τ_{AB} and τ_{CD} are the periods of the primary or desired period and the secondaries period, respectively. This error would be again adjusted for by a proportional controller by subtracting it from the carrier, as shown at point E2. The adjustments made in this method would effectively work if it was only a phase offset, this is because the total error is a non-changing value. This aspect of a PLL controller would be the phase detection

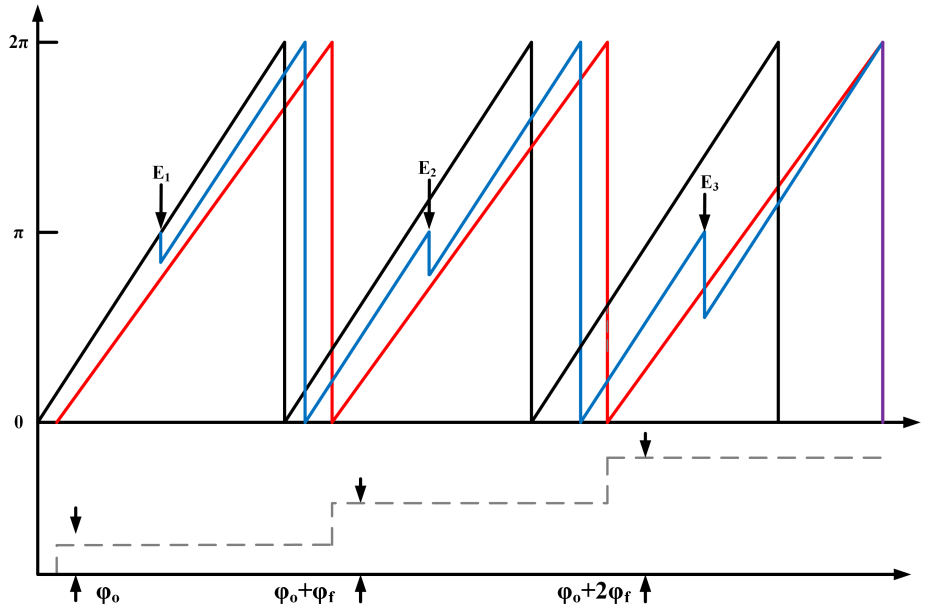

Fig. 2.7: The Black line is the internal unadjusted carrier for the secondary, the Red line is the rectifier's bridge current I_{CD} generated by the primary Inverter, the Blue line represents the adjusted carrier for the secondary. The phase error between secondary and desired is represented by the dashed gray line.

stage.

$$\phi_f = 2\pi \frac{\tau_{AB} - \tau_{CD}}{\tau_{CD}} \tag{2.23}$$

The error in this example, however, is a linear in nature, which means that it cannot be effectively regulated by a traditional reactive controller, which includes proportional, integral, derivative or any combination of the three in parallel. This is because ϕ_f is added every cycle, which, is caused by the frequency difference between controllers. The expected error seen by the synchronization controller can then be described as 2.24, where ϕ_o is the initial phase offset, ϕ_f is the linear slope of the frequency difference, x is the number of cycles of the secondary controller since start, and ϕ_e is the total error seen by the synchronization controller. This function is bounded within the range of $\pm\pi$.

$$\phi_e = \phi_f x + \phi_o \tag{2.24}$$

Therefore, another portion of the controller has to be introduced to regulate the linear error. The controller would have to proactively add the expected change in error of ϕ_f every cycle. This approach can be seen at point E3, which subtracts the current sensed error and the expected change in error on the next cycle to the carrier. The adjusted carrier then has a zero error at the start of the next switching cycle and would maintain zero error so long as ϕ_f was subtracted every cycle.

The method to realize this is by introducing a rollover integral term on top of a PI controller. The (PI)I controller structure can be seen in Fig. 2.8. The structure of the controller has then taken the format of a phase locked loop (PLL) with its input and output modifications specific to this application. This structure maintains a phase detection stage with the PI block, which also acts as the frequency filter. The integral term is then the frequency generation of the PLL. The application specific portion of this controller is that instead of regulating to the primaries operating frequency, it is regulating to the phase and frequency difference between the primary and secondary. This use of a phase locked loop in this context from a signal processing point of view is carrier synchronization or carrier recovery [118–120].

The second to last challenge with the implementation of this controller design is the determination of ϕ_o or θ and ϕ_f. To determine these values, it can be noted that the induced bridge current in (2.25) is independent of the output voltage at its fundamental component and is dependent on the primary side output voltage. The current also contains the desired phase offset θ to maximize power transfer. This equation is only true under the

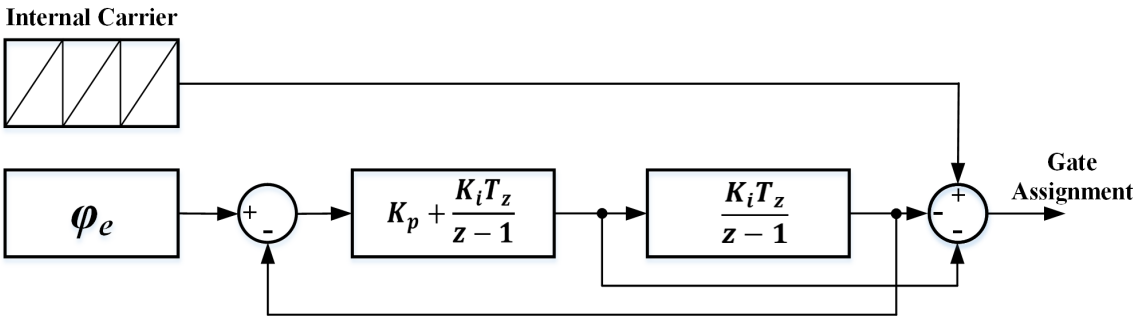

Fig. 2.8: PLL Controller

assumption that the frequency difference is zero. The current I_{CD} is then an ideal source to determine the phase and frequency relationship between primary and secondary. First, to transform the current waveform to a usable digital value, a sensing circuit and zero crossing comparator can be introduced to determine the positive edge current transitions or the zero degree points of the desired carrier waveform in the example above. This information can then be fed into the PLL controller discussed, adjusting the secondaries internal carrier. This leaves us with the final PLL controller representation shown in Fig. 2.9. Where the current I_{cd} is used as the desired carrier. The current is then filtered to remove any higher order harmonics. Then passed to a comparator to find the rising edges of the current, which can then be used to evaluate the current phase angle error ϕ_e that can be then fed to the PLL controller.

To properly determine the phase and frequency, before switching commences to ensure proper synchronization, the use of free resonance currents induced in I_{CD} can be utilized if the lower rectifier switches are kept on as outlined in [104]. This free resonance current can then synchronize the controller and once a certain amplitude of current is reached, to ensure proper regulation, power transfer can begin. This delay for preparing the PLL controller before activation is a requisite in use and doubles in this application as a pad detection stage [118–120].

$$I_{cd} = -\frac{4MV_{in}\sin\left(\frac{\phi_{AB}}{2}\right)}{\pi\omega_s L_{ss} L_p}\sin\left(\omega_s t + \theta + \frac{\phi_{AB}}{2}\right) \tag{2.25}$$

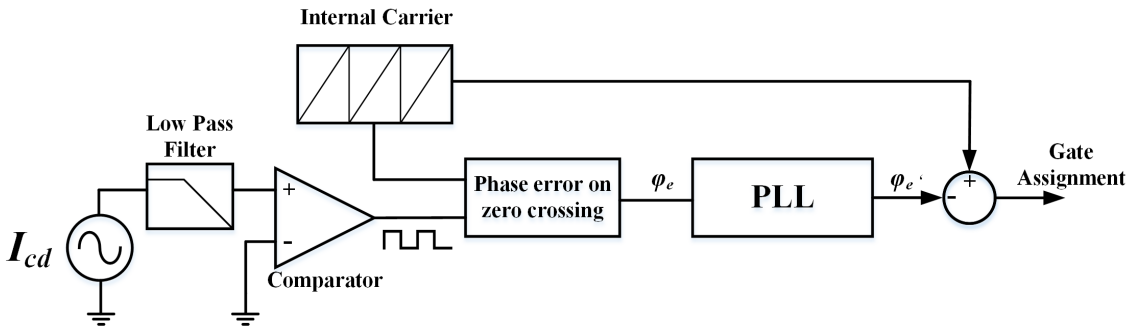

Fig. 2.9: Complete Synchronization Controller

The proposed control behavior is shown in Fig. 2.10. This controller behavior outlines the initial behavior to determine proper sensing and control through free resonance currents, activation of the switches and power transfer, and it determines a cutoff point where power transfer is too low to properly regulate the switching waveforms, due to low amplitude being fed into the comparator.

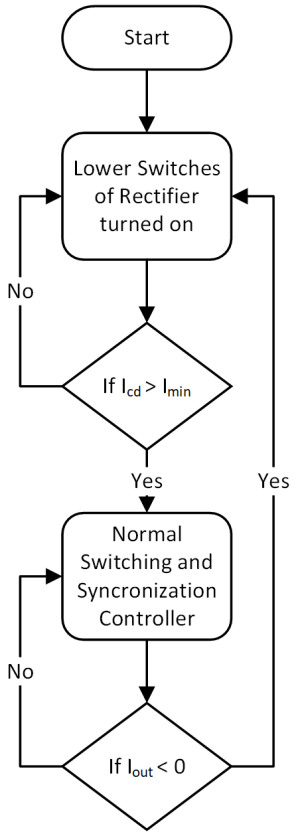

Fig. 2.10: Controller Behavior Flowchart

The final challenges with implementation, is that the adjustments made by the synchronization controller have to avoid switching transitions and maintain proper shape of the induced square wave. This occurs in the final summation block of the controller diagram in Fig. 2.9. To maintain proper adjustment between the positive half of the square and the negative half, a simple division of the necessary adjustment by two can be made and applied at two different points in time along the carrier to maintain proper alignment, one during

the positive half and one during the negative half. To avoid switching transitions with the two points of adjustment, a simple check of the desired ϕ_{CD} can be used to determine the two largest spacing's between switching transitions and apply the two adjustments there. An exaggerated example of this process at two different duty cycles is shown in Fig. 2.11, the desired carrier is shown in blue and the actual secondary carrier is shown in red. It can be seen that as the duty cycle transitions, the locations at which adjustments are made, are moved. The movement of the adjustment points occur around $\phi_{CD} = \pi/4$

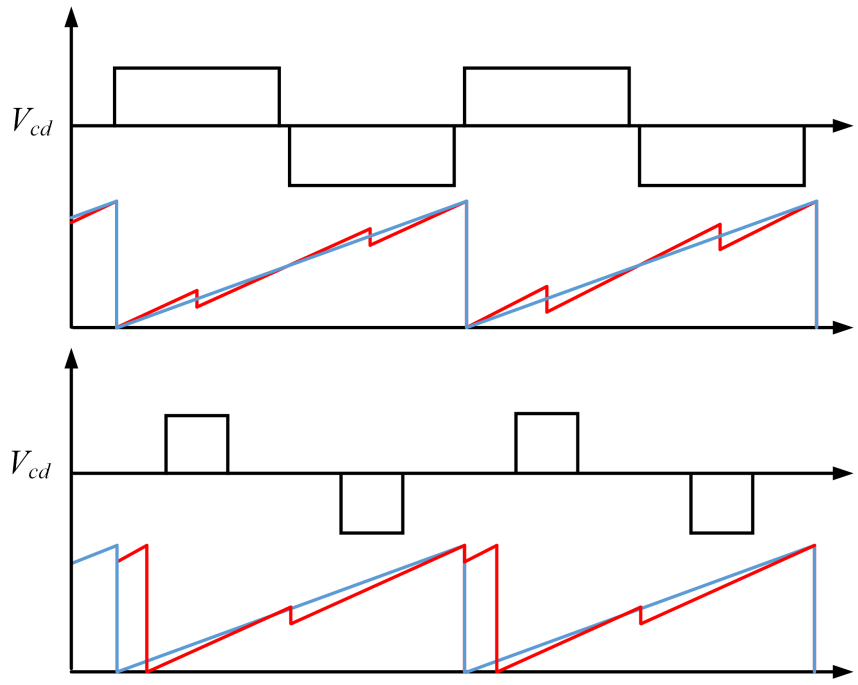

Fig. 2.11: Carrier with split adjustments and variable adjustment points

What this specific implementation accomplishes is a minimization of computational complexity of the PLL stage through locking the PLL to the frequency and phase difference instead of having the controller generate its own unique carrier, which would require instantaneous phase calculations through sin and arctan and higher precision sampling of the current waveform to determine the input sinusoidal. Finally, this controller helps to eliminate concerns about gate assignment and adjustment to account for frequency differences over the range of the SAE standard.

CHAPTER 3

Simulation

3.1 Software

To initially verify the validity of the proposed controller strategy and the DWPT system, a dynamic, and static simulation model was created. The software utilized to determine the controller's performance was PLECS, which is short for Piece-wise Linear Electrical Circuit Simulation. PLECS is a simulation tool designed for switching based electronic circuits. The simulation software utilizes ideal switching devices and does not include parasitics within the simulation, allowing the simulation software to run significantly faster than other circuit simulation software's such as LTspice. The software allows for the designer to build in parasitics if necessary for accuracy.

The primary motivation for utilizing PLECS to validate controller design is the software's integration with MATLAB Simulink through PLECS block set and its internal control blocks. The internal control blocks allow for direct continuous or discrete time controller designs to be implemented directly in the model. Data can also be directly in-jested by Matlab for further analysis or higher level control schemes to be developed with the large library for Simulink.

The other simulation software that was utilized was LTspice to determine the system tuning performance. LTspice is a free general circuit solver. The simulation is an excellent software to solve circuits where parasitics and precision are of an emphasis. The software does struggle with switching circuits due to this precision, though. That is why this software was utilized to validate system tuning and provide power electronics debugging with an accurate static model, A dynamic circuit model is viable but would be extremely cumbersome to include additional control behavior.

Ansys is a magnetic simulation tool utilizing finite element modeling. This simulation

tool is excellent to predict coupling and pad characteristics in wireless charging applications. It can be used as a method to generate an expected DWPT model that can be used in conjunction with PLECS or LTspice to simulate tuning, pad, and control design with a quick turnaround.

3.1.1 LTspice Model

The system design outlined in chapter 2 was applied for the initial static system simulation. The design of the active rectification was done in conjugation with the design of a passively rectified high power DWPT system intended for heavy-duty vehicle applications. Therefore, tuning of the DWPT system was done to satisfy the high power requirement. The parameters of this system are defined by $V_{in} = V_{out} = 800V$, $P_{out} = 100\,\text{kW}$. The primary and secondary pad design will be discussed in chapter 4. The pads inductances are defined in 3.1. The voltage rating for the primary and secondary pad is 2 kV. The primary current rating is 250 A and the secondary current rating is 375 A. The coupling between primary and secondary is $K = 0.197$. From these conditions, the system tuning for the simulation is given in table 3.1. The simulation circuit for the static verification is shown in Fig. 3.1.

Table 3.1: System Tuning Values

Component	Value
L_{ps}	5.62 µH
C_{pp}	0.624 µF
C_{ps}	0.453 µF
L_p	13.36 µH
L_s	7.26 µH
C_{ss}	0.898 µF
C_{sp}	1.04 µF
L_{ss}	3.35 µH

This circuit's inverter and output power waveforms are presented in Fig. 3.2 and Fig.

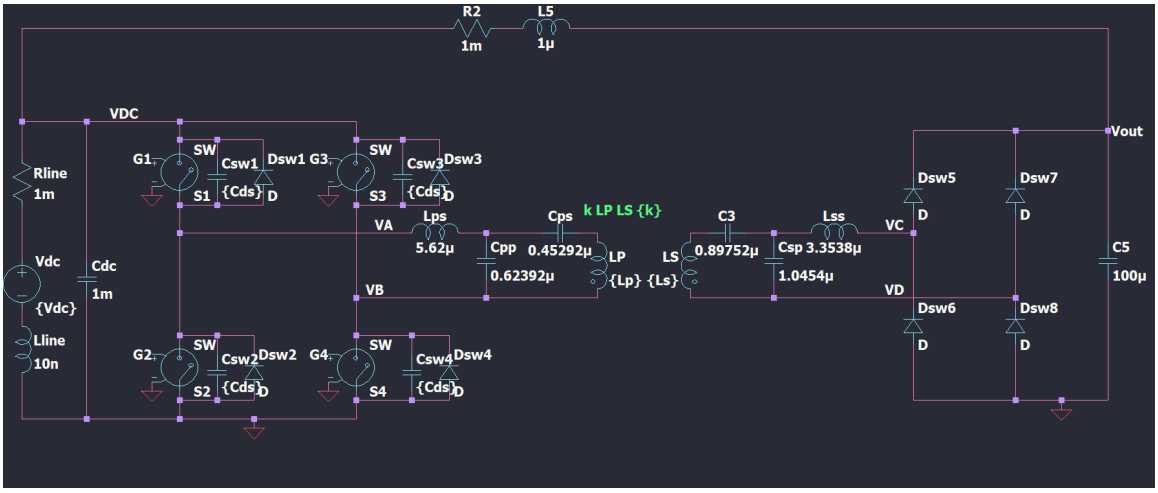

Fig. 3.1: Static LTspice Simulation

3.3. For the simulation and hardware validation of the system, the testing makes use of recirculating DC current from the receiver back to the primaries to allow for the system power supply to only supply losses. From these waveforms it can be seen that given these tuning values generated from the analytical solution, and the system design parameters, the circuit does not effectively soft switch and the power output is slightly below the desired output power at 88 kW.

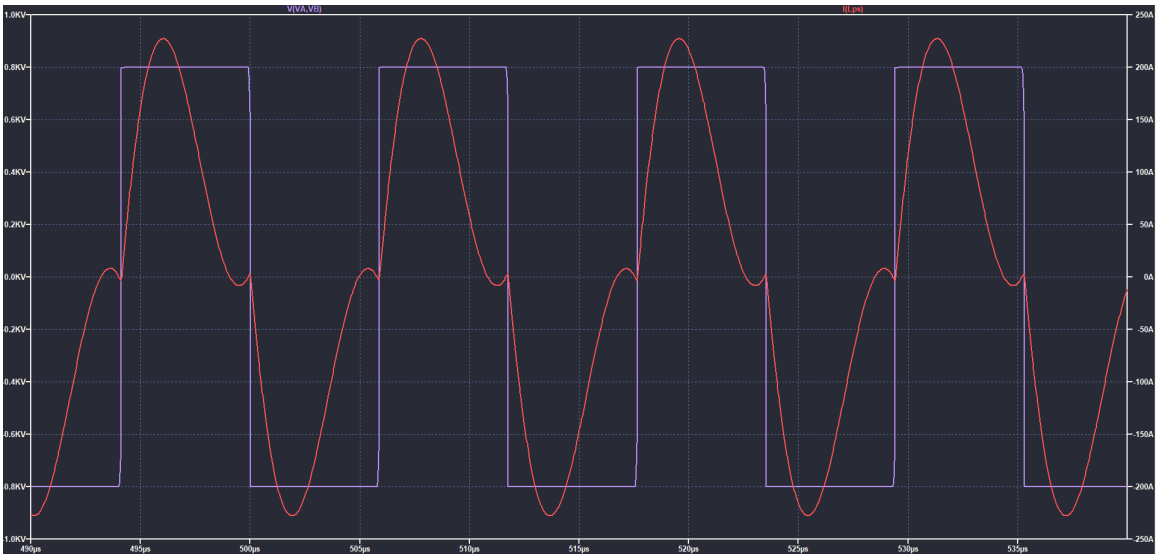

Fig. 3.2: LTspice Inverter Wave Forms

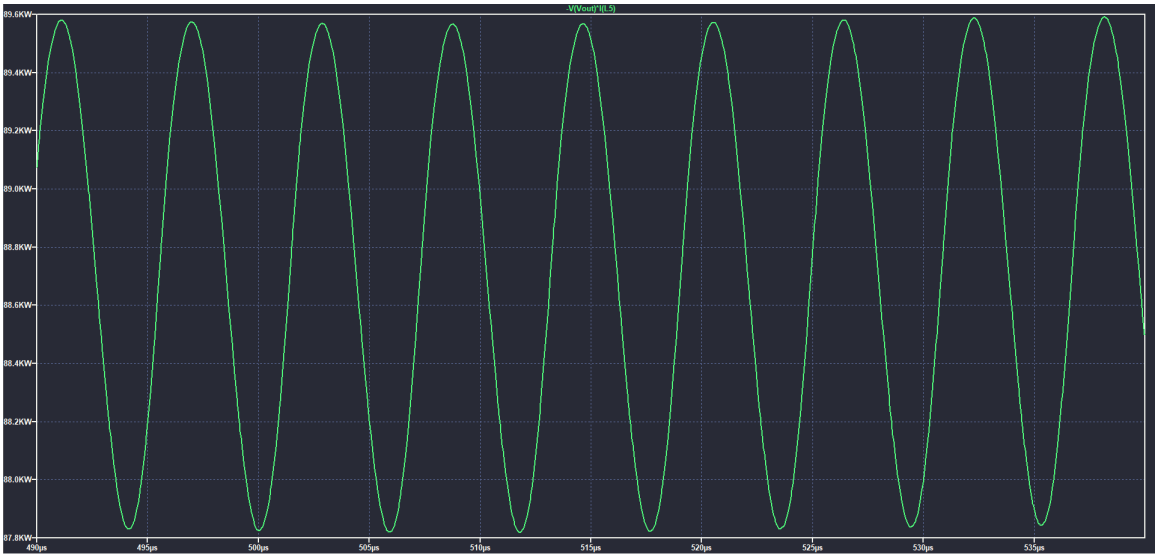

Fig. 3.3: Output Power

The lower output power is attributed to the output current I_{cd} shown in Fig. 3.4. It can be seen from the figure that current I_{cd} is operating in discontinuous conduction mode. The source of this phenomena is outlined by [121]. The proposed cause of the discontinuous conduction in this paper is the ratio of the receiver coils voltage and the output DC voltage. The ratio of these voltages needs to be such that the receiver coils voltage is not significantly smaller than the output voltage. Adjustments to tuning can be applied to adjust this ratio such that DCM is avoided, and were then applied through trial and error with the physical tuning values in the experimental setup.

However, under hardware testing, it was also noted that the system was producing large amounts of noise within the communication wires. The source of this noise was determined to be high $\frac{dv}{dt}$ across the pads relative to ground. The waveforms of the pad's voltage with a traditional LCCL-LCCL tuning can be seen in Fig. 3.5. The generation of this noise is caused from missed matched impedance's seen by either half bridge of the converter. To address the noise, the design of the LCCL-LCCL tuning network moved to a split compensation design, by splitting the series inductors and capacitors.

The design of the split tuning circuit follows the same as described previously with the added change of the series inductors L_{ps} and L_{ss} are split into two, their values halved,

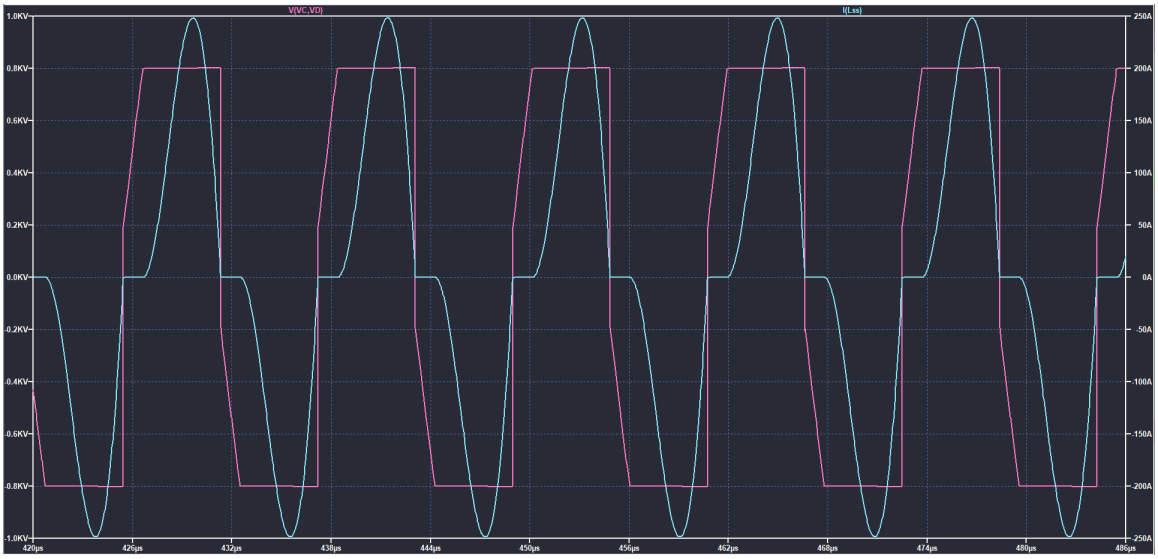

Fig. 3.4: LTspice Rectifier Wave Forms

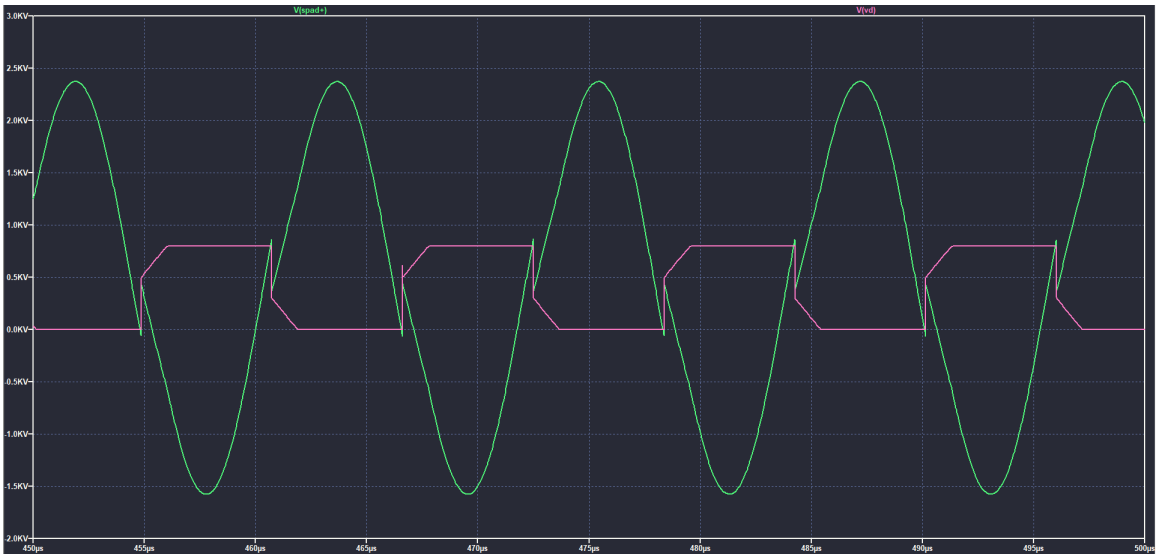

Fig. 3.5: Pad Voltages Relative to Ground with Traditional LCCL tuning

and applied to either leg of the half bridge. The series capacitance C_{ps} and C_{ss} are split into two, their values doubled, and applied to either side of the coils. The final tuning topology layout is shown in Fig. 3.7. The circuit was then simulated with the split design and the pad voltages relative to ground were now pure sinusoidals as shown in Fig. 3.6. This drastically decreased the system's noise output.

The analytical tuned values and realized hardware tuned values, including modifications

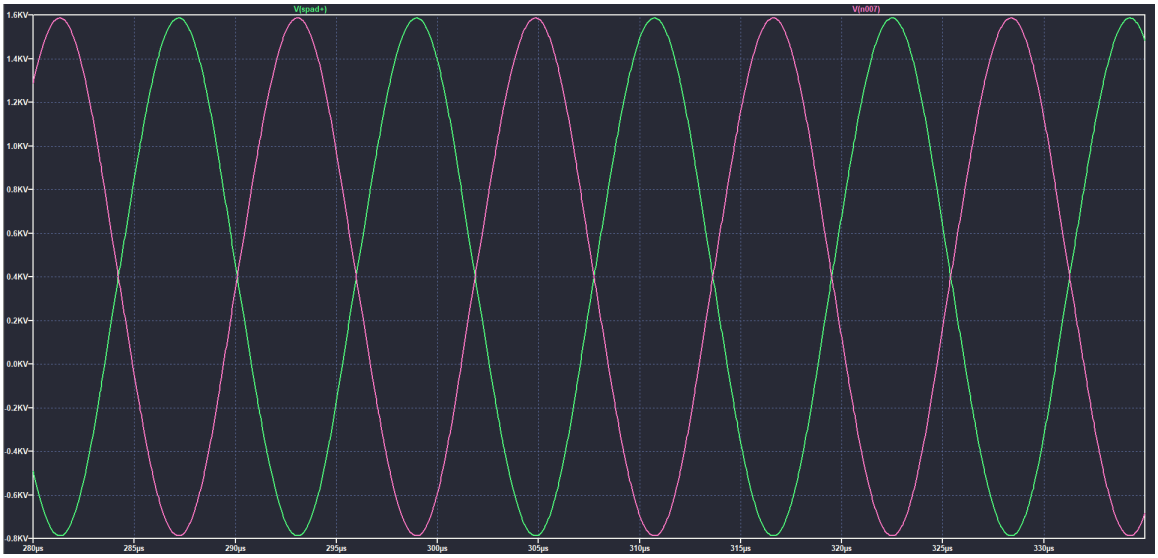

Fig. 3.6: Pad Voltages Relative to Ground with Split Tuning

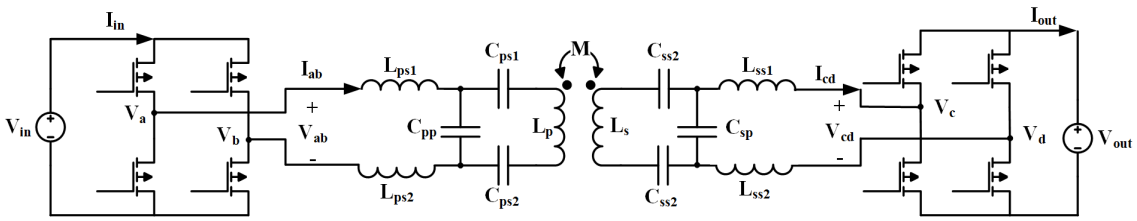

Fig. 3.7: Split Tuning Topology

to avoid DCM, are presented in table 3.2. The final hardware tuning values were simulated using LTspice and achieved a power output of 97 kW. With the modified tuning values, the new tuning achieves zero volt switching which can be seen in the inverters output waveform shown in Fig. 3.8, in which the bridge current is lagging the induced square wave voltage.

Table 3.2: Analytical and Realized Tuning Values for Split Tuning

Component	Analytical Value	Hardware Value
L_{ps1}&L_{ps2}	2.81 µH	2.81 µH
C_{pp}	0.624 µF	0.6308 µF
C_{ps1}&C_{ps2}	0.906 µF	0.830 µF
L_p	13.36 µH	13.36 µH
L_s	7.26 µH	7.26 µH
C_{ss1}&C_{ss2}	1.795 µF	1.980 µF
C_{sp}	1.04 µF	1.045 µF
L_{ss1}&L_{ss2}	1.677 µH	1.677 µH

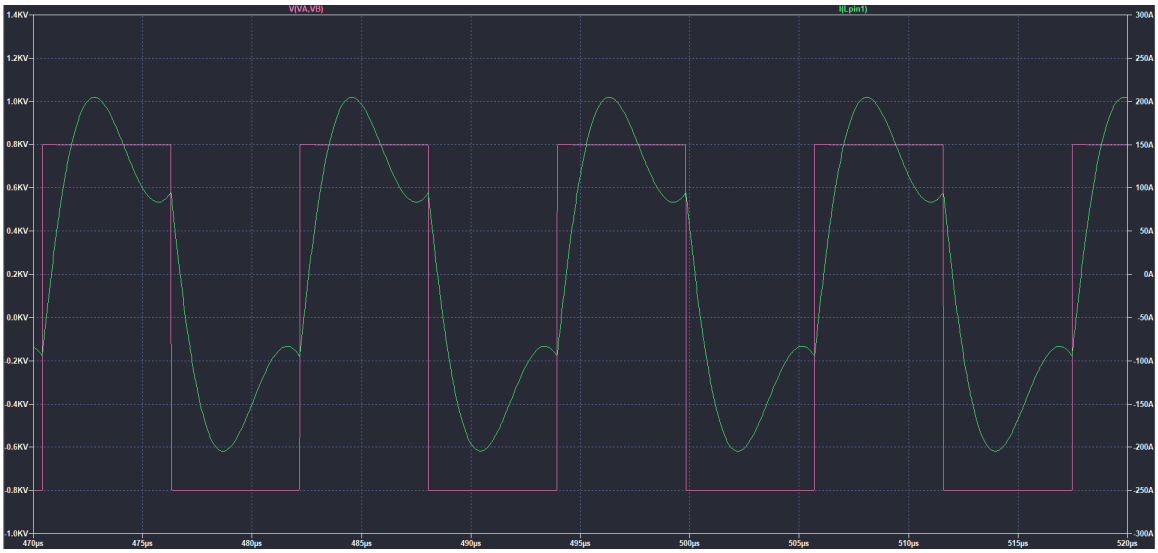

Fig. 3.8: Hardware Realized Simulation

3.1.2 PLECS Model

The dynamic circuit model utilized in PLECS has its origin in design from [104, 115]. In these research papers, the initial proposal of PLECS to model dynamic wireless power transfer was proposed [104], and then further refined in [115]. This was proposed to achieve a quick turnaround for updating pad and magnetic information, tuning design and closed loop controllers. The general outline of this approach is described here, along with controller implementation. The controller was implemented in PLECS to be directly realizable within hardware.

To develop a dynamic simulation model for wireless power transfer, a coupling coefficient and inductance matrix needs to be defined in order to determine the respective coupling between primary pads and the secondary. The mathematical representation of this position varying inductance matrix was described in chapter 1. To generate the matrix, Ansys was utilized. The Finite element solver can generate an accurate position based inductance matrix that then can be fed into the simulation software.

The design of the pads within Ansys utilizes a DD primary and secondary coil structure which, can be seen in Fig. 3.9. From this figure, it can be seen the structure of the DWPT system will consist of three primary pads and a single secondary receiver. The coupling of the pads through lateral misalignment are given in Fig. 3.10. From this it can be seen that the primary pads one, two, and three have good coupling to the secondary pad four, while it is traveling over. the primary pads also have relatively low coupling between them.

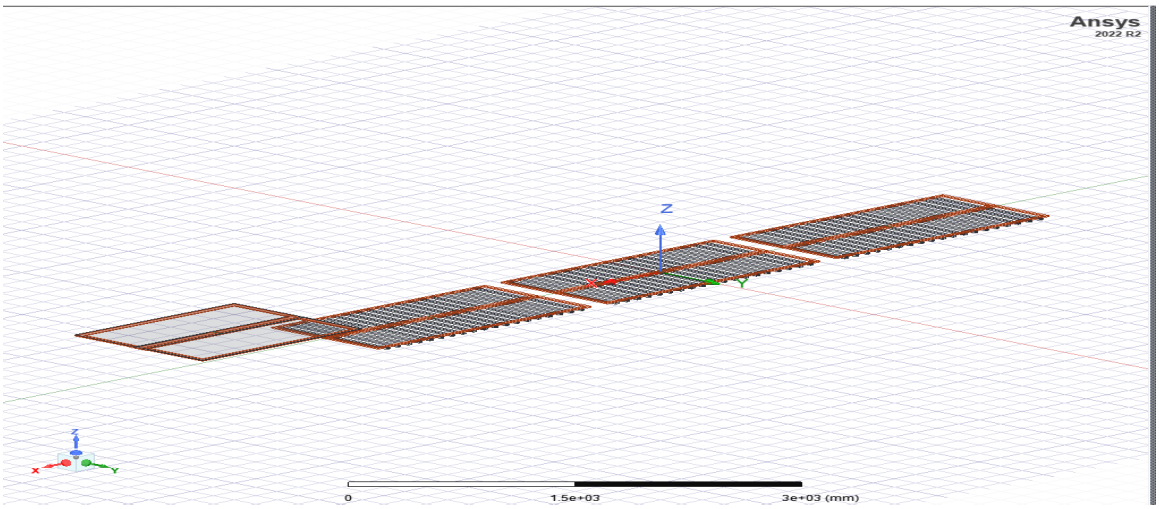

Fig. 3.9: Ansys Simulation Model

This inductance matrix can then be fed directly into the PLECS model. The PLECS model can implement this inductance matrix through a variable inductor circuit element. The model takes the dynamic inductance matrix as a control variable for this inductor. The PLECS variable inductor requires this inductance matrix to be structured by row for the various elements, followed by their time derivatives. The coupling matrix described

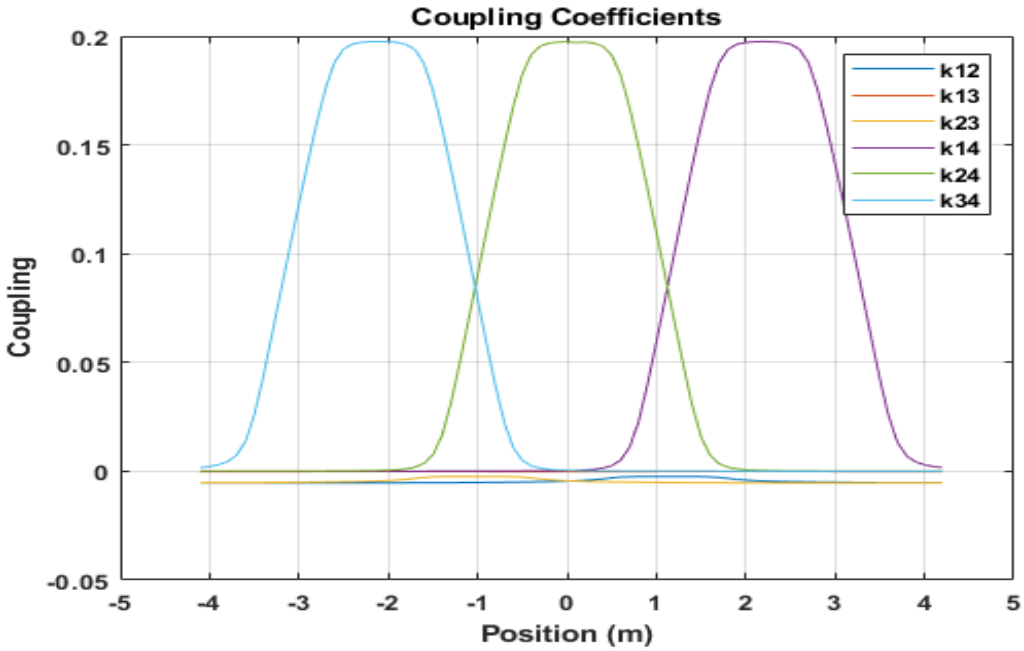

Fig. 3.10: Position Varying Coupling Coefficients

previously can be directly transformed to follow this pattern. The terminals of the variable inductor are then de-multiplexed at either terminal, and the full implementation is shown in Fig. 3.11.

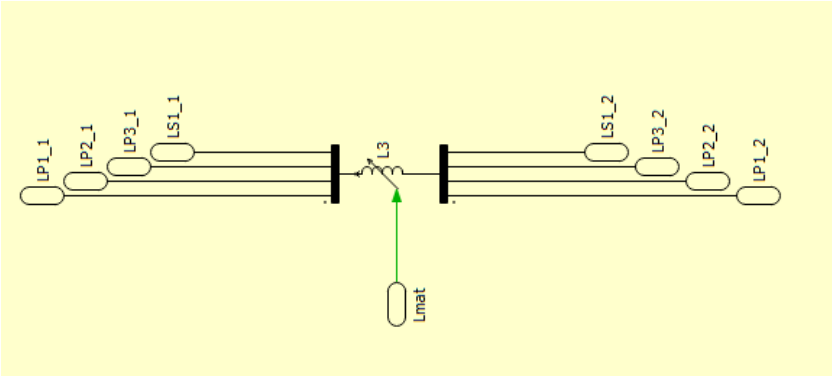

Fig. 3.11: PLECS Variable Inductor

The remaining model from a power electronics view includes the system tuning, inverters, and rectifiers. The Fig. 3.12 shows the overall circuit model including the three primaries, secondary, source, and load. In Fig. 3.13 the primary tuning network and in-

verters are seen including the split tuning topology. In Fig. 3.14 the secondary tuning network and active rectifier are seen, along with the power and synchronization controller sub-blocks.

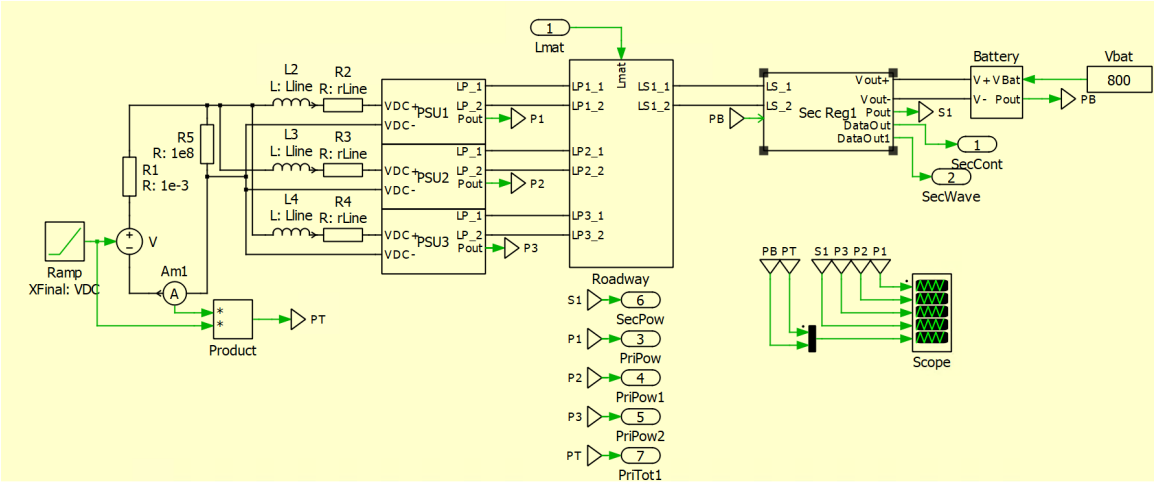

Fig. 3.12: System Level PLECS model

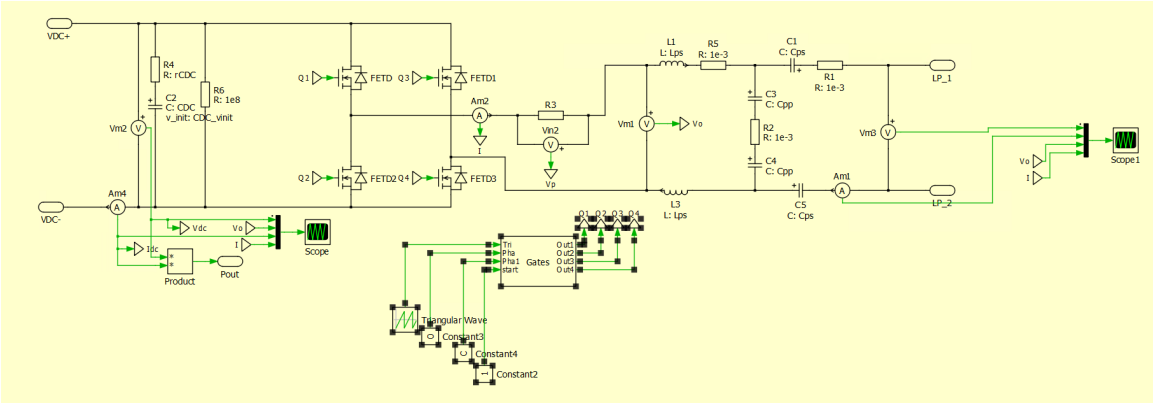

Fig. 3.13: Primary sub-block PLECS model

Within the secondary subsystem in Fig. 3.14 it can be seen there are three subsystem blocks that regulate the switching behavior. The first control block on the bottom right is implementing the gate assignments. Within this block there are straightforward gate assignment outputs from the input control variables from the phase and power control block

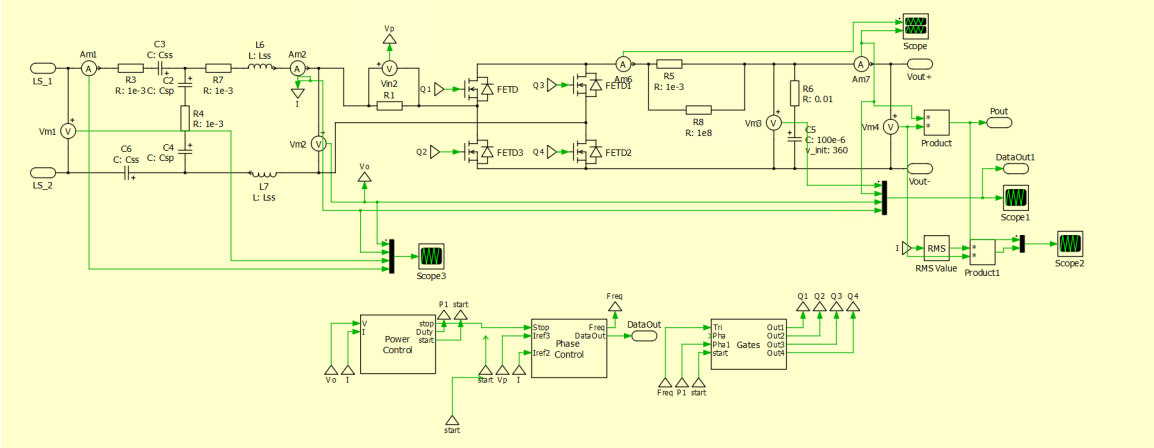

Fig. 3.14: Secondary sub-block PLECS model

and can be seen in Fig. 3.15. The second subsystem is the power controller, which implements power regulation, activation, and deactivation according to the controller flowchart shown in Fig. 2.10. The exact model within the subsystem is shown in Fig. 3.16. From this model, it can be seen the PI controller that is regulating ϕ_{CD}. It is accomplishing this by regulating to different references determined by the bottom C-script output, which is implementing activation and deactivation.

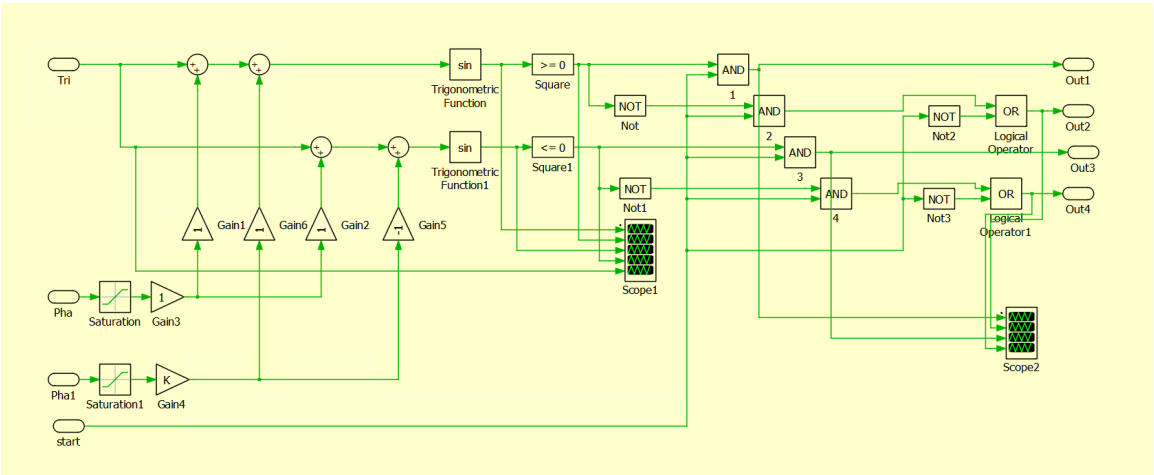

Fig. 3.15: Gate Assignment Control Block

The final control block implemented is the phase and frequency controller, as shown in Fig. 3.17. This control structure implements the digital equivalent PLL controller structure,

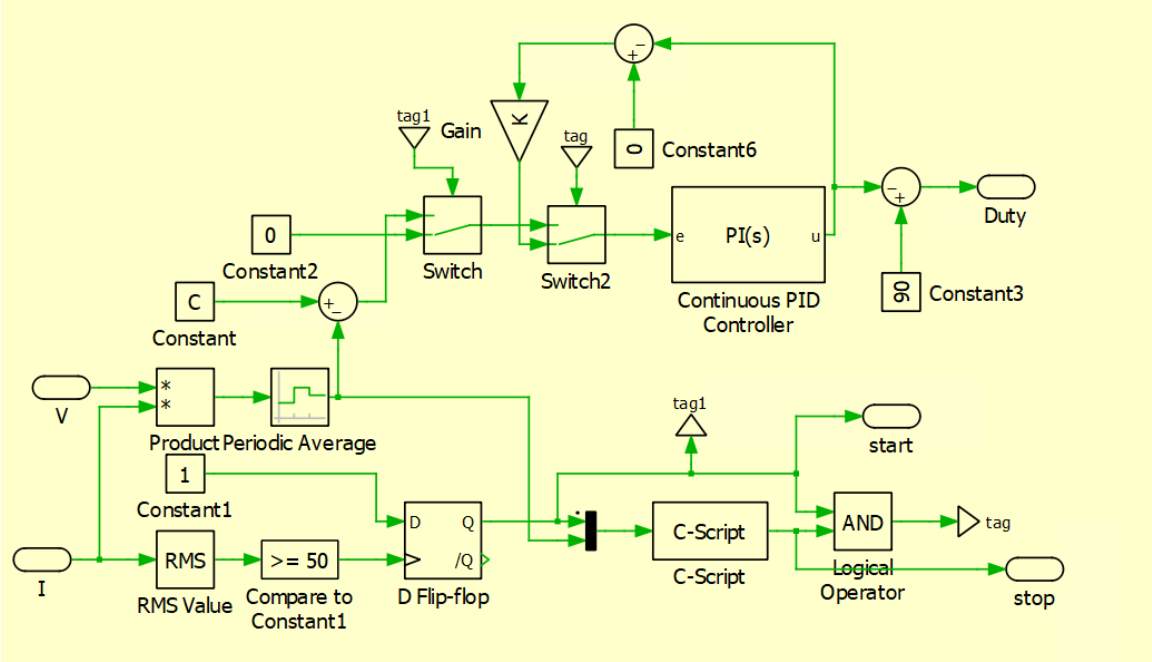

Fig. 3.16: Power Regulation Control Block

with a few additional modifications to allow for direct hardware implementation. The first modification made to the controller structure is a low pass input filter to the system. This Low pass input filter is to filter out higher order harmonics from the current waveform. that would cause undesirable zero crossing events. The undesirable zero crossing events would negatively affect controller behavior. The filter design is a simple low pass filter set to slightly above the resonance of the system, as shown by the bode plot of the filter seen in Fig. 3.18.

From this point, the next two blocks in the PLECS model act as the zero crossing comparator to determine positive edge zero crossing events. The following c-script calculates the effective phase error of the internal carrier and the input. After which it is fed through the feedback of the PLL controller and then to another c-script which bounds the input of the error to $\pm\pi$. This bounding ensures the controller always regulates to the smallest phase error distance. Lastly, there is an additional constant added to the phase shift before modulation to take into account the phase lag introduced by the filter. The discrete PLL controller is then fully realized.

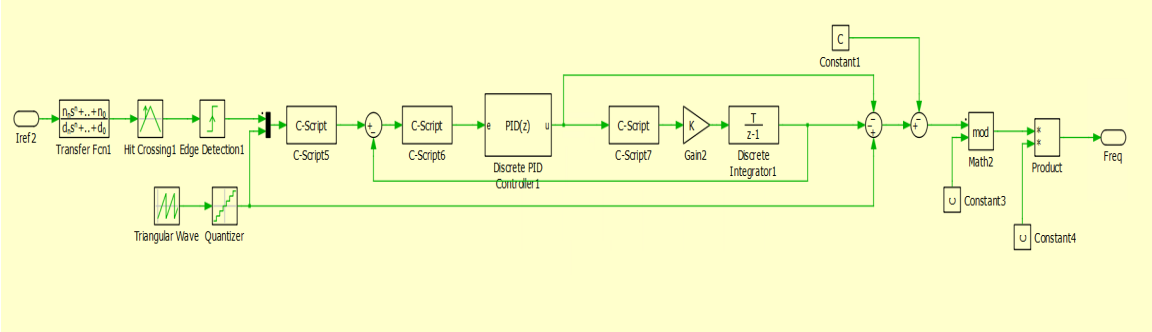

Fig. 3.17: Phase and Frequency Control Block

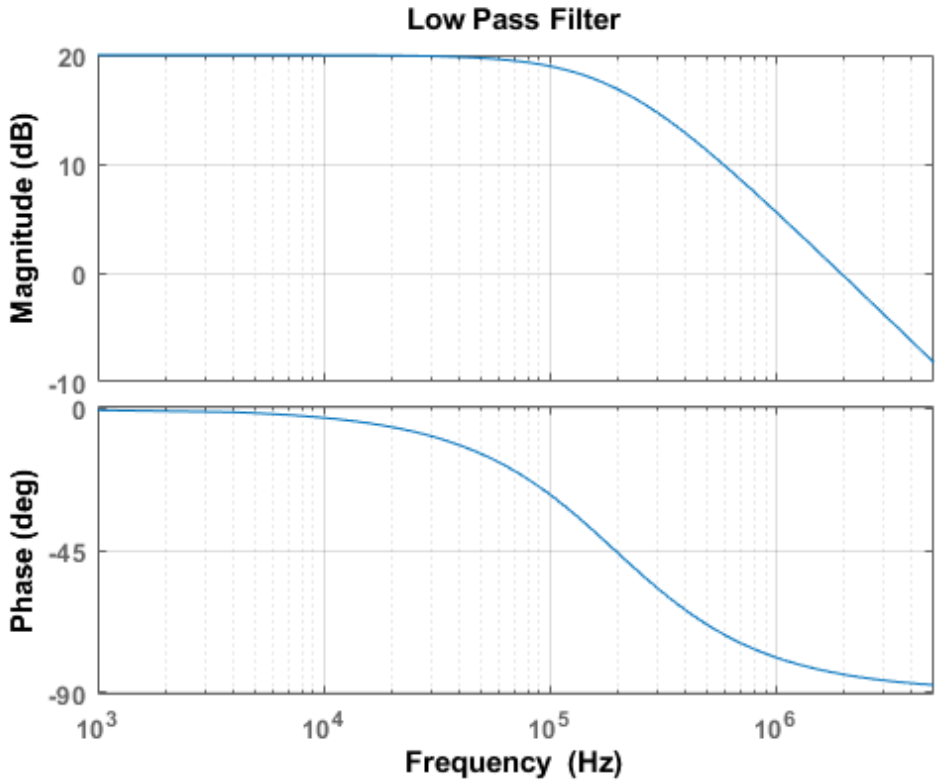

Fig. 3.18: Bode of input filter

The primary controllers for this simulation have been set up without any additional vehicle detection. That entails that all primaries are active for the full duration of the simulation and are properly synchronized to the same operating frequency. For this simulation, the primary and secondary inverters operated with a frequency difference of 50 Hz and an initial phase offset of 30°. The vehicle speed was set to 100 mph (160.93 km/h). The

frequency difference was set to 50 Hz for two reasons. The first is that, due to the precision of the FPGA utilized in the hardware validation stage, 50 Hz is a large enough frequency difference to show meaningful compensation by the controller. The second is that, 50 Hz a frequency difference that allows the simulation to solve for a common base frequency to run the simulation at.

The power output of this simulation can be seen in Fig. 3.19. From this simulation, it can be seen that the total power transfer of the system was slightly higher than the LTspice simulation when the vehicle was directly over one of the primary pads. This is due to the difference in the simulation software. The peak power received by this simulation is approximately 100 kW with a power ripple of 12 kW while transitioning between pads. It can be seen the activation point of the rectifier cut off some initial power transfer of the first pad as well as some power transfer from the final pad during deactivation. The point at which activation and deactivation occur can be improved through better sensing methods and higher precision of control. However, for this vehicle speed and the shown response time, the controller demonstrated has an effective activation and deactivation response time.

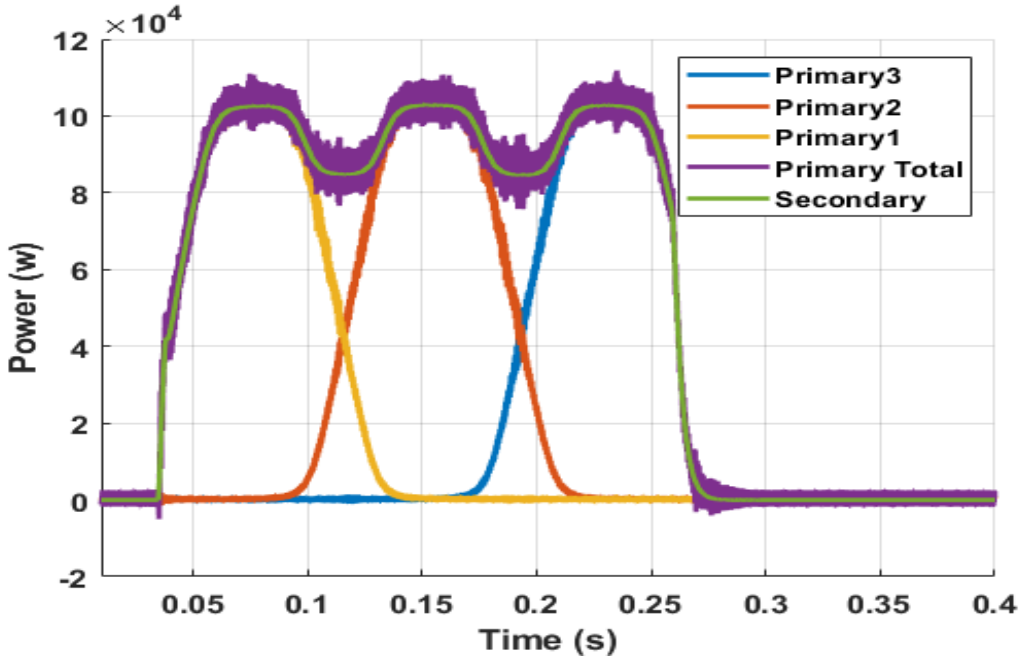

Fig. 3.19: Power Transfer of DWPT system

From the simulation, it can also be viewed the rectifier's voltage and current waveforms shown in Fig. 3.20. The controller's output's can also be seen in Fig. 3.21. The inverter waveform highlights proper direction of power flow and power regulation through ϕ_{CD} and good alignment of the bridge current in purple with the induced bridge voltage in yellow. The controller outputs highlights the secondaries internal carrier τ_{cd} in orange. Its adjusted carrier in yellow $\tau_{cd'}$. The adjusted carrier is synchronized with the induced bridge current or the desired alignment, shown in blue τ_{ab}. It can be seen that the adjusted carrier has synchronized effectively with the desired carrier. The controller's output can be seen by the lines in purple and green. In which the line in purple represents the phase detection stage of the PLL controller and the line in green represents the frequency output of the controller. Given the relative frequency difference between controllers to the operating frequency, both of these values would appear static at this level of zoom.

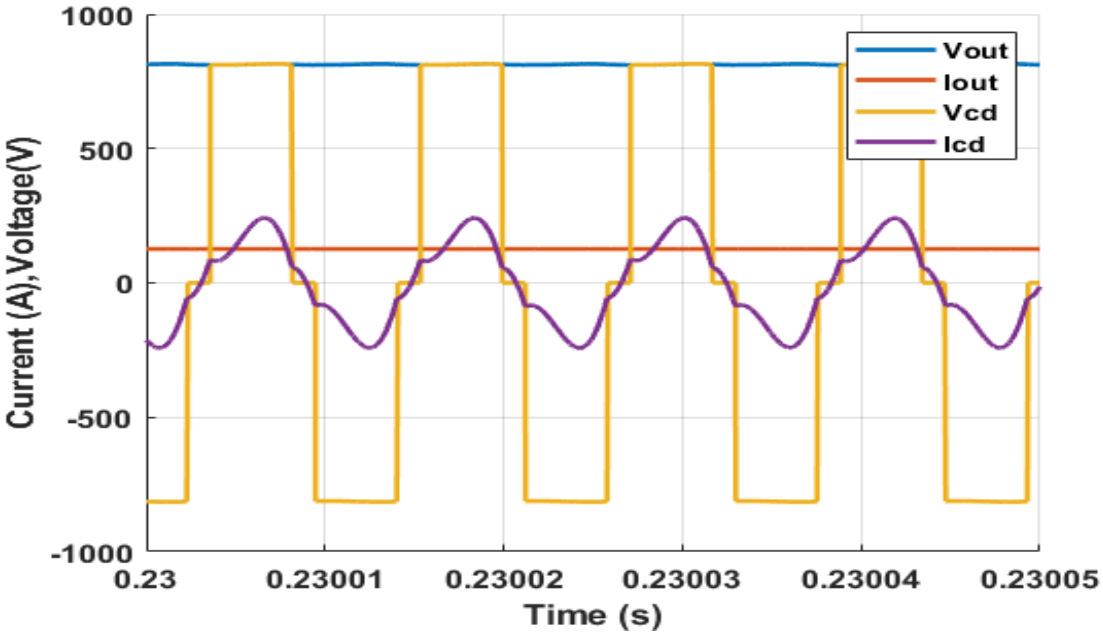

Fig. 3.20: Rectifier Waveforms

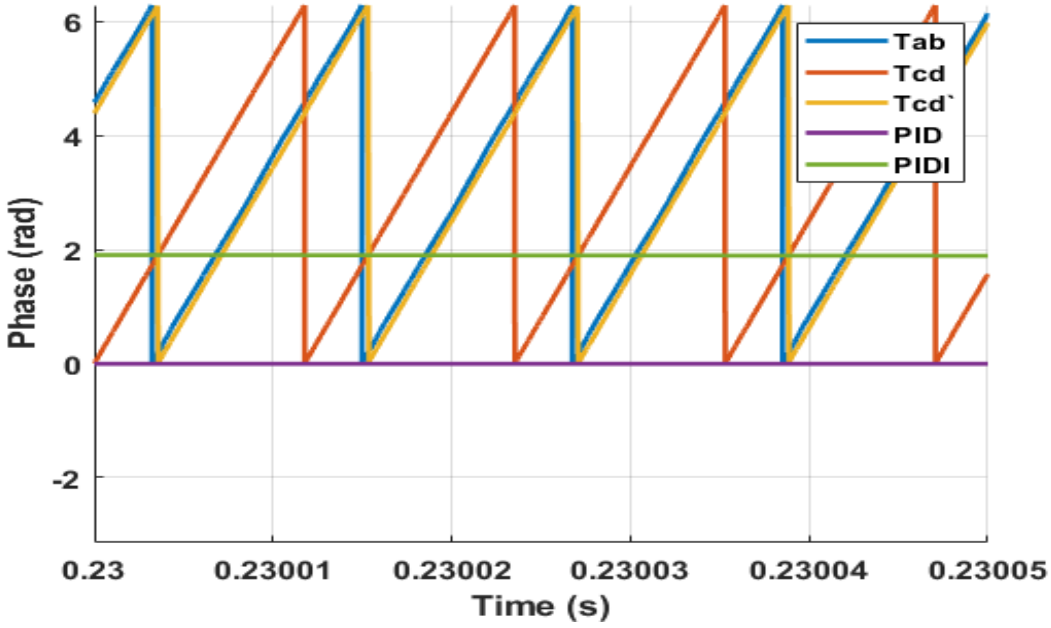

Fig. 3.21: PLL controller Wave Forms

CHAPTER 4

Hardware Testing and Results

4.1 Implementation

4.1.1 Power Electronics

The development of the hardware for this control strategy was done in tandem with a traditional passively rectified 100kW DWPT system. The high level design of that system and more in depth considerations for the hardware design of the controller are outlined in this section. The first consideration for the system was the selection of switching devices. The selection of switching devices was governed by the power specifications. For the 100 kW system, the input, and output voltage for testing was set to 800 V. This voltage and power level then defines the desired DC and AC current of 125 A and 138 A RMS, respectively.

The component options for the switching devices are limited by operating frequency and power levels of the system. The final selection of the switching device was a silicon carbide power module from Wolfspeed. The device has a voltage rating of 1200V, and at the operating frequency of 85kHz, a current rating of approximately 170 Amps RMS. An image of the Wolfspeed device is shown in Fig. 4.1a and its output current rating versus switching curve is shown in Fig. 4.1b. The selection of power modules over discrete devices was to increase power density of the system while minimizing implementation complexity and parasitics.

From the selection of the switching devices, the design of the inverter and active rectifier could be completed. The full assembly and individual PCBs are shown in Fig. 4.2. The design of the inverter assembly was heavily influenced by ease of assembly. The gate drivers that are designed for these switches mount on top of the switching device, the gate drivers have additional connectors on top for power and gate signal inputs. For ease of assembly,

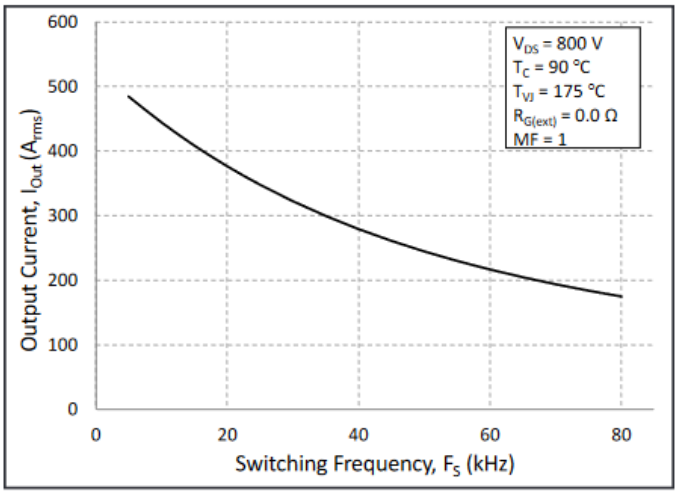

Figure 22. Typical Ouput Current Capablity vs. Switching Frequency (Inverter Application)

(a) Wolfspeed Sic Power Module (b) Output Current Vs. Switching Frequency

Fig. 4.1: Switching Device Selection

and to remove jumper wires from the control PCB to the gate drivers, a layered PCB mounting structure was designed and can be seen fully assembled in Fig. 4.2c.

First, the power board was designed utilizing 6 layer 6 oz (0.23 kg) copper to handle the power levels required as shown in Fig. 4.2a with the mounted gate drivers. From this the choice of DC bus capacitance was also designed to handle the RMS ripple currents of the system which are 110 A RMS. The DC capacitors were broken up into two complimentary sections. The first section is made up of high frequency ceramic capacitors to handle high frequency ripple. This capacitance constituted 1.5 µF of the total capacitance. The remaining capacitance was handled with film capacitors mounted to the PCB with a capacitance of 400 µF to meet voltage and current ripple. Bleeder resistors were also utilized with dual functionality. The resisters were utilized to drain the DC capacitors in case of a fault, as well as operate as a voltage divider to measure DC voltage on the control board.

The gate drivers were mounted through the power board to the switching devices. The control board, as seen in Fig. 4.2b, was mounted directly to the top of the gate drivers. This allows for compact and easy assembly while allowing quick revisions to be applied to the control PCB without having to wait for the power PCB redesign. Additionally, a small

daughter board can be seen attached to the control board. This daughter board allows for even faster deployment of new sensing circuitry or control hardware. On the control and daughter board there are provisions for DC and AC sensing for current and DC voltage sensing. There are also provisions for fiber optic synchronization signals between primary pads and the sensing circuitry necessary for the control strategy of this thesis.

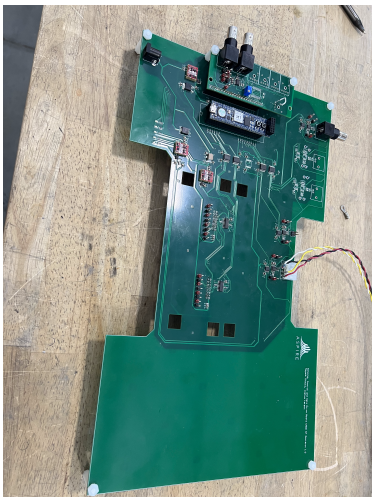

(a) Inverter Control Board

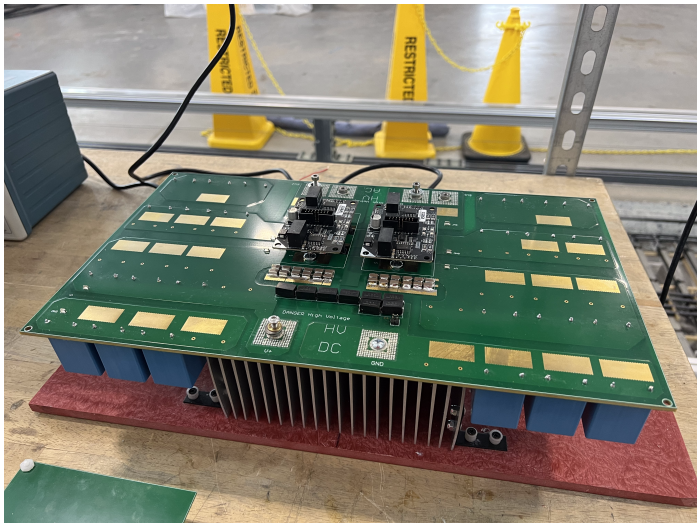

(b) Inverter Power board

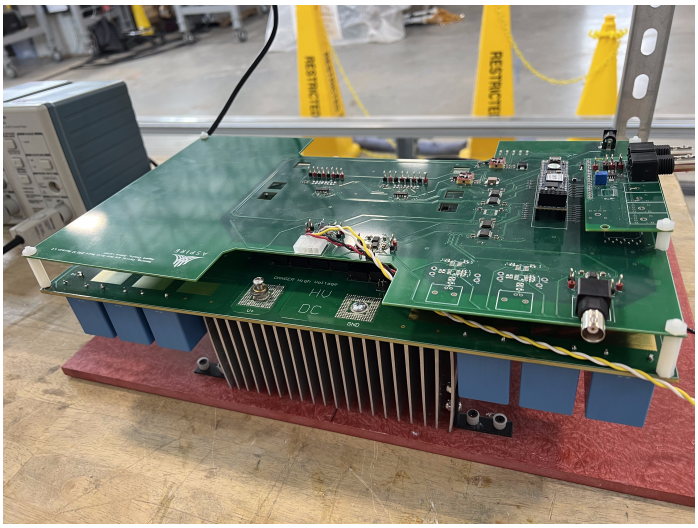

(c) Full Inverter Assembly

Fig. 4.2: Inverter Assembly

4.1.2 Sensing Circuitry

To allow for proper zero crossing detection of the rectifiers bridge current, a sensing circuit had to be designed. From the analytical and simulated design, the hardware realization can be broken into two distinct sections. The first section is the AC sensing circuit and the second is the Low pass filter and comparator to locate the rising current edges. Given the high currents flowing through the bridge of the rectifier and inverter, it was decided to fabricate an in house current transformer to measure the AC current. The circuit of the current transformer is shown in Fig 4.3. This figure highlights the primary winding which will be the sensed wire. The secondary windings are the sensor windings which are wrapped around a toroid. The winding ratio between the primary and a single secondary is 1:30. The current generated from these windings will be fed through burden resistors of 1Ω to handle the few amps of current generated by the transformer and allow for a voltage output. After this, it goes into an output resistor of 100Ω to match the impedance of the sensor to 50Ω BNC connection when the windings are placed in parallel. The final conversion ratio from Amps to Volts is 1200:1 A/V.

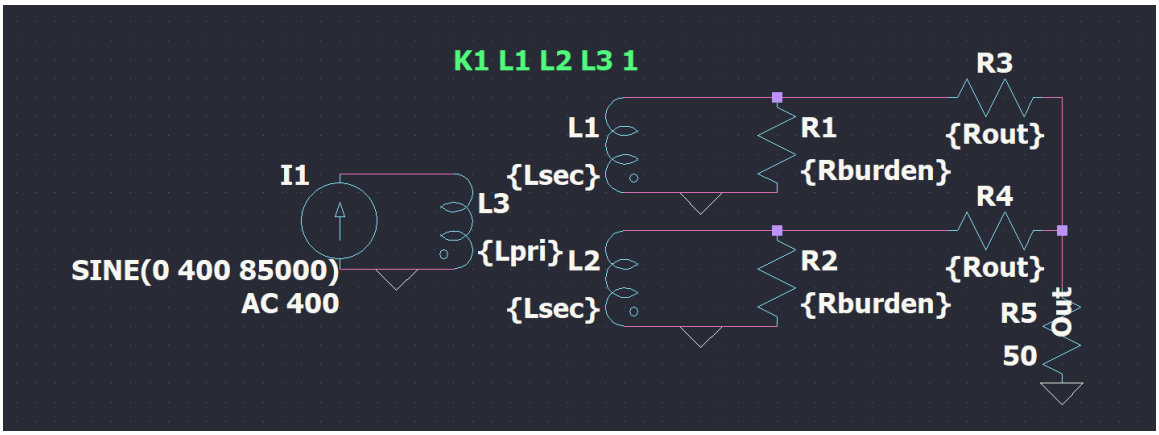

Fig. 4.3: Current Transformer Circuit

The simulated frequency response of this sensor is highlighted in Fig. 4.4 and was confirmed with a network analyzer. From this figure, it can be seen that the CT has effectively a zero degree phase shift in its output voltage relative to the current input at

85kHz. The realized current transformer is shown in Fig. 4.5. In this figure, it can be seen that the toroid with secondary windings has been shielded with copper sheets. The burden and output resistors can also be seen along with the BNC connection.

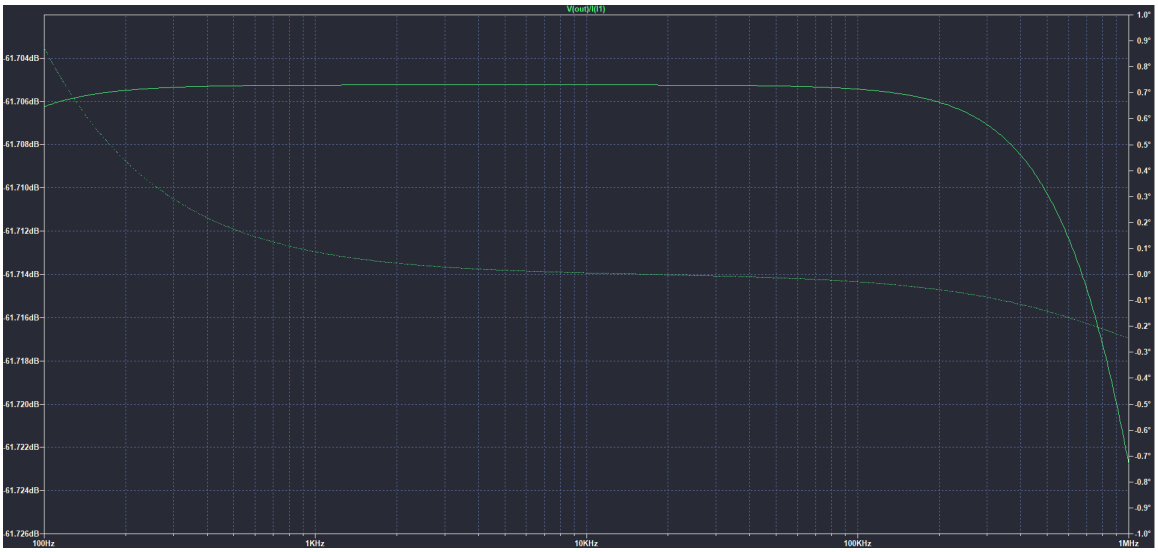

Fig. 4.4: Current Transformer Frequency Response

The output of the CT is then fed to an amplifier and filter stage. This stage adds a gain to the output of the current transformer due to the large conversion ratio and applies the desired low pass filter from simulation. The circuit diagram of the amplifier is shown in Fig. 4.6 The amplifier utilized is a AD8138 and maintains a 10x gain with $1k\Omega$ for R1 and a $10k\Omega$ for R2. The filter capacitance needed for the amplifier is 82 pF The final filter output is shown in Fig. 4.7. From this it can be seen that at the fundamental component of the sensed signal will have a 28° lag. This lag as specified in simulation can be accounted for through a feed forward offset inside the controller. The amplifier's output has a DC offset of 2.5 V and a range of 0 V-5 V. This output is sent to a high speed comparator with its comparison point set to 2.5 V to determine the zero crossings. The high speed comparator is a TLV3601.

The full sensing circuit was then verified to determine minimum currents for accurately determining the zero crossing events and the actual phase lag introduced by the filter. It was

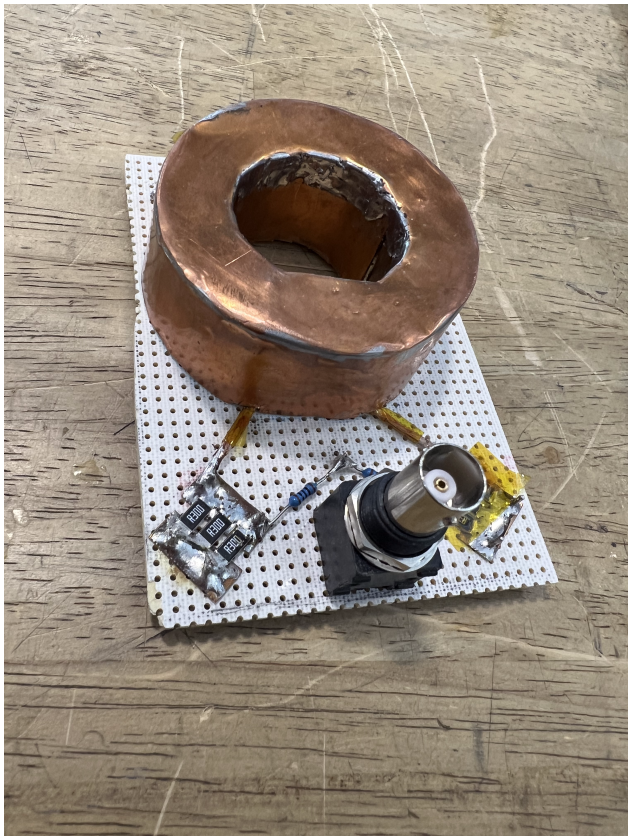

Fig. 4.5: Current Transformer Prototype

completed utilizing a power amplifier to replicate the bridge currents as pure sinusoidals. From these tests, the following data was generated as shown in table 4.1. This data allowed for a determination of a minimum starting point for the controller to accurately detect zero crossings. This allows for an approximate starting point to activate the controller based on the free resonant current amplitude. This starting point is around the 50 A range since a current amplitude of 34 A yields sporadic comparison values but has reached completely stable readings by 68 A. The Fig. 4.8 highlights the output voltage waveform from the current transfer in light blue and the output voltage from the amplifier in dark blue and the generated square wave from the comparator in purple.

4.1.3 Coils and Tuning

The remaining hardware pertains to the actual resonant circuit and wireless power

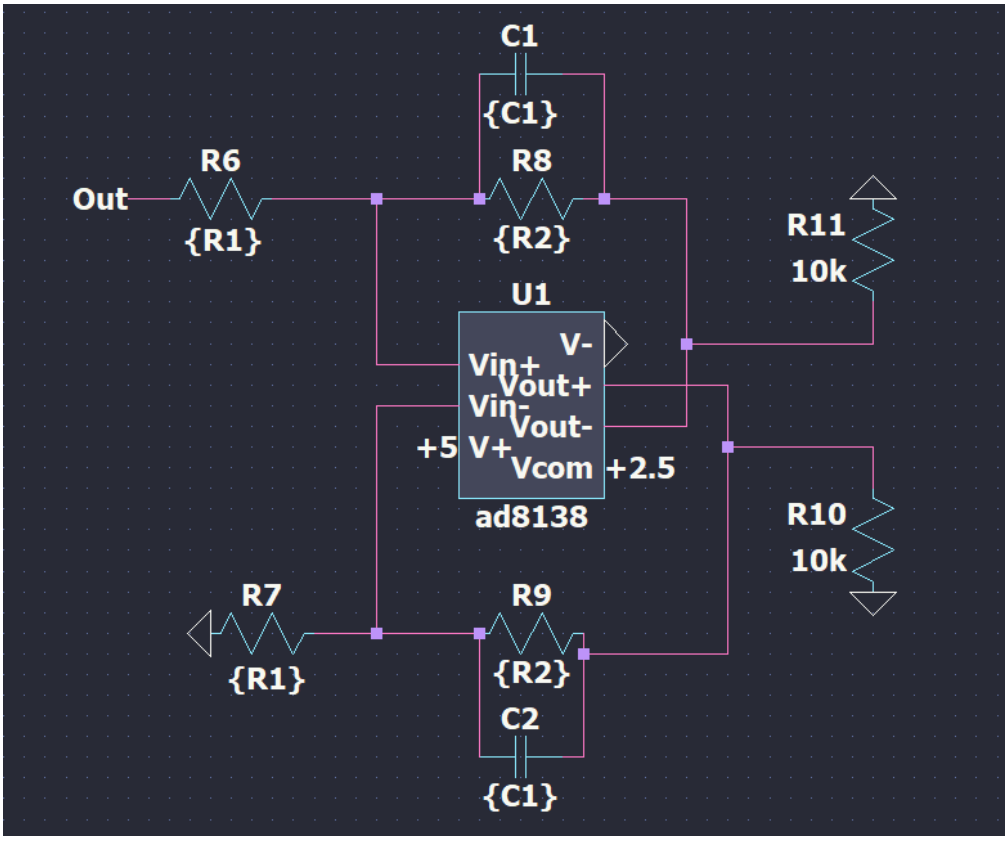

Fig. 4.6: Amplifier Circuit

transfer. The design of the tuning network component values that was outlined in chapter 2. This section will discuss practical development of that tuning design. As described by the design methodology outlined in chapter 2. The first point of design is the primary and secondary coils. For these coils, the use of an existing secondary was utilized and modifications were made to a primary coil design in [115]. The secondary coil is a tri-filer DD coil that is 1 m x 1 m, and capable of handling 750 kVARs at 375 A and 2000 V with an inductance of 7.26 µH. The coil is shown in Fig. 4.9. The primary coil design is also a DD coil. It is a bi-filer coil that is 2.4 m x 1.2 m, capable of handling 500 kVARs at 250 A and 2000 V. From this, an initial tuning topology was tested using values described in chapter 3 and then later revised due to the issues highlighted until the final values were achieved and shown for reference in table 4.2.

The implementation of the split tuning network for these pads was completed using

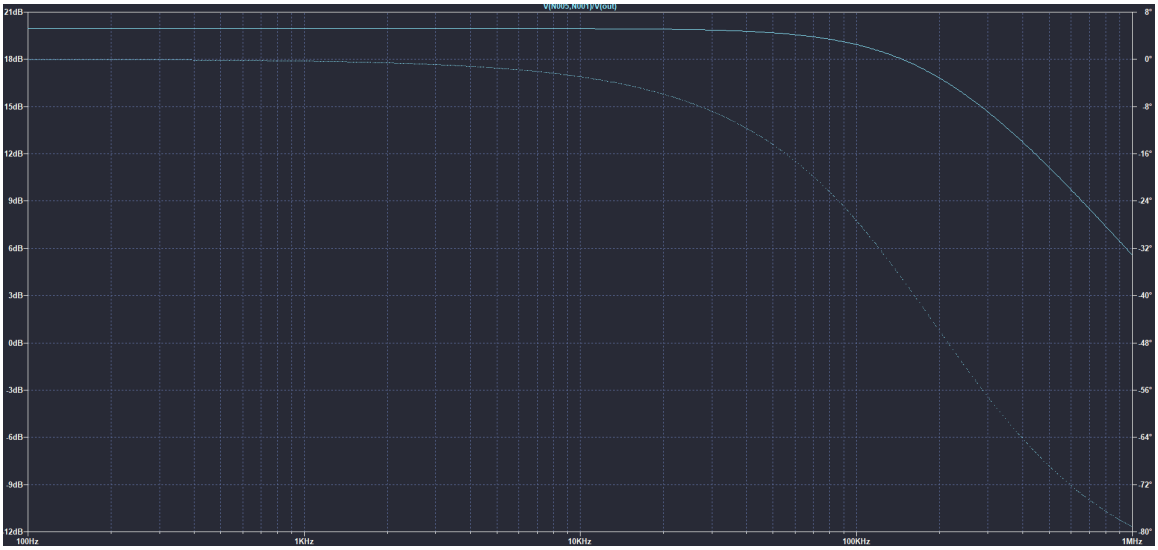

Fig. 4.7: Amplifier bode plot

Table 4.1: Sensor Test Results

Current	Voltage	Phase
34 A	28 mV	N/A
68 A	56 mV	32°
102 A	84 mV	31°
137 A	113 mV	31°
170 A	141 mV	28.6°

Table 4.2: Analytical and Realized Tuning Values for Split Tuning

Component	Analytical Value	Hardware Value
L_{ps1}&L_{ps2}	2.81 µH	2.81 µH
C_{pp}	0.624 µF	0.6308 µF
C_{ps1}&C_{ps2}	0.906 µF	0.830 µF
L_p	13.36 µH	13.36 µH
L_s	7.26 µH	7.26 µH
C_{ss1}&C_{ss2}	1.795 µF	1.980 µF
C_{sp}	1.04 µF	1.045 µF
L_{ss1}&L_{ss2}	1.677 µH	1.677 µH

traditional inductor design principles and bus bar based capacitor networks. The tuning for the secondary is shown in Fig. 4.11. The series and parallel capacitors are designed within a

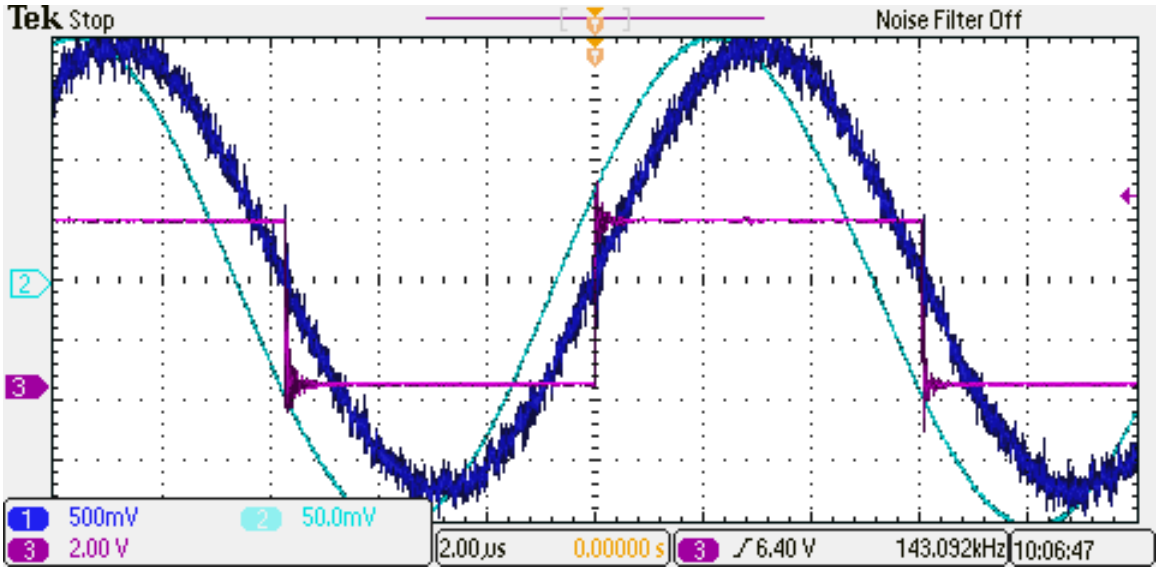

Fig. 4.8: CT and Amplifier Results waveform

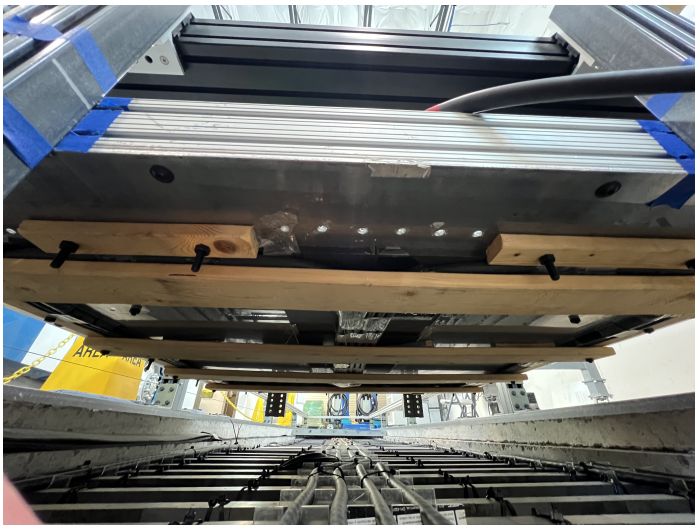

Fig. 4.9: Secondary Coil

Fig. 4.10: Primary Coil

single network utilizing aluminum bus-bars and can be seen in the bottom left. Aluminum bus-bars were eventually chosen for all capacitor design, given the cost-effectiveness and quick turn around for development over copper. The split inductors leading to the inverter can be seen in the center and top right, respectively. The primary side tuning network for the 100 kW pad can be seen in Fig. 4.10. This capacitor bank was originally designed with copper, but will be transitioned to aluminum as well.

4.2 Results

The completed DWPT system can be seen in Fig. 4.12. Where a rail system is utilized to replicate a moving vehicle. As with the simulation of the system, three primaries were constructed. The tuning on the primaries are slightly different between the 100 kW static pad and the other two. This is due to different power level requirements existing between the first iteration of the primary pads at 30 kW and the final design of 100 kW. The first pad, which, is the farthest in the image, has the correct split tuning design for 100 kW. The

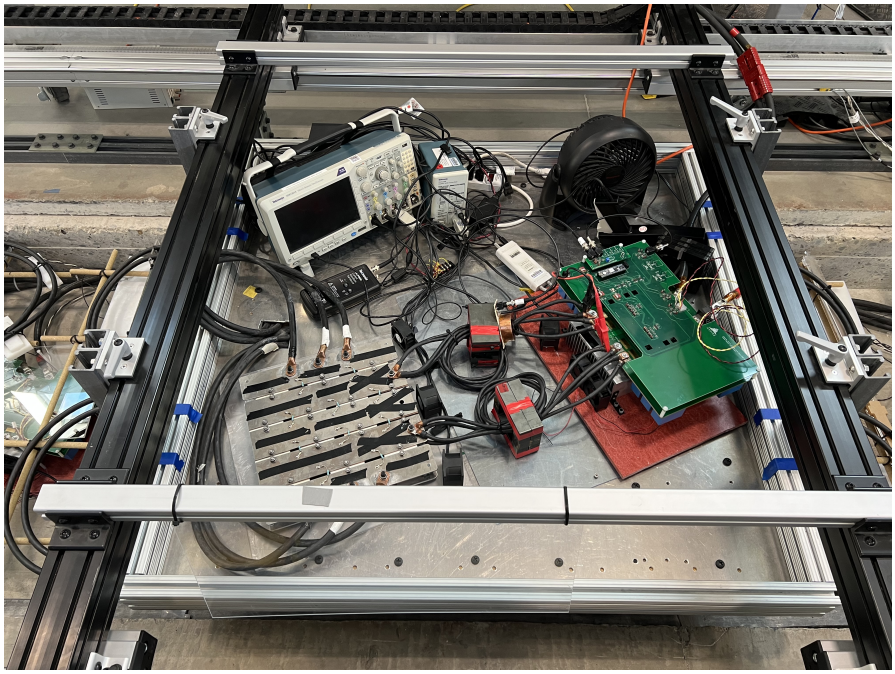

Fig. 4.11: Active Rectifier Setup

closer two pads in the middle and on the left of the figure underneath the secondary system have a lower power rating.

For the static tests, the 100 kW tuning pad was utilized. However, for all dynamic tests, a lower power was run to utilize all the primary pads. The secondary coil tuning and active rectifier are positioned at the bottom of Fig. 4.11 and its measurement equipment moves with the secondary positioned in the top left. To verify the design of the active rectifier, passive rectification testing results are also presented as a reference point in both static and dynamic.

4.2.1 Static

For the static testing, initial verification of the system design was performed. Tests were conducted to the 100 kW design rating. The output power of the experimental results versus the simulated design over the full input voltage range is shown in Fig. 4.13. It can be noted from this figure that the experimental output power is higher than the simulated design. This could be caused by modifications in tuning due to unknown parasitics of the

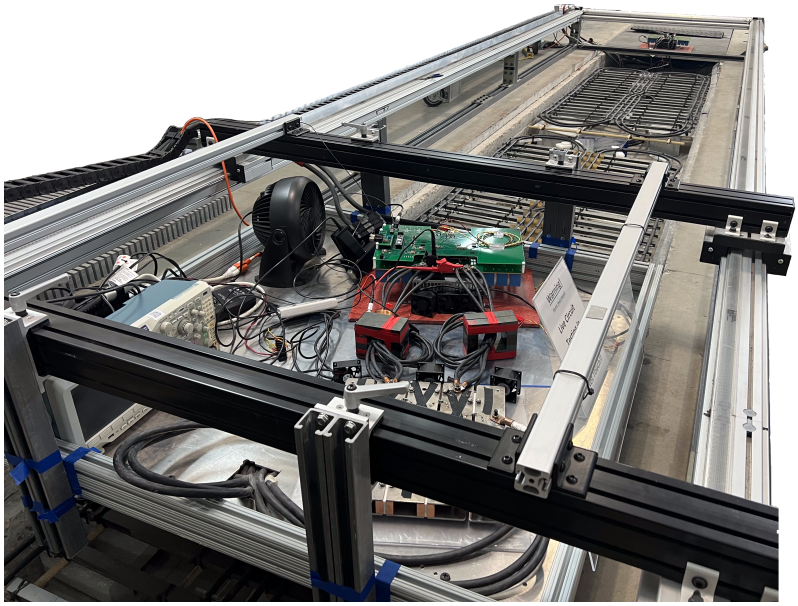

Fig. 4.12: Indoor Rail

tuning network created during construction of the full system assembly.

The full power inverter waveforms are shown in Fig. 4.14. The recirculating current is highlighted in dark blue, the bridge current is in light blue. The current waveform was accidentally inverted, and the bridge voltage is in green. The waveforms show good alignment with the simulated values shown in Fig. 3.8. It also confirms that the system is zero volt switching, improving efficiency.

Once the system had been validated through a passive rectification, the active rectifier could be validated. The initial validation of the controller was performed at the minimum threshold current for the sensing circuit to properly function of approximately 50 A. The square voltage was also operated at a duty cycle below 50% to make it clear the rectifier was actively rectified, power levels for the rectifier are then be slightly below theoretical maximum for the respective voltage curve given in Fig. 4.13.

The frequency difference between controller was initially set to be just the discrepancies between crystal oscillator's at desired frequency of 85 kHz. The results of this experiment can be seen in Fig. 4.15. In this figure, the active rectifier's AC current is shown in light

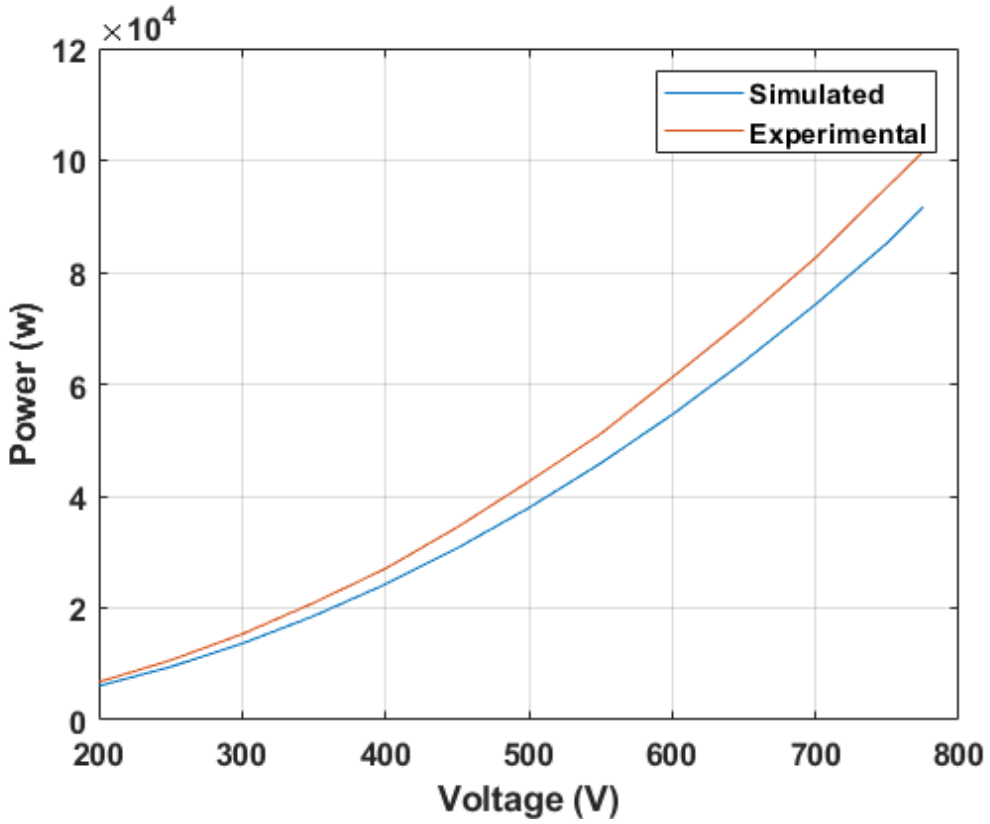

Fig. 4.13: Simulated Vs. Experimental Power

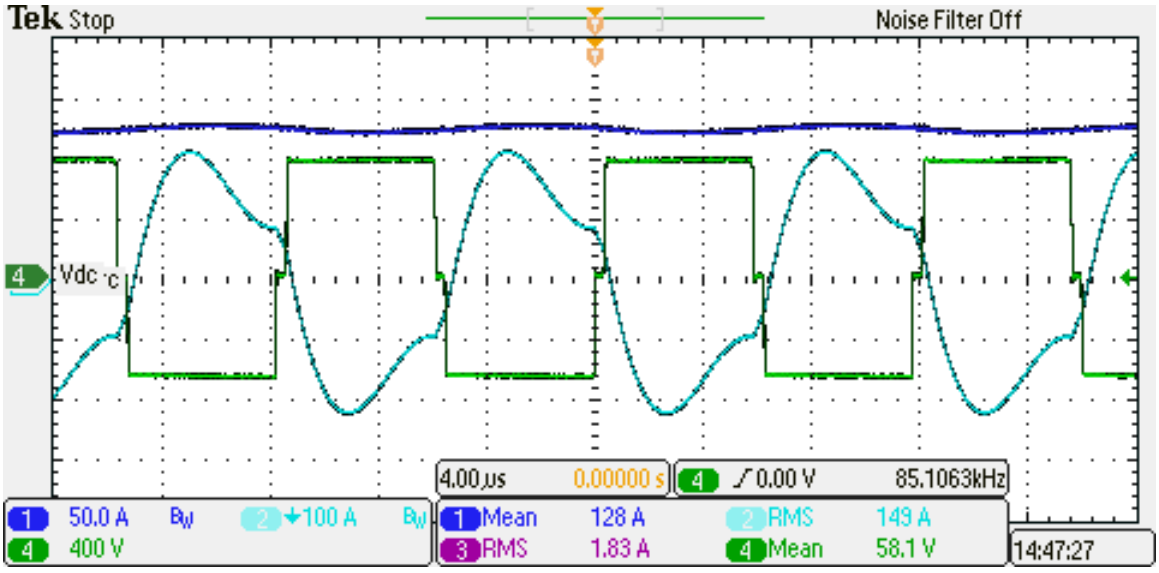

Fig. 4.14: 100 kW Inverter Wave Forms

blue and its induced voltage is shown in purple. The voltage in this image is actually double the represented value due to probe gain not being able to be properly adjusted for on the oscilloscope. The experimental result's alignment show excellent matching to the PLECS simulation of the controller design highlighted in Fig. 3.20.

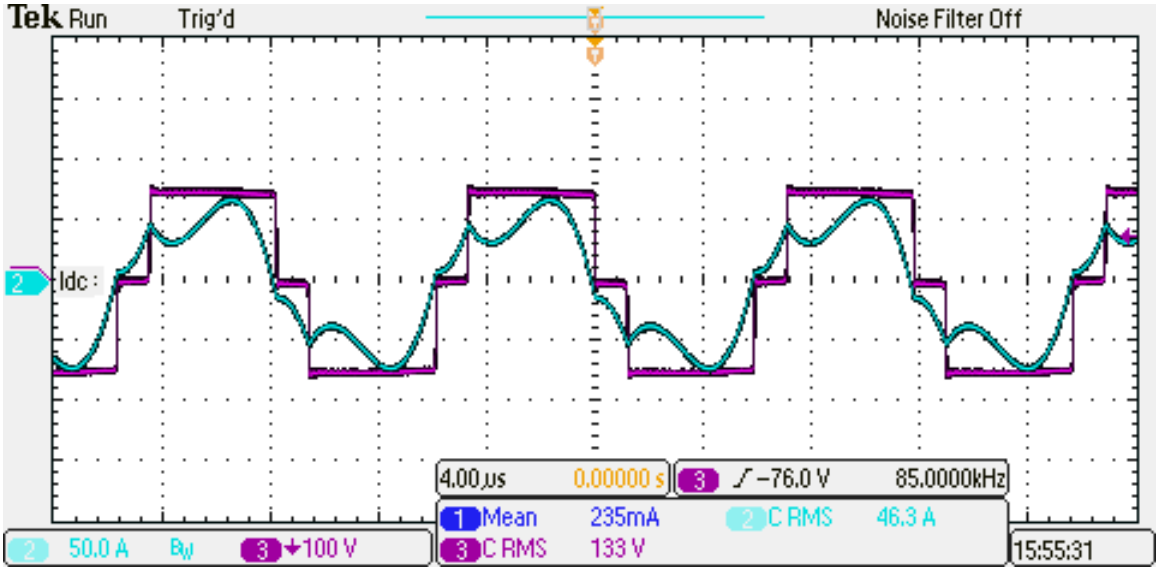

Fig. 4.15: Active Rectifier at 85 kHz

The maximum power transfer achieved by the controller for static testing with the frequency difference of just the internal clocks in this thesis was 20.56 kW. This was achieved with an input voltage of 400 V and a recirculating current of 51.4 A. This was achieved with an efficiency of 91.65%. Note that this was accomplished with a slightly reduced duty cycle, shown in Fig. 4.16. The loss current supplied by the power supply was 4.29 A.

The controller was then pushed to align with a larger frequency difference of approximately 50 Hz to match the PLECS simulation.The secondary controller was set to operate initially at 85 kHz and the primary was set to operate at 85.05 kHz. The results of the experiment are highlighted in Fig. 4.17. In this figure, it can be seen that the waveforms still maintain proper alignment. The frequency of operation registered by the oscilloscope is 85.046 kHz, which puts the frequency difference at 46 Hz between the primary controller and the secondary rectifier.

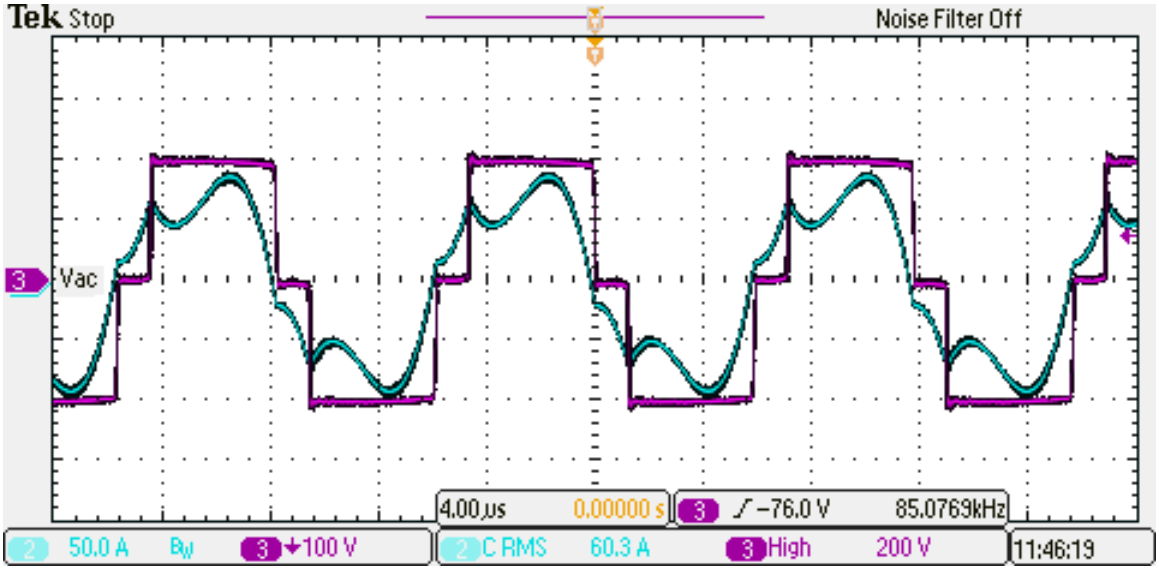

Fig. 4.16: Active Rectifier at 20.56 kW

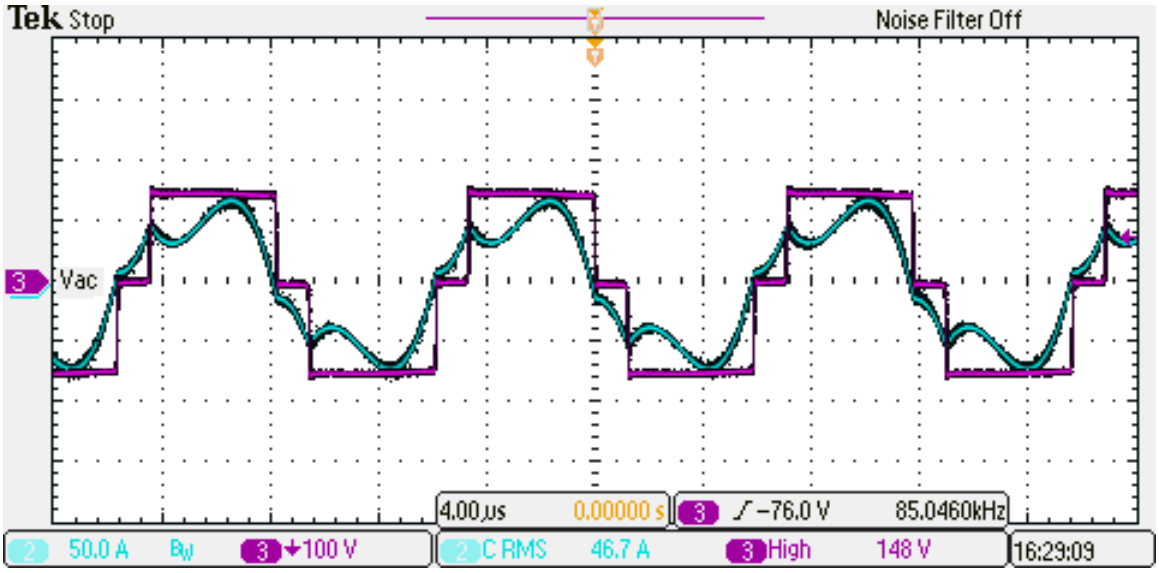

Fig. 4.17: Active Rectifier at 85.046 kHz

Lastly, for the static verification of the controller, which occurred for all tests, was the initialization of the controller based on the induced bridge current amplitude. In Fig. 4.18 a long time screen capture showing the increase of bridge current until activation of the rectifier's switches is shown. In this figure, the induced bridge current is increasing in amplitude until it hits the minimal threshold of 50 A. After which the switching begins and there is an initial starting transient. Once the transient has finished, the system has

stabilized and the rectifier's voltage continued to increase as the DC bus voltage increased.

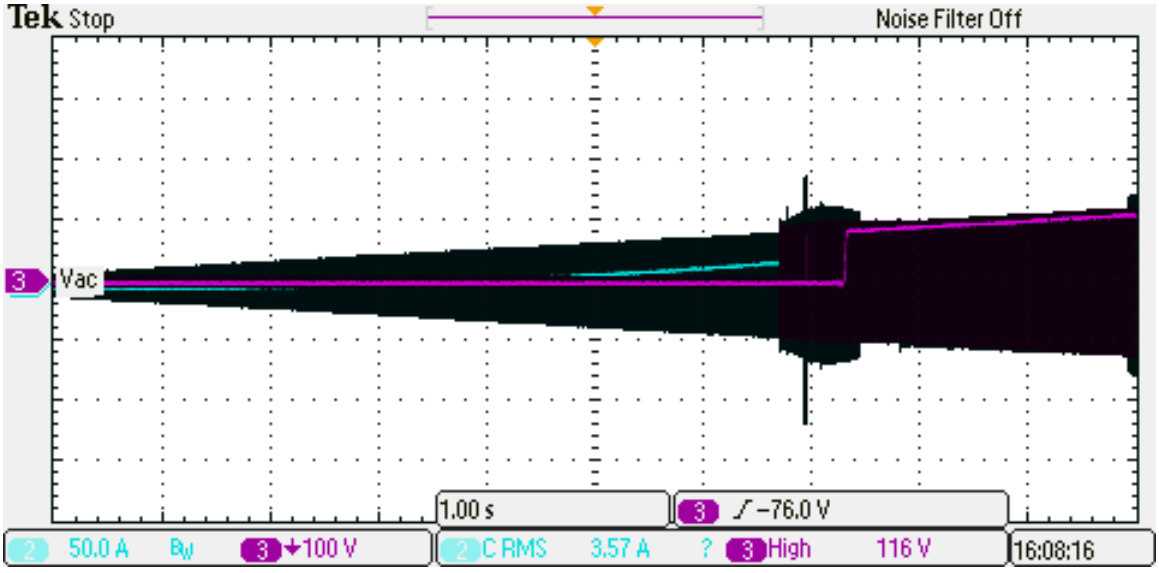

Fig. 4.18: Rectifier Activation Ramp

4.2.2 Dynamic

Initial validation of the dynamic system was first conducted with the passive rectification as a benchmark, as was done with the static verification. The system was run at 450 V. This input voltage yields the 30 kW limit on the other two pads. The resulting received DC current from the passive rectifier is highlighted in Fig. 4.19. For this test, a back and forth pass across the dynamic system is shown. The three primary pads can be seen from this figure, with the first higher power primary being on either end and the two lower power pads in the center, with the reflection point of the waveform being the center of the third pad. The sudden end of power transfer at the very end of the waveform was done through user input to the primary pad's control.

The active rectification test was then performed under the same conditions, but at a lower operating point of 300 V. The lower operating point was chosen due to an instability problem that is shown in the results of the dynamic active rectification, see in Fig. 4.20. In this figure it can be seen that there is a large amount of noise in the recirculating current

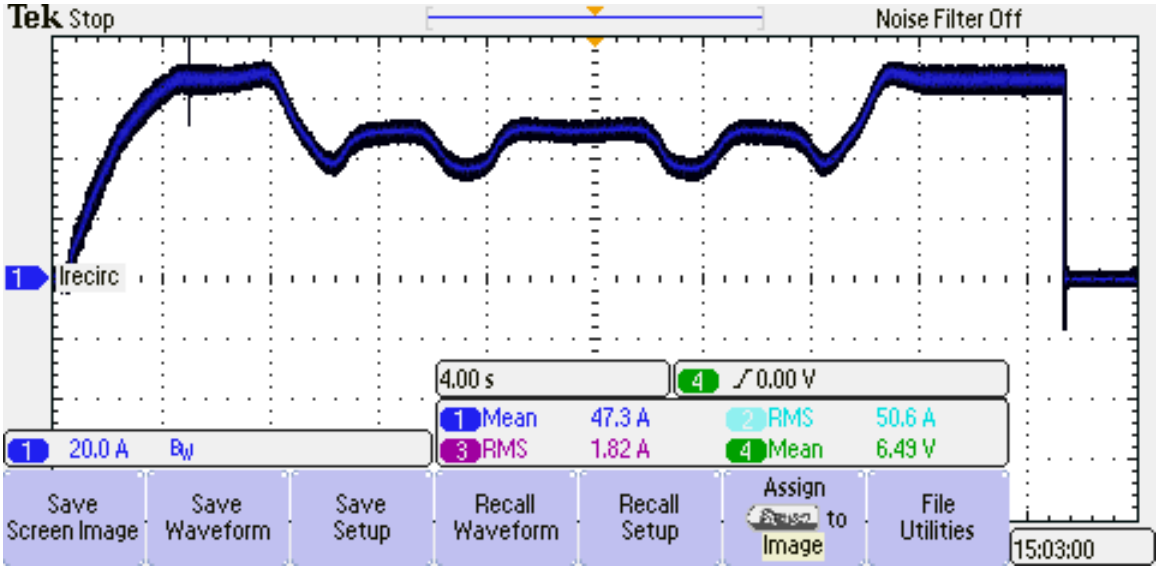

Fig. 4.19: Passive Dynamic Test

that was not as clearly present during the static tests but did exist if the scale of the oscilloscopes measuring DC current were zoomed out. The overall shape of the current waveform and its amplitude for the given power level match the passive rectification results for the system.

However, to find the source of the noise, further testing was done. In Fig. 4.21, it can be seen that the amplitude of this noise not nearly as large when shown on a smaller timescale during static testing and dynamic. It can also be seen that the noise is cyclic in nature and relatively short, appearing approximately every 400 ms. This smaller pulses account for the increased noise band, however, the extremely large noise spikes shown in Fig. 4.19 were not able to be captured on smaller time scales or when the system was tested statically to show their behavior further testing may be able to properly capture them.

To try to find the source of the noise, the active rectifier's oscilloscope was then synced with the trigger set to the blips in current in Fig. 4.21. The results of this trigger are shown in Fig. 4.22. From this figure, there is no discernible inconsistency in the rectifier's waveform that could be the source of this problem. The fundamental nature of the noise is more than likely coming from an error within the implementation of the code at a rollover point, or calculation point, as the controller generates and applies the frequency difference.

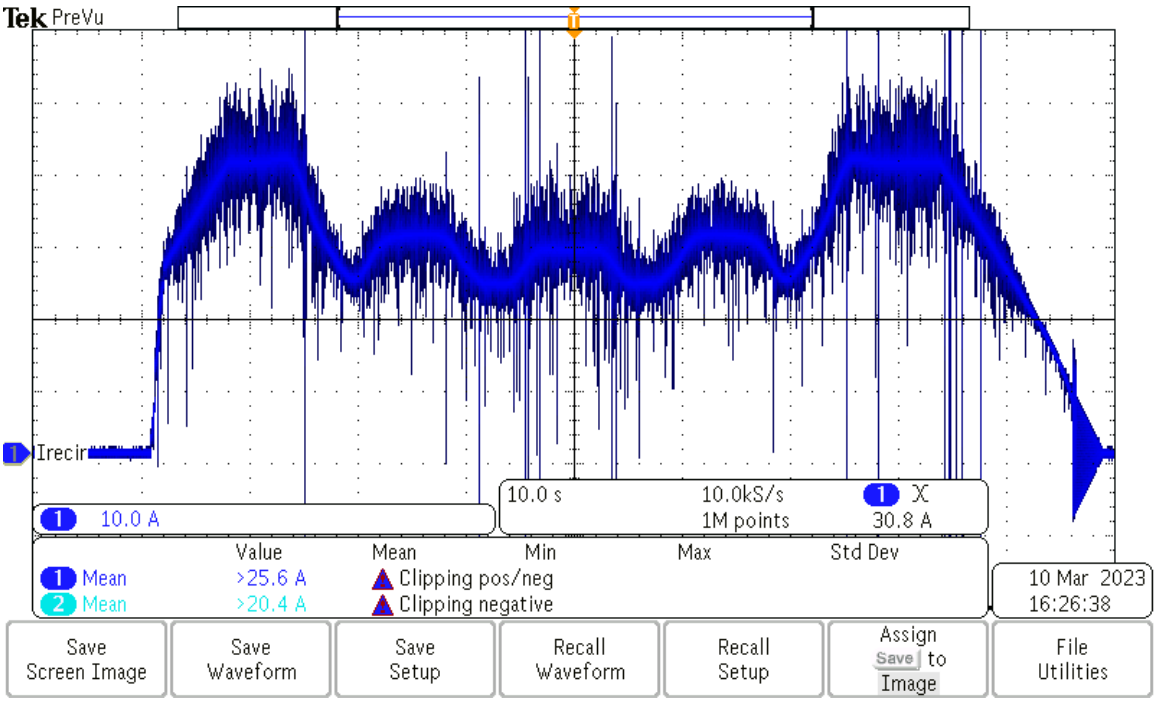

Fig. 4.20: Active Dynamic Test

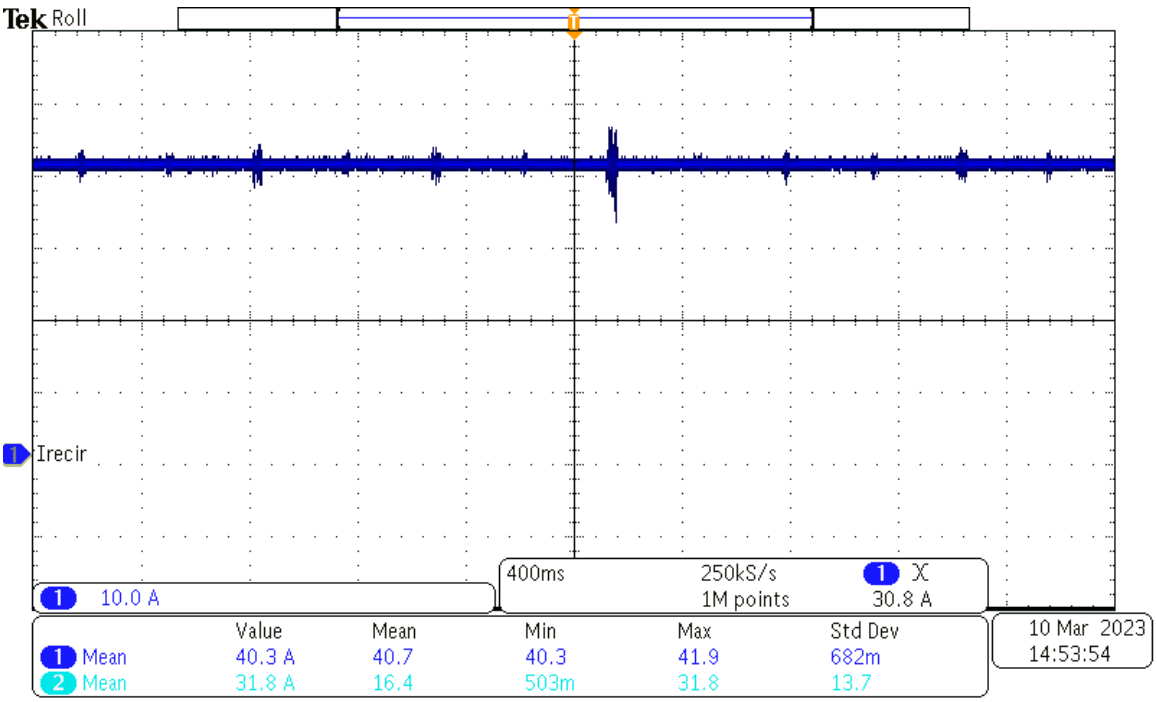

Fig. 4.21: Active Dynamic Test close up

This error is probably introducing a slight offset in the switching waveform on a single cycle, and thus creating the noise that is not readily apparent in the rectifier's waveform. The reason for this error is believed to be from the limitations of the FPGA. For this design, the clock frequencies generated to run this controller were extremely fast for high precision and could be the cause for a missed calculation. A method to potentially fixing this error is reducing the controller operating frequency slightly to improve its stability.

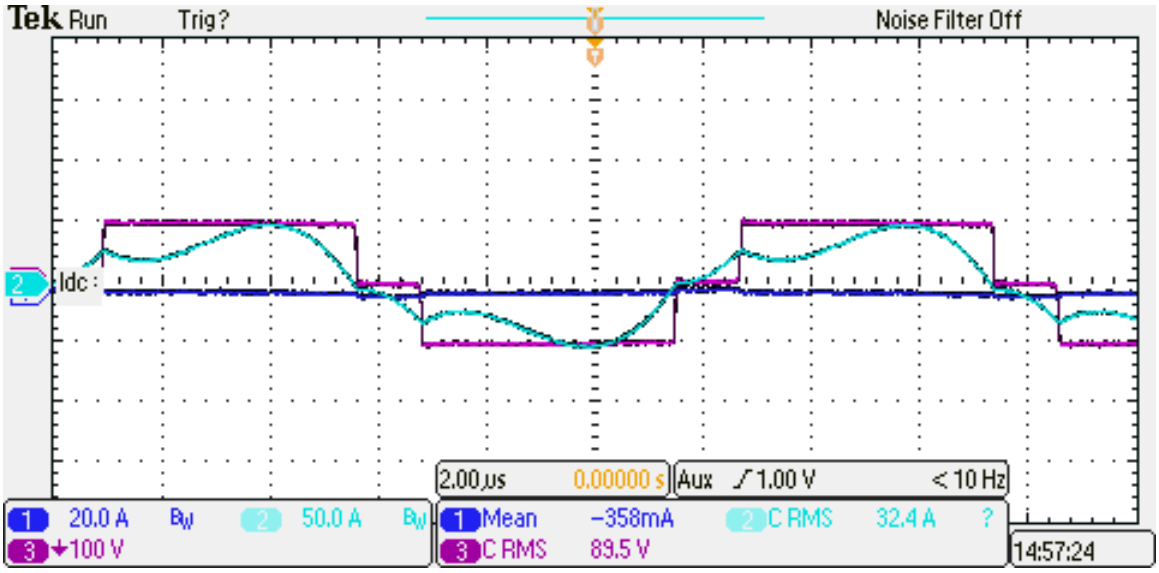

Fig. 4.22: Synchronized Rectifier waveforms during noise instance

CHAPTER 5

Conclusion and Future Work

5.1 Conclusion

This thesis presents the design and implementation of a communication-less synchronous rectification strategy and hardware setup for in motion wireless charging. This work was conducted to validate a method for improved performance for DWPT systems via the removal of extra DC-DC converters to regulate power transfer. The developed hardware for this system was designed for 100 kW heavy-duty vehicle applications and was verified up to that power level with passive rectification. The system was then verified dynamically up to 30 kW.

The active rectification synchronization technique was then implemented utilizing induce bridge currents on the secondary as a method for synchronization. The synchronization method utilizes an AC sensing circuit and a comparator to determine the rising zero crossing of the current. This information is then fed directly to a digital PLL to adjust the internal switching carrier of the secondary. This was then simulated in PLECS along with closed loop control over power regulation. The active rectification controller was then implemented and validate up to 12 kW in both static and dynamic testing. The controller proposed showed excellent matching between simulation and experimental results in terms of the rectifier's alignment. However, there was some induced noise in the rectification that was caused by unknown perturbations from the controller that occurred cyclically.

5.2 Future Work

The future work pertaining to this method of active rectification for in motion wireless charging is, first, resolving the cyclic noise introduced by the controller. Once this source of this noise is resolved, higher power levels for this design can be comfortably reached and

additional controls techniques can be applied.

The second, is implementing and experimentally validating the closed look power regulation on top of the synchronization controller. Implementing this control loop allows for vehicle side power regulation, allowing for interoperable vehicle class use of a single DWPT system. Additionally, it allows for the removal of a vehicle side DC-DC converter.

The third, is the implementation of the closed loop activation and deactivation of the primary and secondary controller. This will drastically improve system efficiency and allow for proper utilization of in motion charging lanes at vehicle discretion.

The fourth, aspect of this control strategy that should be pursued is the inversion of this control strategy to a primary side synchronization to the secondary frequency and phase. For this thesis, the control strategy is employed under the assumption that all the primary pads are synchronized to a common frequency and phase, and the secondary is synchronized to the primaries. This creates additional overhead with the implementation of synchronization cables between primaries and additional points of total system failure. This approach also makes the initial starting of power transfer more difficult due to the necessity of an alternate form of vehicle detection for the first pad's activation.

If this control strategy were to be inverted and applied on the primary side, it would allow for a more seamless control over the DWPT system. It would allow for, first, the removal of synchronization cables from the primary to primary. Second, it would allow for easy vehicle detection since the secondary would be able to activate on demand for power and have the primaries react, as the secondary reacted for this thesis.

The primary limitation for this thesis in implementing this inverted synchronization approach is the primary to primary interaction and that pushing power into the system is fundamentally an unstable application. This is due to the initial phase detected by the second primary pad, after the first has initialized power transfer, in the system would be at a fundamentally incorrect angle to transmit power to the secondary. The current would then have to perform a large transition in phase to transmit power, which would have a major impact on the controller which would have to be ignored by the system. Additionally,

the system would have issues during pad transitions. This is because, as shown in equation 2.19. The inverter's current is dependent upon the receiver's side induced voltage. This would be also be dependent upon neighboring primary pads induced voltage. This causes instability of the current waveform as the both primary controllers seek to push power into the system during pad transitions.

REFERENCES

[1] "Electric vehicles and hybrids surpass 10% of U.S. light-duty vehicle sales." [Online]. Available: https://www.eia.gov/todayinenergy/detail.php?id=51218

[2] O. US EPA, "Inventory of U.S. Greenhouse Gas Emissions and Sinks," Feb. 2017. [Online]. Available: https://www.epa.gov/ghgemissions/inventory-us-greenhouse-gas-emissions-and-sinks

[3] U. Nations, "The Paris Agreement," publisher: United Nations. [Online]. Available: https://www.un.org/en/climatechange/paris-agreement

[4] F. Lambert, "Tesla cuts Supercharger prices back down after customer backlash over increase," Jan. 2019. [Online]. Available: https://electrek.co/2019/01/22/tesla-cuts-supercharger-prices-back-down-customer-backlash/

[5] "EV Charging Stations | Palmdale, CA." [Online]. Available: https://www.cityofpalmdale.org/976/EV-Charging-Stations

[6] "Porsche Taycan (93 kWh Battery) Fast Charging Analysis: Very Good." [Online]. Available: https://insideevs.com/news/512344/porsche-taycan-fast-charging-analysis/

[7] D. Chang, "Battery Electric Buses Reach Wireless Charging Milestone," Feb. 2022. [Online]. Available: https://waveipt.com/battery-electric-bus-reach-wireless-charging-milestone/

[8] Chetvorno, "English: Block diagram of a phase locked loop (PLL), a very common circuit used in radio and telecommunications systems. There are a wide variety of PLL circuits; this diagram shows the simplest type of analog phase locked

loop, which functions as a narrow bandwidth filter." Apr. 2017. [Online]. Available: https://commons.wikimedia.org/wiki/File:Phase_locked_loop.svg

[9] "Global Energy & CO2 Status Report 2019 – Analysis." [Online]. Available: https://www.iea.org/reports/global-energy-co2-status-report-2019

[10] "The Efficiency of Power Plants of Different Types," May 2010, section: posts. [Online]. Available: https://www.brighthubengineering.com/power-plants/72369-compare-the-efficiency-of-different-power-plants/

[11] J. Thomas, "Drive Cycle Powertrain Efficiencies and Trends Derived from EPA Vehicle Dynamometer Results," *SAE International Journal of Passenger Cars - Mechanical Systems*, vol. 7, no. 4, pp. 1374–1384, Oct. 2014. [Online]. Available: https://www.sae.org/content/2014-01-2562/

[12] K. Poornesh, K. P. Nivya, and K. Sireesha, "A Comparative study on Electric Vehicle and Internal Combustion Engine Vehicles," in *2020 International Conference on Smart Electronics and Communication (ICOSEC)*, Sep. 2020, pp. 1179–1183.

[13] N. Adnan, S. M. Nordin, I. Rahman, P. Vasant, and M. A. Noor, "An Overview of Electric Vehicle Technology: A Vision Towards Sustainable Transportation," 2018, iSBN: 9781522552109 Pages: 292-309 Publisher: IGI Global. [Online]. Available: https://www.igi-global.com/chapter/an-overview-of-electric-vehicle-technology/www.igi-global.com/chapter/an-overview-of-electric-vehicle-technology/197137

[14] "2022 Ford F-150® Lightning™ All-Electric Truck | Pricing, Photos, Specs & More | Ford.com." [Online]. Available: https://www.ford.com/trucks/f150/f150-lightning/2022/

[15] R. Shabanpour, S. N. D. Mousavi, N. Golshani, J. Auld, and A. Mohammadian, "Consumer preferences of electric and automated vehicles," in *2017 5th IEEE International Conference on Models and Technologies for Intelligent Transportation Systems (MT-ITS)*, Jun. 2017, pp. 716–720.

[16] V. Etacheri, R. Marom, R. Elazari, G. Salitra, and D. Aurbach, "Challenges in the Development of Advanced Li-Ion Batteries: A Review," *Energy & Environmental Science*, vol. 4, Jan. 2011.

[17] "Battery Pack Prices Fall to an Average of $132/kWh, But Rising Commodity Prices Start to Bite," Nov. 2021, section: Press Release. [Online]. Available: https://about.bnef.com/blog/battery-pack-prices-fall-to-an-average-of-132-kwh-but-rising-commodity-prices-start-to-bite/

[18] D. Pevec, J. Babic, A. Carvalho, Y. Ghiassi-Farrokhfal, W. Ketter, and V. Podobnik, "Electric Vehicle Range Anxiety: An Obstacle for the Personal Transportation (R)evolution?" in *2019 4th International Conference on Smart and Sustainable Technologies (SpliTech)*, Jun. 2019, pp. 1–8.

[19] S. Sachan and N. Adnan, "Stochastic charging of electric vehicles in smart power distribution grids," *Sustainable Cities and Society*, vol. 40, pp. 91–100, Jul. 2018. [Online]. Available: https://www.sciencedirect.com/science/article/pii/S221067071830338X

[20] C. Rodríguez, C. Vidal, M. Díaz, E. Contreras, G. Guggisberg, and I. Rivas, "An Overview of Challenges and Benefits Associated to the Development of Vehicle to Grid Technology," in *2021 IEEE CHILEAN Conference on Electrical, Electronics Engineering, Information and Communication Technologies (CHILECON)*, Dec. 2021, pp. 1–6.

[21] C. Liu, K. T. Chau, D. Wu, and S. Gao, "Opportunities and Challenges of Vehicle-to-Home, Vehicle-to-Vehicle, and Vehicle-to-Grid Technologies," *Proceedings of the IEEE*, vol. 101, no. 11, pp. 2409–2427, Nov. 2013, conference Name: Proceedings of the IEEE.

[22] K. Qian, C. Zhou, M. Allan, and Y. Yuan, "Modeling of Load Demand Due to EV Battery Charging in Distribution Systems," *IEEE Transactions on Power Systems*,

vol. 26, no. 2, pp. 802–810, May 2011, conference Name: IEEE Transactions on Power Systems.

[23] L. Grackova and I. Oleinikova, "Economic motivation for electric vehicles participation in power market," in *11th International Conference on the European Energy Market (EEM14)*, May 2014, pp. 1–5, iSSN: 2165-4093.

[24] Z. Lin, J.-M. Li, and J. Dong, "Dynamic Wireless Power Transfer: Potential Impact on Plug-in Electric Vehicle Adoption," SAE International, Warrendale, PA, SAE Technical Paper 2014-01-1965, Apr. 2014, iSSN: 0148-7191, 2688-3627. [Online]. Available: https://www.sae.org/publications/technical-papers/content/2014-01-1965/

[25] H. Tu, H. Feng, S. Srdic, and S. Lukic, "Extreme Fast Charging of Electric Vehicles: A Technology Overview," *IEEE Transactions on Transportation Electrification*, vol. 5, no. 4, pp. 861–878, Dec. 2019, conference Name: IEEE Transactions on Transportation Electrification.

[26] "Enabling Extreme Fast Charging: A Technology Gap Assessment." [Online]. Available: https://www.energy.gov/eere/vehicles/downloads/enabling-extreme-fast-charging-technology-gap-assessment

[27] P. Machura and Q. Li, "A critical review on wireless charging for electric vehicles," *Renewable and Sustainable Energy Reviews*, vol. 104, pp. 209–234, Apr. 2019. [Online]. Available: https://www.sciencedirect.com/science/article/pii/S1364032119300383

[28] H. Feng, R. Tavakoli, O. C. Onar, and Z. Pantic, "Advances in High-Power Wireless Charging Systems: Overview and Design Considerations," *IEEE Transactions on Transportation Electrification*, vol. 6, no. 3, pp. 886–919, Sep. 2020, conference Name: IEEE Transactions on Transportation Electrification.

[29] B. Song, U. Madawala, and C. Baguley, "A Review of Grid Impacts, Demand Side Issues and Planning Related to Electric Vehicle Charging," in *2021 IEEE Southern Power Electronics Conference (SPEC)*, Dec. 2021, pp. 1–6.

[30] L. Patnaik, P. S. Huynh, D. Vincent, and S. S. Williamson, "Wireless Opportunity Charging as an Enabling Technology for EV Battery Size Reduction and Range Extension: Analysis of an Urban Drive Cycle Scenario," in *2018 IEEE PELS Workshop on Emerging Technologies: Wireless Power Transfer (Wow)*, Jun. 2018, pp. 1–5.

[31] C. Suarez and W. Martinez, "Fast and Ultra-Fast Charging for Battery Electric Vehicles – A Review," in *2019 IEEE Energy Conversion Congress and Exposition (ECCE)*, Sep. 2019, pp. 569–575, iSSN: 2329-3748.

[32] "Supercharger." [Online]. Available: https://www.tesla.com/supercharger

[33] "Porsche Charging all-electric Porsche models quickly and easily. - Porsche USA." [Online]. Available: https://www.porsche.com/usa/aboutporsche/e-performance/charging-bev/

[34] "Charging System Testing - Vehicle Charging System Testing | Advanced Vehicle Testing Activity." [Online]. Available: https://avt.inl.gov/content/charging-system-testing/vehicle-charging-system-testing.html

[35] D. Yelaverthi, "Three-Phase Unfolding Based Soft DC-Link Converter Topologies for AC to DC Applications," *All Graduate Theses and Dissertations*, May 2021. [Online]. Available: https://digitalcommons.usu.edu/etd/8015

[36] K. Gandhi and W. G. Morsi, "Impact of the Open Charge Point Protocol Between the Electric Vehicle and the Fast Charging Station on the Cybersecurity of the Smart Grid," in *2022 IEEE Canadian Conference on Electrical and Computer Engineering (CCECE)*, Sep. 2022, pp. 235–240, iSSN: 2576-7046.

[37] G. Y. Dayanikli, R. R. Hatch, R. M. Gerdes, H. Wang, and R. Zane, "Electromagnetic Sensor and Actuator Attacks on Power Converters for Electric Vehicles," in *2020 IEEE Security and Privacy Workshops (SPW)*, May 2020, pp. 98–103.

[38] C. Chen, Z. Wei, and A. C. Knoll, "Charging Optimization for Li-Ion Battery in Electric Vehicles: A Review," *IEEE Transactions on Transportation Electrification*, vol. 8, no. 3, pp. 3068–3089, Sep. 2022, conference Name: IEEE Transactions on Transportation Electrification.

[39] L. von Kolzenberg, A. Latz, and B. Horstmann, "Solid–Electrolyte Interphase During Battery Cycling: Theory of Growth Regimes," *ChemSusChem*, vol. 13, no. 15, pp. 3901–3910, 2020, _eprint: https://onlinelibrary.wiley.com/doi/pdf/10.1002/cssc.202000867. [Online]. Available: https://onlinelibrary.wiley.com/doi/abs/10.1002/cssc.202000867

[40] "Top 10 Companies in Wireless Electric Vehicle Charging Systems Market | Meticulous Blog," Nov. 2022, section: Information Technology. [Online]. Available: https://meticulousblog.org/top-10-companies-in-wireless-electric-vehicle-charging-systems-market/,https://meticulousblog.org/top-10-companies-in-wireless-electric-vehicle-charging-systems-market/

[41] "Wireless Power Transfer for Electric Vehicles and Mobile Devices | IEEE eBooks | IEEE Xplore." [Online]. Available: https://ieeexplore.ieee.org/book/7953908

[42] Chetvorno, "English: Generic block diagram of a wireless power system that works by (nonresonant) inductive coupling (electromagnetic induction). It works like a transformer. It consists of a "transmitter" unit consisting of an oscillator that produces an alternating current of the correct frequency in a "primary" coil. The alternating current produces an alternating magnetic field (B, green) which extends to the "secondary" coil in the receiver unit and induces a voltage in it by Faraday's law of induction. The alternating current in the secondary is rectified to DC (if DC is needed) and powers a load. This is a simplified version of how wireless charging

units for portable devices like the Qi and PowerPad systems work. Wireless charging stands for tools such as electric toothbrushes operate at mains frequency (50/60 Hz) and so do not need the oscillator, but must use an iron core inside the coils in order to transfer power at low frequencies." Dec. 2014. [Online]. Available: https://commons.wikimedia.org/wiki/File:Wireless_power_system_-_inductive_coupling.svg

[43] J. C. Quinn, B. J. Limb, Z. Pantic, P. Barr, R. Zane, and T. H. Bradley, "Feasibility of wireless power transfer for electrification of transportation: Techno-economics and life cycle assessment," in *2015 IEEE Conference on Technologies for Sustainability (SusTech)*, Jul. 2015, pp. 245–249.

[44] S. Lukic and Z. Pantic, "Cutting the Cord: Static and Dynamic Inductive Wireless Charging of Electric Vehicles," *IEEE Electrification Magazine*, vol. 1, no. 1, pp. 57–64, Sep. 2013, conference Name: IEEE Electrification Magazine.

[45] A. Ahmad, M. S. Alam, and R. Chabaan, "A Comprehensive Review of Wireless Charging Technologies for Electric Vehicles," *IEEE Transactions on Transportation Electrification*, vol. 4, no. 1, pp. 38–63, Mar. 2018, conference Name: IEEE Transactions on Transportation Electrification.

[46] S. Li and C. C. Mi, "Wireless Power Transfer for Electric Vehicle Applications," *IEEE Journal of Emerging and Selected Topics in Power Electronics*, vol. 3, no. 1, pp. 4–17, Mar. 2015, conference Name: IEEE Journal of Emerging and Selected Topics in Power Electronics.

[47] H. Zhang, F. Lu, H. Hofmann, W. Liu, and C. C. Mi, "A Four-Plate Compact Capacitive Coupler Design and LCL-Compensated Topology for Capacitive Power Transfer in Electric Vehicle Charging Application," *IEEE Transactions on Power Electronics*, vol. 31, no. 12, pp. 8541–8551, Dec. 2016, conference Name: IEEE Transactions on Power Electronics.

[48] H. Toromura, Y. Huang, S. Koyama, J. Miyakoshi, and N. Shinohara, "Biological effects of high-power microwave power transfer for electric vehicle," in *2016 IEEE Wireless Power Transfer Conference (WPTC)*, May 2016, pp. 1–3.

[49] I. Ahmed, E. A. ElGhanam, M. S. Hassan, and A. Osman, "Study of the Feasibility of Using Microwave Power Transfer for Dynamic Wireless Electric Vehicle Charging," in *2020 IEEE Transportation Electrification Conference & Expo (ITEC)*, Jun. 2020, pp. 365–370, iSSN: 2377-5483.

[50] B. Hesterman, "Analysis and Modeling of Magnetic Coupling," Jan. 2007.

[51] G. A. Covic and J. T. Boys, "Modern Trends in Inductive Power Transfer for Transportation Applications," *IEEE Journal of Emerging and Selected Topics in Power Electronics*, vol. 1, no. 1, pp. 28–41, Mar. 2013, conference Name: IEEE Journal of Emerging and Selected Topics in Power Electronics.

[52] "J2954_202010: Wireless Power Transfer for Light-Duty Plug-in/Electric Vehicles and Alignment Methodology - SAE International." [Online]. Available: https://www.sae.org/standards/content/j2954_202010/

[53] R. Tavakoli, "Design of Road Embedded Dynamic Charging Systems for Electrified Transportation," *All Graduate Theses and Dissertations*, May 2020. [Online]. Available: https://digitalcommons.usu.edu/etd/7715

[54] Z. Zhang, H. Pang, C. H. T. Lee, X. Xu, X. Wei, and J. Wang, "Comparative Analysis and Optimization of Dynamic Charging Coils for Roadway-Powered Electric Vehicles," *IEEE Transactions on Magnetics*, vol. 53, no. 11, pp. 1–6, Nov. 2017, conference Name: IEEE Transactions on Magnetics.

[55] G. Rituraj, B. K. Kushwaha, and P. Kumar, "A Unipolar Coil Arrangement Method for Improving the Coupling Coefficient Without Ferrite Material in Wireless Power Transfer Systems," *IEEE Transactions on Transportation Electrification*, vol. 6, no. 2,

pp. 497–509, Jun. 2020, conference Name: IEEE Transactions on Transportation Electrification.

[56] C. Wang, C. Zhu, G. Wei, J. Feng, J. Jiang, and R. Lu, "Design of Compact Three-Phase Receiver for Meander-Type Dynamic Wireless Power Transfer System," *IEEE Transactions on Power Electronics*, vol. 35, no. 7, pp. 6854–6866, Jul. 2020, conference Name: IEEE Transactions on Power Electronics.

[57] T. Fujita, T. Yasuda, and H. Akagi, "A Dynamic Wireless Power Transfer System Applicable to a Stationary System," *IEEE Transactions on Industry Applications*, vol. 53, no. 4, pp. 3748–3757, Jul. 2017, conference Name: IEEE Transactions on Industry Applications.

[58] Z. Wang, S. Cui, S. Han, K. Song, C. Zhu, M. I. Matveevich, and O. S. Yurievich, "A Novel Magnetic Coupling Mechanism for Dynamic Wireless Charging System for Electric Vehicles," *IEEE Transactions on Vehicular Technology*, vol. 67, no. 1, pp. 124–133, Jan. 2018, conference Name: IEEE Transactions on Vehicular Technology.

[59] Y. Liu, R. Mai, D. Liu, Y. Li, and Z. He, "Efficiency Optimization for Wireless Dynamic Charging System With Overlapped DD Coil Arrays," *IEEE Transactions on Power Electronics*, vol. 33, no. 4, pp. 2832–2846, Apr. 2018, conference Name: IEEE Transactions on Power Electronics.

[60] S. Cui, Z. Wang, S. Han, C. Zhu, and C. C. Chan, "Analysis and Design of Multiphase Receiver With Reduction of Output Fluctuation for EV Dynamic Wireless Charging System," *IEEE Transactions on Power Electronics*, vol. 34, no. 5, pp. 4112–4124, May 2019, conference Name: IEEE Transactions on Power Electronics.

[61] F. Lu, H. Zhang, H. Hofmann, and C. C. Mi, "A Dynamic Charging System With Reduced Output Power Pulsation for Electric Vehicles," *IEEE Transactions on Industrial Electronics*, vol. 63, no. 10, pp. 6580–6590, Oct. 2016, conference Name: IEEE Transactions on Industrial Electronics.

[62] L. Chen, G. R. Nagendra, J. T. Boys, and G. A. Covic, "Double-Coupled Systems for IPT Roadway Applications," *IEEE Journal of Emerging and Selected Topics in Power Electronics*, vol. 3, no. 1, pp. 37–49, Mar. 2015, conference Name: IEEE Journal of Emerging and Selected Topics in Power Electronics.

[63] Z. Chen, W. Jing, X. Huang, L. Tan, C. Chen, and W. Wang, "A Promoted Design for Primary Coil in Roadway-Powered System," *IEEE Transactions on Magnetics*, vol. 51, no. 11, pp. 1–4, Nov. 2015, conference Name: IEEE Transactions on Magnetics.

[64] G. R. Nagendra, G. A. Covic, and J. T. Boys, "Sizing of Inductive Power Pads for Dynamic Charging of EVs on IPT Highways," *IEEE Transactions on Transportation Electrification*, vol. 3, no. 2, pp. 405–417, Jun. 2017, conference Name: IEEE Transactions on Transportation Electrification.

[65] M. Budhia, G. A. Covic, and J. T. Boys, "Design and Optimization of Circular Magnetic Structures for Lumped Inductive Power Transfer Systems," *IEEE Transactions on Power Electronics*, vol. 26, no. 11, pp. 3096–3108, Nov. 2011, conference Name: IEEE Transactions on Power Electronics.

[66] A. C. Bagchi, A. Kamineni, R. A. Zane, and R. Carlson, "Review and Comparative Analysis of Topologies and Control Methods in Dynamic Wireless Charging of Electric Vehicles," *IEEE Journal of Emerging and Selected Topics in Power Electronics*, vol. 9, no. 4, pp. 4947–4962, Aug. 2021, conference Name: IEEE Journal of Emerging and Selected Topics in Power Electronics.

[67] J. M. Miller, O. C. Onar, and M. Chinthavali, "Primary-Side Power Flow Control of Wireless Power Transfer for Electric Vehicle Charging," *IEEE Journal of Emerging and Selected Topics in Power Electronics*, vol. 3, no. 1, pp. 147–162, Mar. 2015, conference Name: IEEE Journal of Emerging and Selected Topics in Power Electronics.

[68] A. Kamineni, M. J. Neath, A. Zaheer, G. A. Covic, and J. T. Boys, "Interoperable EV Detection for Dynamic Wireless Charging With Existing Hardware and Free

Resonance," *IEEE Transactions on Transportation Electrification*, vol. 3, no. 2, pp. 370–379, Jun. 2017, conference Name: IEEE Transactions on Transportation Electrification.

[69] C. Park, S. Lee, S. Y. Jeong, G.-H. Cho, and C. T. Rim, "Uniform Power I-Type Inductive Power Transfer System With DQ-Power Supply Rails for On-Line Electric Vehicles," *IEEE Transactions on Power Electronics*, vol. 30, no. 11, pp. 6446–6455, Nov. 2015, conference Name: IEEE Transactions on Power Electronics.

[70] H. Feng, T. Cai, S. Duan, J. Zhao, X. Zhang, and C. Chen, "An LCC-Compensated Resonant Converter Optimized for Robust Reaction to Large Coupling Variation in Dynamic Wireless Power Transfer," *IEEE Transactions on Industrial Electronics*, vol. 63, no. 10, pp. 6591–6601, Oct. 2016, conference Name: IEEE Transactions on Industrial Electronics.

[71] S. Zou, O. C. Onar, V. Galigekere, J. Pries, G.-J. Su, and A. Khaligh, "Secondary Active Rectifier Control Scheme for a Wireless Power Transfer System with Double-Sided LCC Compensation Topology," in *IECON 2018 - 44th Annual Conference of the IEEE Industrial Electronics Society*, Oct. 2018, pp. 2145–2150, iSSN: 2577-1647.

[72] A. K. Swain, M. J. Neath, U. K. Madawala, and D. J. Thrimawithana, "A Dynamic Multivariable State-Space Model for Bidirectional Inductive Power Transfer Systems," *IEEE Transactions on Power Electronics*, vol. 27, no. 11, pp. 4772–4780, Nov. 2012, conference Name: IEEE Transactions on Power Electronics.

[73] D. J. Thrimawithana and U. K. Madawala, "A Generalized Steady-State Model for Bidirectional IPT Systems," *IEEE Transactions on Power Electronics*, vol. 28, no. 10, pp. 4681–4689, Oct. 2013, conference Name: IEEE Transactions on Power Electronics.

[74] Y. Tang, Y. Chen, U. K. Madawala, D. J. Thrimawithana, and H. Ma, "A New Controller for Bidirectional Wireless Power Transfer Systems," *IEEE Transactions on Power Electronics*, vol. 33, no. 10, pp. 9076–9087, Oct. 2018, conference Name: IEEE Transactions on Power Electronics.

[75] A. Desmoort, O. Deblecker, and Z. De Grève, "Active Rectification For the Optimal Command of Bidirectional Resonant Wireless Power Transfer Robust to Severe Circuit Parameters Deviations," *IEEE Transactions on Industry Applications*, vol. 56, no. 2, pp. 1640–1648, Mar. 2020, conference Name: IEEE Transactions on Industry Applications.

[76] D. Seltzer, L. Corradini, D. Bloomquist, R. Zane, and D. Maksimović, "Small signal phasor modeling of dual active bridge series resonant DC/DC converters with multi-angle phase shift modulation," in *2011 IEEE Energy Conversion Congress and Exposition*, Sep. 2011, pp. 2757–2764, iSSN: 2329-3748.

[77] U. K. Madawala, M. Neath, and D. J. Thrimawithana, "A Power–Frequency Controller for Bidirectional Inductive Power Transfer Systems," *IEEE Transactions on Industrial Electronics*, vol. 60, no. 1, pp. 310–317, Jan. 2013, conference Name: IEEE Transactions on Industrial Electronics.

[78] D. J. Thrimawithana, U. K. Madawala, and M. Neath, "A Synchronization Technique for Bidirectional IPT Systems," *IEEE Transactions on Industrial Electronics*, vol. 60, no. 1, pp. 301–309, Jan. 2013, conference Name: IEEE Transactions on Industrial Electronics.

[79] C.-Y. Huang, J. T. Boys, and G. A. Covic, "LCL Pickup Circulating Current Controller for Inductive Power Transfer Systems," *IEEE Transactions on Power Electronics*, vol. 28, no. 4, pp. 2081–2093, Apr. 2013, conference Name: IEEE Transactions on Power Electronics.

[80] T. Diekhans and R. W. De Doncker, "A Dual-Side Controlled Inductive Power Transfer System Optimized for Large Coupling Factor Variations and Partial Load," *IEEE Transactions on Power Electronics*, vol. 30, no. 11, pp. 6320–6328, Nov. 2015, conference Name: IEEE Transactions on Power Electronics.

[81] H. H. Wu, A. Gilchrist, K. D. Sealy, and D. Bronson, "A High Efficiency 5 kW Inductive Charger for EVs Using Dual Side Control," *IEEE Transactions on Industrial*

Informatics, vol. 8, no. 3, pp. 585–595, Aug. 2012, conference Name: IEEE Transactions on Industrial Informatics.

[82] Y.-D. Lee, D.-M. Kim, C.-E. Kim, and G.-W. Moon, "A New Receiver-Side Integrated Regulator With Phase Shift Control Strategy For Wireless Power Transfer System," in *2020 IEEE PELS Workshop on Emerging Technologies: Wireless Power Transfer (WoW)*, Nov. 2020, pp. 112–115.

[83] C. Liu and X. Liu, "Inductive Power Transfer System with Automatic Control," in *2019 IEEE PELS Workshop on Emerging Technologies: Wireless Power Transfer (WoW)*, Jun. 2019, pp. 383–386.

[84] L. H. Chan, Y. Yang, and K.-W. E. Cheng, "Comparative Studies on the Primary-Side Frequency and Phase Shift Control for Series-Series Compensated Inductive Power Transfer," in *2020 8th International Conference on Power Electronics Systems and Applications (PESA)*, Dec. 2020, pp. 1–5.

[85] M. J. Neath, A. K. Swain, U. K. Madawala, and D. J. Thrimawithana, "An Optimal PID Controller for a Bidirectional Inductive Power Transfer System Using Multiobjective Genetic Algorithm," *IEEE Transactions on Power Electronics*, vol. 29, no. 3, pp. 1523–1531, Mar. 2014, conference Name: IEEE Transactions on Power Electronics.

[86] M. Neath, U. Madawala, and D. Thrimawithana, "Frequency jitter control of a multiple pick-up Bidirectional Inductive Power Transfer system," in *2013 IEEE International Conference on Industrial Technology (ICIT)*, Feb. 2013, pp. 521–526.

[87] G. Elliott, J. Boys, and A. Green, "Magnetically coupled systems for power transfer to electric vehicles," in *Proceedings of 1995 International Conference on Power Electronics and Drive Systems. PEDS 95*, Feb. 1995, pp. 797–801 vol.2.

[88] A. Green and J. Boys, "10 kHz inductively coupled power transfer-concept and control," in *1994 Fifth International Conference on Power Electronics and Variable-Speed Drives*, Oct. 1994, pp. 694–699.

[89] W. Chen, F. Lin, G. A. Covic, and J. T. Boys, "Design Considerations of a Bipolar Track for Dynamic Electric Vehicle Charging," in *2019 IEEE Energy Conversion Congress and Exposition (ECCE)*, Sep. 2019, pp. 1188–1194, iSSN: 2329-3748.

[90] K. Throngnumchai, A. Hanamura, Y. Naruse, and K. Takeda, "Design and evaluation of a wireless power transfer system with road embedded transmitter coils for dynamic charging of electric vehicles," in *2013 World Electric Vehicle Symposium and Exhibition (EVS27)*, Nov. 2013, pp. 1–10.

[91] V. X. Thai, S. Y. Choi, B. H. Choi, J. H. Kim, and C. T. Rim, "Coreless power supply rails compatible with both stationary and dynamic charging of electric vehicles," in *2015 IEEE 2nd International Future Energy Electronics Conference (IFEEC)*, Nov. 2015, pp. 1–5.

[92] S. Nagai, T. Fujita, H. Fujimoto, S. Tsuge, and T. Hashimoto, "Efficiency Evaluation of Receiving Current Control Using Pulse Density Modulation for Dynamic Wireless Power Transfer," in *2021 IEEE PELS Workshop on Emerging Technologies: Wireless Power Transfer (WoW)*, Jun. 2021, pp. 1–5.

[93] K. Hata, T. Imura, and Y. Hori, "Dynamic wireless power transfer system for electric vehicles to simplify ground facilities - power control and efficiency maximization on the secondary side," in *2016 IEEE Applied Power Electronics Conference and Exposition (APEC)*, Mar. 2016, pp. 1731–1736.

[94] C. Wang, C. Zhu, K. Song, G. Wei, S. Dong, and R. G. Lu, "Primary-side control method in two-transmitter inductive wireless power transfer systems for dynamic wireless charging applications," in *2017 IEEE PELS Workshop on Emerging Technologies: Wireless Power Transfer (WoW)*, May 2017, pp. 1–6.

[95] W. Cai, H. Tang, X. Lai, and L. Sun, "Multiple-Receiver Wireless Power Transfer with Efficient Power Control Strategy," in *2019 IEEE PELS Workshop on Emerging Technologies: Wireless Power Transfer (WoW)*, Jun. 2019, pp. 378–382.

[96] H. Hu, T. Cai, S. Duan, H. Feng, X. Zhang, J. Niu, and J. Zhao, "Constant maximum power control for dynamic wireless power transmission system," in *2017 IEEE PELS Workshop on Emerging Technologies: Wireless Power Transfer (WoW)*, May 2017, pp. 295–299.

[97] Z. Zhou, L. Zhang, Z. Liu, Q. Chen, R. Long, and H. Su, "Model Predictive Control for the Receiving-Side DC–DC Converter of Dynamic Wireless Power Transfer," *IEEE Transactions on Power Electronics*, vol. 35, no. 9, pp. 8985–8997, Sep. 2020, conference Name: IEEE Transactions on Power Electronics.

[98] D. Kobayashi, T. Imura, and Y. Hori, "Real-time coupling coefficient estimation and maximum efficiency control on dynamic wireless power transfer for electric vehicles," in *2015 IEEE PELS Workshop on Emerging Technologies: Wireless Power (2015 WoW)*, Jun. 2015, pp. 1–6.

[99] C. Cui, K. Song, C. Zhu, Q. Zhang, Y. Liu, and S. Dong, "State Feedback Controller Design of Dynamic Wireless Power Transfer System," in *2018 IEEE PELS Workshop on Emerging Technologies: Wireless Power Transfer (Wow)*, Jun. 2018, pp. 1–5.

[100] N. T. Diep, N. K. Trung, and T. T. Minh, "Power Control in the Dynamic Wireless Charging of Electric Vehicles," in *2019 10th International Conference on Power Electronics and ECCE Asia (ICPE 2019 - ECCE Asia)*, May 2019, pp. 1–6, iSSN: 2150-6086.

[101] R. Tavakoli, A. Jovicic, N. Chandrappa, R. Bohm, and Z. Pantic, "Design of a dual-loop controller for in-motion wireless charging of an electric bus," in *2016 IEEE Energy Conversion Congress and Exposition (ECCE)*, Sep. 2016, pp. 1–8.

[102] F. Farajizadeh, D. Barth, D. M. Vilathgamuwa, T. Leibfried, and U. K. Madawala, "Control of Power in Dynamic Wireless Power Transfer Systems With the use of PWM-Synchronized Sampling Technique," in *2021 IEEE 12th Energy Conversion Congress Exposition - Asia (ECCE-Asia)*, May 2021, pp. 148–152, iSSN: 2150-6086.

[103] A. Ong, P. K. S. Jayathuathnage, J. H. Cheong, and W. L. Goh, "Transmitter Pulsation Control for Dynamic Wireless Power Transfer Systems," *IEEE Transactions on Transportation Electrification*, vol. 3, no. 2, pp. 418–426, Jun. 2017, conference Name: IEEE Transactions on Transportation Electrification.

[104] "Development of Intermediate Controllers for Inductive Charging Systems in Dynamic Roadway Systems." [Online]. Available: https://researchspace.auckland.ac.nz/handle/2292/36183

[105] R. Shen, W. Xiao, B. Zhang, D. Qiu, and C. N. Man Ho, "Load Detection Method and Control of Class-E Inverter for Dynamic Wireless Power Transfer," in *2018 IEEE PELS Workshop on Emerging Technologies: Wireless Power Transfer (Wow)*, Jun. 2018, pp. 1–5.

[106] N. Hasan, H. Wang, T. Saha, and Z. Pantic, "A novel position sensorless power transfer control of lumped coil-based in-motion wireless power transfer systems," in *2015 IEEE Energy Conversion Congress and Exposition (ECCE)*, Sep. 2015, pp. 586–593, iSSN: 2329-3748.

[107] S. Inoue, C. R. Teeneti, D. Goodrich, J. Larsen, A. Kamineni, and R. Zane, "High-Power Field-Focusing Circuit for Dynamic Wireless Power Transfer Systems," in *2022 Wireless Power Week (WPW)*, Jul. 2022, pp. 699–704.

[108] K. Lee, Z. Pantic, and S. M. Lukic, "Reflexive Field Containment in Dynamic Inductive Power Transfer Systems," *IEEE Transactions on Power Electronics*, vol. 29, no. 9, pp. 4592–4602, Sep. 2014, conference Name: IEEE Transactions on Power Electronics.

[109] A. Dayerizadeh, H. Feng, and S. M. Lukic, "Dynamic Wireless Charging: Reflexive Field Containment Using Saturable Inductors," *IEEE Transactions on Industry Applications*, vol. 56, no. 2, pp. 1784–1792, Mar. 2020, conference Name: IEEE Transactions on Industry Applications.

[110] S. Y. Jeong, J. H. Park, G. P. Hong, and C. T. Rim, "Automatic Current Control by Self-Inductance Variation for Dynamic Wireless EV Charging," in *2018 IEEE PELS Workshop on Emerging Technologies: Wireless Power Transfer (Wow)*, Jun. 2018, pp. 1–5.

[111] ——, "Autotuning Control System by Variation of Self-Inductance for Dynamic Wireless EV Charging With Small Air Gap," *IEEE Transactions on Power Electronics*, vol. 34, no. 6, pp. 5165–5174, Jun. 2019, conference Name: IEEE Transactions on Power Electronics.

[112] H. Hao, G. A. Covic, and J. T. Boys, "An Approximate Dynamic Model of LCL-T-Based Inductive Power Transfer Power Supplies," *IEEE Transactions on Power Electronics*, vol. 29, no. 10, pp. 5554–5567, Oct. 2014, conference Name: IEEE Transactions on Power Electronics.

[113] H. Li, J. Fang, and Y. Tang, "Reduced-Order Dynamical Models of Tuned Wireless Power Transfer Systems," in *2018 International Power Electronics Conference (IPEC-Niigata 2018 -ECCE Asia)*, May 2018, pp. 337–341.

[114] E. Ayisire, A. El-Shahat, and A. Sharaf, "Magnetic Resonance Coupling Modelling for Electric Vehicles Wireless Charging," in *2018 IEEE Global Humanitarian Technology Conference (GHTC)*, Oct. 2018, pp. 1–2, iSSN: 2377-6919.

[115] B. Varghese, "Roadway-Embedded Transmitters and Multi-Pad Receivers for High Power Dynamic Wireless Power Transfer," *All Graduate Theses and Dissertations*, Dec. 2021. [Online]. Available: https://digitalcommons.usu.edu/etd/8232

[116] G. A. Covic and J. T. Boys, "Inductive Power Transfer," *Proceedings of the IEEE*, vol. 101, no. 6, pp. 1276–1289, Jun. 2013, conference Name: Proceedings of the IEEE.

[117] D. J. Thrimawithana and U. K. Madawala, "A novel matrix converter based bi-directional IPT power interface for V2G applications," in *2010 IEEE International Energy Conference*, Dec. 2010, pp. 495–500.

[118] EETimes, "Using PLLs to Obtain Carrier Synchronization: Part 1," Mar. 2003. [Online]. Available: https://www.eetimes.com/using-plls-to-obtain-carrier-synchronization-part-1/

[119] ——, "Using PLLs to Obtain Carrier Synchronization: Part 2," Apr. 2003. [Online]. Available: https://www.eetimes.com/using-plls-to-obtain-carrier-synchronization-part-2/

[120] L. Litwin, "Matched filtering and timing recovery in digital receivers," 2001. [Online]. Available: https://www.semanticscholar.org/paper/Matched-filtering-and-timing-recovery-in-digital-Litwin/0b564223aa685e3c7dbab13cb2c3a8e75f27525d

[121] N. A. Keeling, G. A. Covic, and J. T. Boys, "A Unity-Power-Factor IPT Pickup for High-Power Applications," *IEEE Transactions on Industrial Electronics*, vol. 57, no. 2, pp. 744–751, Feb. 2010, conference Name: IEEE Transactions on Industrial Electronics.